NOVA SCHOOL OF SCIENCE & TECHNOLOGY

DEPARTMENT OF MATERIALS SCIENCE

JOANA FERNANDES DOS SANTOS

Bachelor in Cell and Molecular Biology

EXPLORING IRON OXIDE NANOPARTICLES COATING AND STABILITY FOR MAGNETIC HYPERTHERMIA APPLICATIONS

MASTER IN BIOMATERIALS AND NANOMEDICINE

NOVA University Lisbon

November, 2023

NOVA SCHOOL OF SCIENCE & TECHNOLOGY

DEPARTMENT OF MATERIALS SCIENCE

EXPLORING IRON OXIDE NANOPARTICLES COATING AND STABILITY FOR MAGNETIC HYPERTHERMIA APPLICATIONS

JOANA FERNANDES DOS SANTOS

Bachelor in Cell and Molecular Biology

Adviser: Dr. Paula Isabel Pereira Soares
Researcher, NOVA University Lisbon

Co-adviser: Dr. Tânia Sofia dos Santos Vieira
Researcher, NOVA University Lisbon

Examination Committee:

Chair: Dr. Jorge Alexandre Monteiro Carvalho Silva,
Associate Professor, NOVA University Lisbon

Rapporteur: Dr. José Ricardo Ramos Franco Tavares,
Associate Professor, NOVA University Lisbon

Adviser: Dr. Paula Isabel Pereira Soares,
Researcher, NOVA University Lisbon

MASTER IN BIOMATERIALS AND NANOMEDICINE

NOVA University Lisbon
November, 2023

Exploring Iron Oxide Nanoparticles Coating and Stability for Magnetic Hyperthermia Applications.

ACKNOWLEDGMENTS

Primeiramente, gostaria de agradecer às minhas orientadoras. À minha orientadora, Doutora Paula Soares, pela oportunidade, por toda a disponibilidade e por toda a paciência ao longo deste último ano. Gostaria de agradecer também à minha coorientadora, Doutora Tânia Vieira por me receber, orientar, fazer rir e ajudar.

Gostaria de agradecer também ao Doutor João Paulo Borges por me receber no Departamento de Ciências dos Materiais e à Doutora Susete Fernandes por me receber, juntamente com a minha orientadora, nos laboratórios deste departamento. Agradeço também ao Doutor Jorge Silva por me receber no Departamento de Física e por me perguntar, sempre com um sorriso, como me estava a correr o trabalho no laboratório de Engenharia de Células e Tecidos.

Obrigada ao Cezar, à Catarina e à Sofia por terem facilitado a minha adaptação aos laboratórios e, principalmente, por todos os desabafos, histórias, conselhos e risos, fizeram me mesmo sentir em casa. Um muito especial obrigada à Beatriz que, desde o momento que soube o tema da minha dissertação, foi incansável e fez questão de estar sempre a par de todo o percurso até ao dia de hoje. E obrigada à Marta que foi muito importante no impacto inicial deste percurso e à Inês pelos desabafos nas horas de almoço.

Quero também agradecer aos amigos que a faculdade me deu ao longo destes 5 anos. À Blue, a minha alentejana, por me ter mostrado que tenho uma costela de Vila Verde de Ficalho, ao Gonçalo por me ter aturado durante estes 5 anos, à Martelo por ser das melhores pessoas que conheço, à Botelho e à Francisca por, mesmo longe, se terem mantido próximas e obrigada a todos os que não mencionei, mas que sabem que são importantes.

Aos meus amigos fora da faculdade. Obrigada à Mariana, à Carolina, à Bea, à Mesqui e ao Chico por estarem sempre lá, por me distraírem e por me ouvirem sempre que preciso. Obrigada à Marta por estar presente quer fosse em Seia, em casa ou na faculdade. A todos vocês obrigada por partilharem comigo esta etapa.

Obrigada à Margarida e ao Gonçalo. Ao meu namorado por se esforçar para perceber e acompanhar o meu trabalho e por acreditar sempre em mim. Obrigada à Margarida, por ter sido a maior constante destes 5 anos, sou mesmo grata a esta faculdade por ela ter aparecido na minha vida e não imagino este percurso sem ela.

Por último, sou eternamente grata à minha família. O maior obrigada do mundo à minha mãe, ao meu pai, à minha irmã, aos meus quatro avós, às minhas tias e primos pois são os responsáveis pelo que alcancei até hoje. Não imagino fazê-lo sem o apoio incondicional que me deram.

“Adventure is worthwhile in itself”

(Amelia Earhart)

ABSTRACT

Currently, cancer treatment research is a leading focus due to limitations in conventional treatments. In particular, malignant melanoma often demonstrates treatment resistance. In response, researchers have been investing in innovative approaches such as magnetic hyperthermia (MH).

MH relies on locally increasing the temperatures to trigger death mechanisms in cancerous cells, employing superparamagnetic iron oxide nanoparticles (SPIONs) to convert electromagnetic energy into heat. However, challenges related to the SPIONs coating's impact on their stability, the MH heating mechanism and the cell death mechanism, hinder MH from becoming a clinical standard.

The primary aim of this work is to explore diverse SPIONs coatings, assessing their stability, cell interactions, and the induced cell death mechanism.

This work presents a detailed characterization of SPIONs coated with three coating agents - oleic acid (OA), dimercaptosuccinic acid (DMSA), and (3-aminopropyl)triethoxysilane (APTES) and an evaluation of their stability across different conditions. Overall, OA- and DMSA-coated SPIONs exhibited similar behavior across various assays, including protein corona formation and hyperthermia tests. Over time, characteristics such as heating capacity decreased in the 3 types of SPIONs. APTES-coated SPIONs displayed higher protein corona formation. Interaction studies involving three cell lines (fibroblasts, melanoma, and macrophages) revealed enhanced internalization of APTES-coated SPIONs, with melanoma cells exhibiting lower internalization compared to fibroblasts and macrophages. In hyperthermia assays, only APTES-coated SPIONs achieved the therapeutic temperature range, reducing the melanoma cells viability.

This work underlines the critical role of the nanoparticles surface modifications used and highlights the multiplicity of factors that require consideration. However, additional research is essential for a better understanding of the cell death mechanism induced by MH and for its clinical translation.

Keywords: protein corona, superparamagnetic iron oxide nanoparticles, magnetic hyperthermia, melanoma, nanotechnology, stability.

The research work described in this dissertation was carried out in accordance with the norms established in the ethics code of NOVA University Lisbon. The work described and the material presented in this dissertation, with the exceptions clearly stated, constitute original work carried out by the author.

RESUMO

Atualmente, o tratamento de cancro é um foco de investigação devido às limitações das metodologias convencionais. Em particular, o melanoma maligno demonstra frequentemente resistência aos tratamentos.

A hipertermia magnética (HM) é uma terapia inovadora que se baseia na elevação de temperatura localizada para desencadear a morte de células tumorais, empregando nanopartículas superparamagnéticas de óxido de ferro (SPIONs) para converter a energia electromagnética em calor. Contudo, desafios como a influência que o revestimento das SPIONs tem na sua estabilidade, o mecanismo de aquecimento da HM e, especialmente, o mecanismo de morte celular, atrasam a evolução da HM para a prática clínica.

O principal objetivo deste trabalho consiste em explorar diferentes revestimentos de SPIONs, avaliando a sua estabilidade, interações celulares e o mecanismo de morte celular induzido.

Este estudo apresenta uma caracterização detalhada de SPIONs revestidas por ácido oleico (AO), ácido dimercaptosuccínico (DMSA) e (3-aminopropil)trietoxissilano (APTES) e uma avaliação da sua estabilidade em diferentes condições. SPIONs revestidas com AO e DMSA apresentaram um comportamento semelhante em diversos ensaios, incluindo nos testes de adsorção proteica e nos de HM. SPIONs revestidas com APTES apresentaram maior formação de proteína corona. Ao longo do tempo, a capacidade de aquecimento dos três tipos de SPIONs diminuiu. Estudos de interação envolvendo fibroblastos, melanoma e macrófagos revelaram uma maior internalização de SPIONs revestidas com APTES, com as células de melanoma a exibirem uma menor internalização. Nos ensaios de HM, somente as SPIONs revestidas por APTES atingiram o intervalo de temperatura terapêutico, reduzindo a viabilidade da linha celular de melanoma.

Este trabalho sublinha o papel crítico do revestimento e destaca a multiplicidade de fatores que exigem consideração. No entanto, mais estudos são necessários para uma melhor compreensão dos mesmos e para a translação clínica da HM.

Palavras chave: estabilidade, hipertermia magnética, melanoma, nanopartículas superparamagnéticas de óxido de ferro, nanotecnologia, proteína corona.

O trabalho de investigação descrito nesta dissertação foi realizado de acordo com as normas estabelecidas no código de ética da Universidade Nova de Lisboa. O trabalho descrito e o material apresentado nesta dissertação, com as exceções claramente indicadas, constituem trabalho original realizado pela autora.

CONTENTS

1. MOTIVATION 1

2. INTRODUCTION 3

2.1 Cancer 3

2.1.1 Melanoma 3

2.2 Hyperthermia 4

2.2.1 Magnetic Hyperthermia 4

2.3 SPIONs 6

2.3.1 Surface Modification 7

2.4 Cell Death 9

2.4.1 Cell Death by Magnetic Hyperthermia 9

3. MATERIALS AND METHODS 13

3.1 SPIONs 13

3.1.1 Synthesis 13

3.1.2 Surface Modification 13

3.1.3 Characterization 14

3.1.4 Stability Study 14

3.2 Cell Culture 15

3.2.1 Cytotoxicity Protocols 15

3.2.2 Internalization Study 15

3.3 Hyperthermia Studies 15

3.3.1 *In Vitro* Magnetic Hyperthermia 15

3.3.2 Sand Bath Hyperthermia 16

4. RESULTS AND DISCUSSION 19

4.1 SPIONs Characterization 19

4.1.1 FTIR 19

4.1.2 TGA 20

4.1.3 XRD 21
4.1.4 TEM 22
4.1.5 ζ-Potential and DLS Analysis 23
4.1.6 Magnetic Hyperthermia Analysis 24
4.2 SPIONs Stability 25
4.2.1 ζ - Potential 25
4.2.2 Protein Corona Formation 26
4.2.3 Magnetic Hyperthermia 28
4.3 SPIONs Cytotoxicity 30
4.4 SPIONs Internalization 32
4.5 Magnetic Hyperthermia 35
4.5.1 *In Vitro* Magnetic Hyperthermia 35
4.6 Sand Bath Hyperthermia 37

5. CONCLUSION AND FUTURE PERSPECTIVES 41

6. BIBLIOGRAPHY 45

A. SPIONS 57

A.1 Spectrophotometric Iron Determination by UV-Vis 57
A.2 Characterization 57
FTIR 57
TEM 58
XRD 58
TGA 58
DLS 58
Magnetic Hyperthermia 60
A.3 Protein Corona 60

B. CELL VIABILITY AND SPIONS INTERNALIZATION 63

B.1 Cytotoxicity protocols 63
Resazurin Assay 63
Live/Dead Assay 66
B.2 Internalization Study 66
Prussian Blue Staining 66
B.3 *In vitro* Magnetic Hyperthermia 71

LIST OF FIGURES

2.1 | Illustration of magnetic hyperthermia therapy. 5
2.2 | Biomedical applications of SPIONs. 6
2.3 | Magnetic hysteresis loops (applied magnetic field versus magnetization) for ferromagnetic, superparamagnetic, paramagnetic, and diamagnetic nanoparticles. 7
2.4 | Chemical structure of OA (A), DMSA (B) and APTES (C). 8

4.1 | FTIR spectra of SPIONs synthesized by chemical co-precipitation. 20
4.2 | TGA curves of SPIONs produced by chemical co-precipitation. 21
4.3 | X-ray pattern of SPIONs synthesized by chemical co-precipitation. 22
4.4 | TEM images and the corresponding size distribution graphs of SPIONs synthesized by chemical co-precipitation. 23
4.5 | Hydrodynamic diameter (A) and ζ-potential analysis (B) of SPIONs produced by chemical co-precipitation diluted in water. 24
4.6 | Temperature variation (A) and SAR values (B) of SPIONs produced by chemical co-precipitation in water for different concentrations. 25
4.7 | ζ-potential analysis of SPIONs at 5 mg/mL in water, PBS 1x and cell culture media. SP 26
4.8 | Analysis of the dynamics of PC formation in OA-coated SPIONs incubated for periods of 1 h, 6 h, 12 h and 24 h at 0.05 mg/mL in different media. 27
4.9 | Analysis of the dynamics of PC formation in DMSA-coated SPIONs incubated for periods of 1 h, 6 h, 12 h and 24 h at 0.05 mg/mL in different media. 27
4.10 | Analysis of the dynamics of PC formation in APTES-coated SPIONs incubated for periods of 1 h, 6 h, 12 h and 24 h at 0.05 mg/mL in different media. 28
4.11 | Evaluation of SPIONs stability at 5 mg/mL in water through analysis of temperature variation (A) and SAR values (B) over 6 months. 29
4.12 | Evaluation of SPIONs stability at 5 mg/mL in water, PBS 1x and DMEM HG + 10% FBS through analysis of temperature variation (A) and SAR values (B) at the end of the 1-month period. 30
4.13 | Resazurin cell viability assay of the HFFF2 (A), WM983b (B) and THP-1 (C) cell lines after 24 h of incubation with the three types of SPIONs produced. 31

4.14 | Live/Dead cell viability assay of the HFFF2, WM983b and THP-1 cell lines after 24 h incubation with APTES-coated SPIONs. 32
4.15 | SPIONs intracellular location in HFFF2 fibroblast cells after Prussian blue staining. 33
4.16 | SPIONs intracellular location in WM983b melanoma cells after Prussian blue staining. 34
4.17 | SPIONs intracellular location in THP-1 macrophage-like cells after Prussian blue staining..... 34
4.18 | Temperature curves of the three types of SPIONs in water at 5 mg/mL on a planar applicator. 35
4.19 | *In vitro* MH (A, C) and subsequent cell viability assays (B, D) of HFFF2 fibroblasts (A, B) and WM983b melanoma cells (C, D) incubated for 24 h with the different types of SPIONs. 36
4.20 | Cell viability of the three cell lines (HFFF2, WM983b and THP-1) after 1 hour of sand bath hyperthermia (41-44 °C). 37
4.21 | Fluorescence images of fibroblast HFFF2 cells stained with phalloidin (F-actin filaments in red) and DAPI (nucleus in blue) 3 h and 24 h after sand bath hyperthermia. 39
4.22 | Fluorescence images of melanoma WM983b cells stained with phalloidin (F-actin filaments in red) and DAPI (nucleus in blue) 3 h and 24 h after sand bath hyperthermia. 39
4.23 | Fluorescence images of THP-1 macrophage-like cells stained with phalloidin (F-actin filaments in red) and DAPI (nucleus in blue) 3 h and 24 h after sand bath hyperthermia. 40

A.1 | DLS Principle. 59

B.1 | Resazurin assay Principle. 63
B.2 | Resazurin cell viability assay of the HFFF2 (A), WM983b (B) and THP-1 (C) cell lines after incubation periods of 24 h and 48 h with the three types of SPIONs. 65
B.3 | SPIONs intracellular location in HFFF2 fibroblast cells after Prussian blue staining. 68
B.4 | SPIONs intracellular location in WM983b melanoma cells after Prussian blue staining. 69
B.5 | SPIONs intracellular location in in THP-1 macrophage-like cells after Prussian blue staining... 70
B.6 | Hyperthermia flasks before the *in vitro* MH assay.. 71

LIST OF TABLES

A.1 | Hydrodynamic size and ζ - potential of different syntheses of the three types of SPIONs in water at 5 mg/mL. 60

ABBREVIATIONS

AMF	Alternating Magnetic Field
Anti-CTLA4	Anti-cytotoxic T lymphocyte antigen-4
APTES	(3-Aminopropyl) triethoxysilane
ATR	Attenuated Total Reflectance
b.p.	Boiling point
DAPI	4’,6-diamino-2-phenylindone
Dh	Hydrodynamic Diameter
DLS	Dynamic Light Scattering
DMEM	Dulbecco’s Modified Eagle’s Medium
DMSA	Dimercaptosuccinic Acid
DMSO	Dimethyl sulfoxide
ER	Endoplasmic Reticulum
FA	Fatty Acid
F-Actin	Filamentous Actin
FBS	Fetal Bovine Serum
FDA	Food and Drug Administration
FWHM	Full width at half-maximum
FTIR	Fourier Transform Infrared
HEPES	4-(2-hydroxyethyl)-1-piperazineethanesulfonic acid
HG	High Glucose
HMGB1	High mobility group box-1
LG	Low Glucose
LMP	Lysosome Membrane Permeabilization
MH	Magnetic Hyperthermia
MILH	Magnetic Intralysosomal Hyperthermia
MFH	Magnetic Fluid Hyperthermia

MNP(s)	Magnetic Nanoparticle(s)
MRI	Magnetic Resonance Imaging
NCCD	Nomenclature Committee on Cell Death
NP(s)	Nanoparticle(s)
OA	Oleic Acid
PBS	Phosphate Buffer Saline
PC	Protein Corona
PDI	Polydispersity Index
PFA	Paraformaldehyde Fixation Buffer
PMAO	Poly (maleic anhydride-alt-1-octadecene)
RES	Reticuloendothelial System
ROS	Reactive Oxygen Species
RPMI	Roswell Park Memorial Institute
SAR	Specific Absorption Rate
(SP)IONs	(Superparamagnetic) Iron Oxide Nanoparticles
TEM	Transmission Electron Microscopy
TGA	Thermogravimetric Analysis
UV	Ultraviolet
XRD	X-Ray Diffraction

SYMBOLS

H	Applied Magnetic Field
H_c	Coercivity
M	Magnetization
M_r	Remanent Magnetization
M_s	Saturation Magnetization
f	Frequency
D_h	Hydrodynamic Diameter
C	Specific Heat
η	Viscosity
k_B	Boltzmann's Constant
T	Temperature
τ	Average Core Diameter or Delay Time
K	Scherrer's Constant
Abs	Absorbance
$D.F$	Dilution Factor
Γ	Decay Constant
n	Refractive Index
D	Diffusion Coefficient
q	Scattering Vector
m	Mass

1. MOTIVATION

Nowadays, cancer treatment encompasses diverse methods, including local approaches like surgery and radiation therapy, along with systemic treatments such as chemotherapy, immunotherapy, and targeted therapy, tailored to cancer type and stage. Despite these options, cancer remains a leading global cause of death and, in fact, almost everyone has a connection with someone who has had cancer, is fighting it or will fight it in the future. Its common treatments often yield side effects and may not halt disease progression. Therefore, a method with adaptability across cancer types, high specificity for cancer cells, and minimal side effects is needed.

In recent years, nanotechnology has displayed significant potential, particularly in the realm of medicine. Specifically, the use of nanoparticles (NPs) has emerged as a strategy to increase the effectiveness of cancer treatments, namely in drug delivery and magnetic hyperthermia (MH). MH is an innovative therapy that employs superparamagnetic NPs subjected to alternating magnetic fields (AMF) to induce cell death through localized heat generation. In the field of nanomedicine, this therapy has gained prominence for its advantageous aspects in effective antitumor treatment, including biosecurity, deep tissue penetration, radio-resistance reduction, and destruction of specific tumors. However, significant challenges need to be addressed for MH to fully exploit its potential as a viable alternative for cancer treatment.

When in physiological environments, NPs tend to lose stability, adsorbing proteins and aggregating and this can strongly affect their properties. To address this, NPs are typically coated with surfactants or other materials. However, selecting the right stabilizing agent remains a significant challenge since it ends up having a huge impact on several important factors such as the “bio-identity” of NPs, stability in physiological environment and cellular interactions. In addition, MH encompasses a broad spectrum of parameters that, when altered, can trigger different cell death pathways. This complexity contributes to the difficult and inconclusive nature of research into understanding the different cell death mechanisms that are induced by this therapy.

The main objective of the presented work is to explore different coatings for superparamagnetic iron oxide nanoparticles (SPIONs), assessing their stability, interactions with different cell types, and the induced cell death mechanism. For this purpose, this work can be divided into four specific aims:

1. Synthesis and characterization of SPIONs coated with three types of coating agents: oleic acid (OA), dimercaptosuccinic acid (DMSA), and (3-aminopropyl)triethoxysilane (APTES).

2. Evaluation of SPIONs stability over time and in various media, assessing hydrodynamic size, heating capacity, and protein corona (PC) formation.

3. Cell assays, including cytotoxicity and internalization studies, using three cell lines: fibroblasts, melanoma, and macrophages.

4. Hyperthermia studies and evaluation of cellular impact induced by temperature increase.

To the best of our knowledge, this is the first report to simultaneously compare the synthesis, characterization, and stability (evaluating PC formation, hydrodynamic size variation and heat capacity) of these three different NPs. Additionally, it is also the first to concurrently examine the interaction of the produced SPIONs with the three aforementioned cell lines, including assessments of potential cytotoxicity, internalization, and the effects of *in vitro* hyperthermia assays.

2. INTRODUCTION

2.1 Cancer

Cancer can be defined as a disease in which abnormal cells grow and divide without control. Nowadays, surgery, radiation, and chemotherapy are the three main treatments. Despite ongoing advancements, these anti-neoplastic therapies frequently result in a number of side effects and are not always successful in preventing the progression of the disease [2]. As consequence, cancer remains one of the leading causes of death worldwide and, according to the International Agency for Research on Cancer, there has been a notable escalation in the numbers. In 2018, around 18.1 million new cases of cancer were recorded, rising to around 19.3 million new cases in 2020 and forecasts point to a further increase to 30.2 million new cases by 2040. It should be noted that the 2020 statistics attribute almost 10 million deaths to this disease, which represents approximately one in six deaths, and projections predict that this figure will rise to 16.3 million in 2040 [3], [4]. These observations impose extreme emotional, physical, and financial pressure on individuals and their families, on communities and health systems, so the treatment of this disease has been an extremely challenging target of study worldwide [5].

2.1.1 Melanoma

Cutaneous melanoma is the most common subtype of melanoma and is a malignant neoplasm originating in melanocytes, which are melanin producing cells. Despite being a minority among skin cancers, its characteristics - such as highly invasive behavior, rapid recurrence, drug resistance and low survival rates - have established melanoma as the primary cause of over 80% of skin cancer deaths [6], [7]. Consequently, it is widely regarded as one of the most aggressive and lethal variations of skin cancer and, over the last five decades, has shown a significant prevalence increase when compared to other forms of malignant tumors [8]–[10]. Numerous risk factors for melanoma oncogenesis have been identified and the majority can be classified as inherited and environmental, with excessive ultraviolet (UV) light exposure being the most significant one [7].

Currently, the primary methods used to treat this type of cancer include surgery, chemotherapy, and immunotherapy, however, these approaches face limitations such as late diagnosis and off-target administration. The commonly used clinical drugs for melanoma treatment, namely doxorubicin (DOX), vemurafenib, and paclitaxel, lack site-specificity and often encounter resistance from melanoma cells [8]. Furthermore, melanoma is a heterogeneous disease, meaning that it exhibits diverse responses to

anticancer drugs, consequently, personalized treatment approaches are necessary to cater to the specific needs of each patient [11]. That said, therapeutic strategies for melanoma have been at the forefront of personalized medicine, with increasing attention in recent years on targeted approaches. Among these, some methods include MH (usually combined with other therapies) and the convergence of molecular targeted therapy with immune checkpoint inhibition (with the combination of nivolumab and ipilimumab being one of the most studied within this context) [12]–[16].

2.2 Hyperthermia

As the name implies, the term "hyperthermia" means heat generation and, when associated with cancer treatment, this heat production essentially occurs at the tumor site [17]. Supported by Greek philosophy which extols the qualities of fire, the first documentation of this technique, represented using cautery, was performed by Hippocrates for the treatment of breast tumors. However, it was in the 19th century with the investigations of Busch and Coley that a better understanding of how the application of heat affected the tumor tissue was achieved, in these cases through the generation of artificial fever by infections and toxins, respectively [18]–[20].

Nowadays, hyperthermia treatment can be categorized based on the extent of the temperature increase and depending on the location of the disease, and these are generally related. First, regarding the whole-body hyperthermia, it involves lower temperatures ($T < 41$ °C) and serves to mimic the febrile process being usually used in the treatment of metastases. The local therapy, also known as thermal ablation, is the one that achieves the highest temperatures ($T > 46$ °C), and its goal is usually the total ablation of the tumor by inducing direct tissue necrosis, coagulation, or carbonization. Large energy absorption, however, may result in harmful outcomes on the surrounding healthy cells. Concerning regional hyperthermia, it entails the application of heat to more extensive areas such as whole tissue and organs and the temperature range is about 41- 46 °C. This milder rise in temperature is usually combined with chemotherapy or radiation therapy and can limit some of the collateral damage to normal tissues beyond the ablation zone [21], [22].

2.2.1 Magnetic Hyperthermia

Nanotechnology is a multidisciplinary field that has been growing in recent years and consists of the manipulation of a broad spectrum of materials with at least one dimension in the range of 1 to 100 nm. NPs, nanotubes, nanowires, and quantum dots are some of the different types of nanomaterials that are highly promising for a variety of applications, since they have unique characteristics (mainly due to their small size and high surface-to-volume ratio). The current nanotechnology era, especially in the field of nanomedicine, is marked by the emergence of various magnetic NPs (MNPs) and their size, chemical composition, morphology, and magnetic properties are key determinants of their applications. Typically composed of pure metals (iron, cobalt, and nickel), metal alloys or metal oxides, MNPs possess an important feature - they can be magnetically controlled by an external magnetic field [23].

MH is a therapeutic approach that involves the use of MNPs to induce controlled heating in the targeted tissues. Therefore, as depicted in Figure 2.1, it is based on the integration of two primary elements: injectable MNPs and a magnetic field generator, both of which normally hold medical device approvals [24]. Successful heating relies on the appropriate amplitude and frequency of the AMF, where the frequency should exceed the MNPs relaxation time for effective heat dissipation. However, in biomedical contexts, the product of magnetic field strength and frequency (H × f) must stay below 5×10^9 $Am^{-1}s^{-1}$ to prevent adverse effects [25], [26].

Nowadays, most MNPs used in hyperthermia applications, whether experimental or commercially available, are predominantly SPIONs according to MagForce® and Sennewald. This preference is due to the stringent requirements of biocompatibility, non-toxicity, ability to evade the reticuloendothelial system (RES), and low protein adsorption for MNPs intended for biomedical use [27], [28]. That said, SPIONs, due to all their characteristics mentioned above, their magnetic field-guided functionality, biocompatibility and theranostic potential, are at the forefront of nanomedicine tools [29].

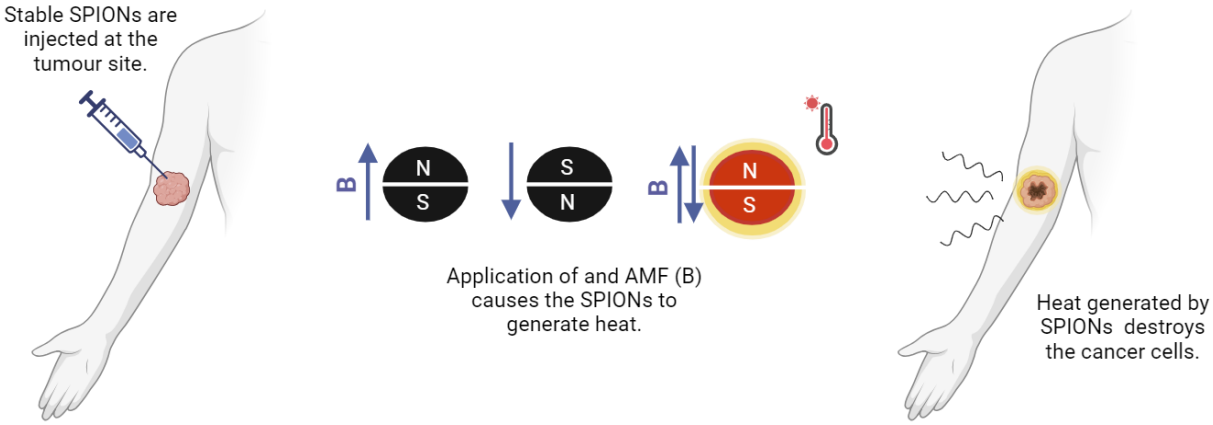

Figure 2.1 | **Illustration of magnetic hyperthermia therapy.** Magnetic hyperthermia treatment utilizes MNPs and an AMF to selectively raise the temperature of cancer cells, leading to their targeted destruction while minimizing harm to healthy tissue, holding significant promise in the field of cancer treatment. Adapted from [30].

MH can be traced back to 1957, when Gilchrist and colleagues selectively heated tumors in lymph nodes using an AMF and iron oxide NPs (IONPs) [31]. In the 1990s, after extensive studies with magnetic fluids, Jordan A. and colleagues proposed the term "magnetic fluid hyperthermia" (MFH) as a novel cancer therapy [32]. Since then, numerous publications have described various approaches, with different magnetic materials, synthesized in different ways and using different field strengths and frequencies. The first pre-clinical trials in patients were initiated by Jordan *et al.* and, in 2001, this group introduced a whole-body magnetic field applicator for clinical MFH [33]. This therapy consists of the injection of aminosilane-coated IONPs which they called NanoTherm®, a real-time temperature simulation software called NanoPlan® and an AMF applicator, the NanoActivator® [34], [35]. The therapeutic potential of this technique has been clinically validated in glioblastoma multiforme and prostate carcinoma, both in synergy with other therapies and as monotherapy and, up to now, is the only metallic-based cancer therapy that has received both FDA and EMA approval [33], [36]–[41].

2.3 SPIONs

One of the most studied types of MNPs, especially in cancer therapy, are IONPs due to characteristics such as high chemical and colloidal stability, high biocompatibility, low cost and, as nanoscale entities, the ability to accumulate at the tumor site [42], [43]. That said, as illustrated in Figure 2.2, this type of NPs have been used in a variety of applications such as drug delivery agents, contrast agents for biomedical imaging, and MH agents [44]–[49].

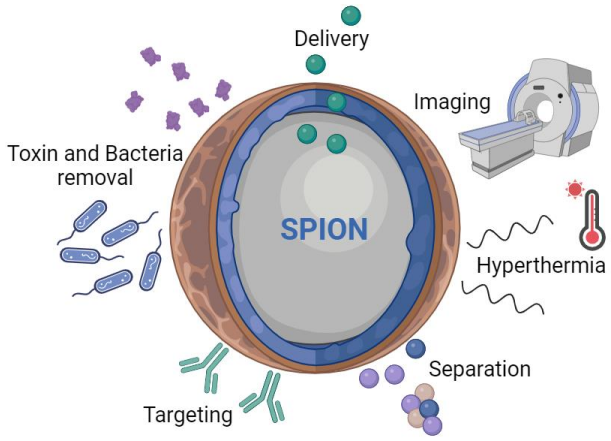

Figure 2.2 | **Biomedical applications of SPIONs.** SPIONs find versatile utility across numerous applications, including drug delivery, toxin and bacteria removal, targeting, magnetic hyperthermia, and serving as contrast agents for biomedical imaging. Adapted from [50].

From all IONPs, the most common magnetic materials that compose the core of IONPs are magnetite (Fe_3O_4), maghemite (γ-Fe_2O_3), and hematite (α-Fe_2O_3), which differ in their chemical composition, crystal structure, stability, and magnetic properties. For biomedical applications, magnetite is the one that stands out, since its properties allow it to exhibit an important property, superparamagnetic behavior [51]. Figure 2.3 represents the hysteresis loops of different forms of magnetism. A hysteresis loop is described by the variation of the degree of magnetization (B) with the magnetic field strength (H). This B-H relationship is directly associated with two parameters: coercivity, which is the magnetic field required to reduce the magnetization to zero, and remanence, or remanent magnetization, which represents the residual magnetization when a field is removed. Due to the total absence of these two parameters, superparamagnetic materials, such as SPIONs, can only be magnetized when an external magnetic field is applied, and this magnetization occurs because, in the presence of this field, the magnetic moments align in the field direction [52], [53]. This behavior is a result of the material's distinct magnetic domain, which is normally attained when the NP size is below approximately 15 nm at room temperature [54]. During the demagnetization process, magnetic moments undergo relaxation, known as Brownian and Néel relaxations, leading to the dissipation of energy in the form of heat. This particular property of SPIONs holds significant importance and is extensively investigated for MH treatments [53]. The presence of this unique magnetic domain and the ability to reverse the orientation of their magnetic dipoles contribute to a significant increase in their magnetic susceptibility. Consequently, they

have the capacity to absorb significantly more energy (per unit mass) than larger multidomain particles when subjected to AMFs suitable for physiological applications [55].

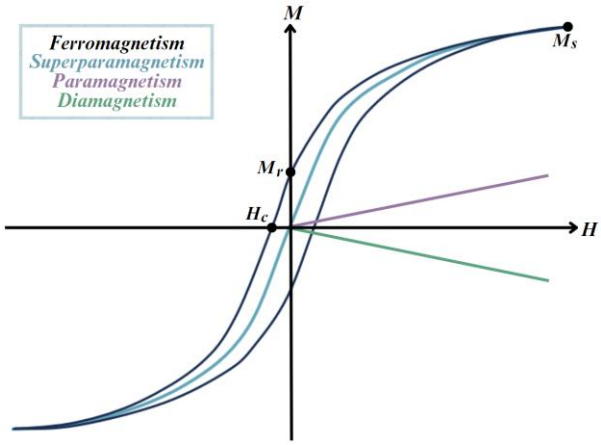

Figure 2.3 | **Magnetic hysteresis loops (applied magnetic field versus magnetization) for ferromagnetic, superparamagnetic, paramagnetic, and diamagnetic nanoparticles**. (H_c - Coercivity; M_r - Remanent magnetization; M_s - Saturation magnetization) Adapted from [56].

2.3.1 Surface Modification

SPIONs surface modification is a strategy employed for diverse purposes. These include providing a reactive surface for functionalization purposes, protection against RES clearance, mitigation of potential cytotoxicity, and prevention of aggregation or oxidative stress [26], [54], [57], [58].

Regarding the aggregation of uncoated SPIONs, it tends to occur under neutral pH conditions. This is primarily because, at physiological pH levels, the particle's charge approaches zero, reducing the repulsive interactions between NPs and leading to their aggregation [59], [60]. To prevent this, and as aforementioned, SPIONs are typically coated to enhance their stability. However, biological fluids consist of various components, including charged proteins, which can interact with the NPs through an adsorption process. This adsorbed layer of proteins is commonly known as PC, and holds significant implications for the properties and behavior of the NPs [61], [62]. Nevertheless, it is crucial to consider that different stabilizing coating agents, depending on the surface charge they provide to the particles, can result in varying degrees of protein adsorption [63]. Calatayud *et al.* conducted a study wherein they compared the hydrodynamic size differences of negatively and positively charged MNPs when immersed in a biological medium [64]. Following a 24-hour incubation period, the research group observed substantial disparities between the two types of NPs. Positively charged particles exhibited a hydrodynamic size of approximately 3000 nm, while negatively charged particles measured around 1500 nm. However, in addition to NP-protein interactions, it's worth noting that there can also be interactions among proteins, referred to as "protein-mediated bridging," which can, in turn, result in the aggregation of NPs [61].

In the context of SPIONs, preventing aggregation is particularly important. When SPIONs aggregate, they cease to exhibit the characteristics of single-domain particles and, instead, become

permanently magnetized assemblies, thereby losing their superparamagnetic properties. This is particularly problematic in MH applications, since these aggregates compromise the SPIONs' heating capacity and, therefore, the MH efficacy [55]. Guibert C. *et al.*, studied the role of aggregation in the heating capacity of IONPs [65]. Among their findings, the group evaluated the variation of the specific absorption rate (SAR), a critical parameter in MH that measures the material's capability to convert alternating magnetic energy into heat. They were able to observe that the SAR values of NPs in small aggregates is similar to that of well-dispersed NPs, while the formation of large aggregates results in a significant decrease in SAR values. Additionally, they concluded that the degree of compactness within the aggregates plays a crucial role, as closer proximity between NPs leads to a more pronounced decrease in heating efficiency. Therefore, SPIONs surface modification with polymers, surfactants or other stabilizing agents is essential to maintain their intrinsic characteristics. Some examples of coating agents employed for surface functionalization of NPs include OA, DMSA and APTES (Figure 2.4).

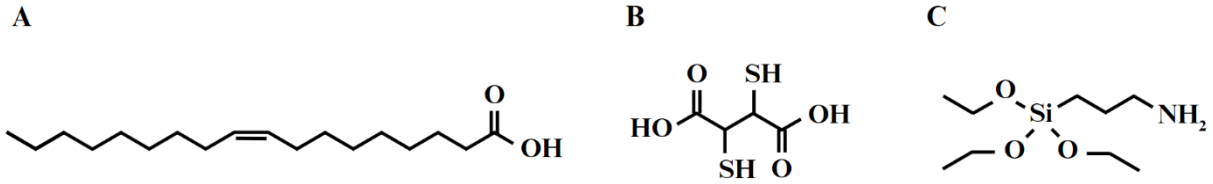

Figure 2.4 | **Chemical structure of OA (A), DMSA (B) and APTES (C).**

OA, a monounsaturated fatty acid (FA), is a common surfactant for surface modification and stability enhancement due to its high affinity for the surface of SPIONs. Stabilization of the particles is achieved by the formation of strong chemical interactions between the positive surface of the NPs and the carboxylic acid of the OA, as well as by repulsion between the OA chains [66]. The literature presents the most varied applications of OA, from inhibition of ferroptotic cell death to improvement of hepatocellular lipotoxicity (by inhibiting endoplasmic reticulum (ER) stress and pyroptosis) [67]–[69]. Overall, OA is considered highly resistant to oxidation and is able to increase the activity of antioxidants (e.g., tocopherols). Regarding SPIONs coated with this compound, numerous studies have been conducted, exploring their potential applications for example in MH, in drug release, and imaging [49], [70], [71].

DMSA, a dithiol, is a derivative and analog of the compound dimercaprol containing two sulfhydryl (-SH) groups. Approved by the FDA in 1989, DMSA is a compound with low toxicity with several applications including the treatment of heavy metal poisoning and the coating of MNP surfaces (being one of the most studied compounds in this last domain) [72], [73]. When the DMSA molecules surrounding the SPIONs are oxidized, they form a cage of disulfide cross-linked DMSA molecules around the core of the NPs and this process leads to an abundance of carboxylate groups on the particle surface, resulting in a negative surface charge, thereby increasing the colloidal stability of the SPIONs in aqueous solutions [74].

APTES is used in a variety of applications and is considered one of the most used organosilanes to promote the interfacial behavior of inorganic oxides, including SPIONs. The functionalization with APTES introduces amino groups on the surface of the NPs opening numerous possibilities for

applications ranging from cell and enzyme separation to diagnostics, drug delivery, and MH [75]. According to the literature, this compound not only improves the colloidal stability of NPs, but also demonstrates higher cell internalization efficiency when compared to other surface coatings [76].

2.4 Cell Death

Recently, the Nomenclature Committee on Cell Death (NCCD) has been formulating guidelines for both define and interpret cell death [77]. The initial morphological classification of cell death encompassed three types: type I cell death (apoptosis), type II cell death (autophagy), and type III cell death (necrosis). However, as scientific research has advanced, diverse novel cell death modalities have since been identified and characterized based on their stimuli, morphological features and molecular mechanisms. Among the current 12 modalities, some share overlapping signaling pathways, yet they are not entirely identical and cannot be neatly incorporated into the traditional type I-III categories [78]. Due to the complexity of this subject, this work will mainly discuss two distinct forms of cell death: necrosis and apoptosis.

Apoptosis stands out as a primary form of programmed cell death, meticulously regulated to induce cellular self-destruction. This orchestrated mechanism entails a sequence of events including cell shrinkage, chromatin condensation (pycnosis), nuclear fragmentation (karyorexia), and plasma membrane blebbing. Ultimately, this process culminates in the formation of small vesicles, termed apoptotic bodies, that are efficiently recognized and absorbed by neighboring phagocytic cells and degraded within the lysosomes [77]. Notably, distinct from other modes of cell death, apoptosis relies on the activity of caspases, and it can be triggered via three pathways: the extrinsic pathway involving death receptors, the intrinsic pathway linked to mitochondria, and the accessory extrinsic pathway involving the perforin/granzyme mechanism. On the other hand, necrosis represents an unregulated form of cell death triggered by external factors and typically involves premature cell death. Characteristic traits of this type of cell death encompass cellular swelling, increased cytoplasmic granularity, inflammation, plasma membrane rupture, and the consequent loss of intracellular organelles. Unlike apoptosis, necrosis lacks pronounced chromatin condensation but involves indiscriminate deoxyribonucleic acid (DNA) degradation [78], [79].

2.4.1 Cell Death by Magnetic Hyperthermia

In the realm of biomedical applications, particularly in cancer treatment utilizing MH, apoptosis gains preference due to its inherent attributes that end up safeguarding neighboring healthy cells. That said, it is essential to heed the temperature threshold that can incite the necrotic mechanism (usually above 45 - 46 °C where the so-called thermo-ablation occurs) [80]. Since cancer cells have a higher sensitivity to hyperthermia compared to normal cells, they go into controlled cell death, not affecting healthy cells. This is also favored by the fact that healthy tissues usually are able to withstand this therapeutic temperature range between 41- 45 °C [81].

After exposure to hyperthermia treatment, a broad spectrum of cellular transformations becomes evident. These encompass modifications in cell membrane characteristics, metabolic processes, nuclear components, cytoskeletal structure, macromolecular synthesis, the upregulation of heat shock genes, and intracellular signaling events [82]. Yet, despite the persistent uncertainty surrounding the specific mechanisms by which hyperthermia induces cell death, prevailing thought asserts that the primary and most immediate impacts of hyperthermia toxicity involve the denaturation of proteins and damage to the cell membrane [81]. In fact, it has been observed a close resemblance between the thermal energy necessary for triggering cell death and the energy required for protein denaturation [83].

In addition to the observable modifications in membrane integrity and the resulting cytoskeletal impairment, an additional pivotal outcome of protein denaturation lies in the disruption of DNA synthesis and repair processes. According to the literature, cells undergoing mitosis have been documented to exhibit heightened sensitivity to heat, making cancer cells notably more responsive to this effect [81]. Another contributing factor to the heightened sensitivity of tumor cells to heat arises from their disorganized and abnormal vasculature architecture, notably distinct from healthy tissue. This anomalous architecture results in reduced blood flow within tumor tissue, thus hindering effective heat dissipation and impeding the supply of oxygen and essential nutrients. In addition, NPs exhibit a tendency to accumulate preferentially in neoplastic tissues. This preferential accumulation is attributed to their selective permeability through the tumor's vasculature, where they are subsequently retained due to diminished lymphatic drainage. This phenomenon is commonly recognized as the enhanced permeabilization retention effect (EPR) [81], [84].

2.4.1.1 Literature review

Cell death mechanisms should not be considered exclusive, so it is plausible to consider that a given stimulus could trigger a combination of events. Within MH there is a wide range of parameters which, when varied, lead to the activation of diverse cell death pathways and this is reflected in the difficulty and lack of consensus observed in this field.

Oh. Y., *et al.* in an *in vitro* MH assay using chitosan-$MnFe_2O_4$ on a breast cancer line observed that at 42 °C the cells showed significant and irreversible alterations in their morphology [85]. The group concluded that the disruption of the cytoskeleton and nucleus of cancer cells eventually led to the induction of apoptosis at this temperature, and in fact, several studies document the association between the apoptotic process and cleavage and disruption of the cytoskeleton (particularly actin filaments) [86]–[88]. Nonetheless, at 52 °C, the group observed the direct induction of necrotic cell death without any observable apoptotic process.

In a study conducted by Salimi. M. *et al.*, the group functionalized SPIONs with polyamidoamine dendrimers (PAMAM) for MH in breast cancer [89]. Their research revealed that MH induced the intrinsic apoptosis pathway in treated cancer cells, with an observed increase in the pro-apoptotic protein Bax. In addition, they observed that in mice the treatment reduced mammary gland tumor growth by suppressing tumor angiogenesis and promoting cell necrosis.

As previously stated, cancer treatment frequently involves the strategic combination of therapies to achieve a synergistic effect. Salvador D. *et al.* combined DOX and hyperthermia on the human melanoma cell lines A375 and MNT-1 [90]. They concluded that hyperthermia led to an increase in the effect of DOX through oxidative stress, cell cycle arrest (in the G2/M phase), and apoptotic cell death. Recently, Duval K. *et al.* used Bionized NanoFerrite IONPs to evaluate the effects of MH on B16-F10 murine melanoma cells [91]. Regarding the induced apoptosis pathways, the results showed that both pro-apoptotic and anti-apoptotic changes were stimulated. However, the synergistic combination with radiation immunity-related mRNA expression proved to be the most effective stimulator of a wide variety of immune and cytotoxic genes. That said, the combination of MH with other immunotherapeutic approaches has been widely explored. Chao *et al*. combined MH with immune checkpoint blockade immunotherapy to achieve whole-body therapeutic responses after local treatment [92]. They observed that thermal ablation using IONPs resulted in high expression of high mobility group box-1 (HMGB1), an immunogenic cell death marker, in the remaining tumors. The group then administered anti-cytotoxic T lymphocyte antigen-4 (anti-CTLA4) to induce systemic immunity resulting in metastasis inhibition.

Furthermore, according to the literature, cancer cells are more susceptible to lysosome membrane permeabilization (LMP), which can be explained by differences in composition and morphology. For example, it is now known that, when compared to normal cells, tumor cells have larger lysosomes and a higher concentration of cathepsins, which are hydrolytic enzymes that can potentially degrade vital cellular components, inducing cell apoptosis or, if the damage is significant, necrosis [93]–[95]. That said, it has been found that LMP can also trigger cell death and numerous studies have used Magnetic Intralysosomal Hyperthermia (MILH) to induce this process [96], [97]. Clerc *et al.* employed this technique using SPIONs modified with gastrin and identified cell death occurring through a non-apoptotic signaling pathway [98]. This demise was attributed to the localized temperature increase at the periphery of the SPIONs. This rise in temperature prompted the lysosomal Fenton reaction, leading to the generation of reactive oxygen species (ROS) and subsequently lipid peroxidation, culminating in LMP and the subsequent release of lysosomal enzymes including cathepsins [25], [96].

In a study conducted by Beola *et al.*, using SPIONs internalized in macrophages, distinct localized temperatures were observed [99]. These temperatures were directly linked to the fluctuations in the quantity of internalized NPs within the lysosomes, as well as the vesicle size. The outcomes led them to hypothesize that this phenomenon might be linked to varying rates of heat transfer through the vesicle wall, but further research is needed. In addition, they also observed that the number of internalized NPs influenced the activation of distinct apoptotic pathways. At lower concentrations of SPIONs, the intrinsic apoptotic mechanism predominated and at higher concentrations the extrinsic route became the main mechanism. Apart from the investigation focused on lysosomes, the elevation of subcellular temperatures has gained significant prominence. Shah *et al.* showcased that hyperthermia specifically targeted at mitochondria also induced apoptosis in cancer cells [100].

3. MATERIALS AND METHODS

3.1 SPIONs

3.1.1 Synthesis

The synthesis of SPIONs was accomplished through a chemical co-precipitation technique, adapted from the method originally described by Soares *et al.* [66]. This method is commonly used for SPIONs synthesis due to its simplicity and productivity. In short, it consists of an ammonia-triggered reaction and precipitation of ferrous and ferric chlorides ($FeCl_2$ and $FeCl_3$, respectively) forming NPs. The complete chemical reaction is depicted in Equation (3.1):

$$Fe^{2+}(\mathrm{aq}) + 2\mathrm{Fe}^{3+}(\mathrm{aq}) + 8\mathrm{OH}^{-}(\mathrm{aq}) \rightarrow \mathrm{Fe_3O_4} + 4\mathrm{H_2O}\ (\mathrm{l}) \quad (3.1)$$

In this work, to create 1 and 2 M solutions, the ferrous chloride (Alfa Aesar) and ferric chloride (Sigma-Aldrich) were dissolved in 10 mL and 2.5 mL of MiliQ water respectively. The iron mixture was then diluted with 50 mL of water achieving a molar ratio of 1:2 (Fe^{2+}: Fe^{3+}). The mixture was then placed under magnetic stirring at 600 rpm and with bubbling N_2 in order to avoid oxidation of the particles. Furthermore, 10 mL of NH_4OH 25% (VWR chemicals) was added quickly while being vigorously stirred for 5 minutes. Finally, to stop the reaction, 60 mL of MiliQ water were introduced. The 1,10-phenanthroline colorimetric method was used to quantify the amount of iron from each SPIONs synthesis afterward [66], [101]. The method's procedure is provided in Appendix A.1.

3.1.2 Surface Modification

3.1.2.1 Stabilization with OA

For this work, the procedure followed for stabilization with OA is described in P.I.P. Soares *et al.* [66]. Briefly, after synthesis, the SPIONs were allowed to settle via magnetic attraction, forming a precipitate, and the upper layer of water was discarded. Then, a known volume of the SPIONs colloid was mixed with OA (Panreac), 64 mM, where the amount of OA to be utilized was obtained by applying a factor of 64% and taking into account the mass of the SPIONs. Then, the mixture was left to react for about 2.5 hours in an ultrasound bath. Finally, in order to release the OA that did not interact, the stabilized SPIONs were subjected to dialysis using a 4 RC 12 to 14 kDa MWCO Dialysis Membrane Tube 4 RC (Spectrum™ Spectra/Por™). MilliQ water was employed for the dialysis, with periodic water changes, until the pH of the final suspension reached a neutral level.

3.1.2.2 Stabilization with DMSA

The surface modification using DMSA in this work was adapted from Fauconnier N. *et al.* [102]. Briefly, post-synthesis, the SPIONs were allowed to settle via magnetic attraction, forming a precipitate, and the upper layer of water was discarded. Afterward, underwent five washes with MiliQ water through magnetic separation and then an oxidation procedure was done to increase solution stability. In order to oxidize the SPIONs, the solution's pH was adjusted to 3 using 65% nitric acid (Panreac) while being magnetically stirred. DMSA was first dissolved in 2 mL of MiliQ water, and the pH adjusted to 5.5 using a 0.1 M NaOH solution (Eka Chemicals) with vigorous stirring. Following this, DMSA (Acros Organics) was added at a ratio of 3:4 of [DMSA]/[Fe^{2+}] and the reaction proceeded for approximately 2.5 hours within an ultrasound bath. Finally, to eliminate unbound DMSA, the NPs underwent dialysis using a 4 RC 12 to 14 kDa MWCO Dialysis Membrane Tube (Spectrum™ Spectra/Por™), and here MiliQ water was used to do dialysis water changes until the final suspension's pH was neutral.

3.1.2.3 Stabilization with APTES

In this work, the stabilization with APTES was carried out according to the method described by Mashhadizadeh H. *et al.* [103]. Briefly, the prepared SPIONs suspension was allowed to settle to separate the supernatant and an aqueous solution containing 10 % (v/v) APTES (Merck) and glycerol, in a ratio of 1:2, was added. Then, for 2 hours, this mixture was left to react at 90 °C with mechanical stirring. Finally, the suspension underwent five washes with water and ethanol, after cooling to room temperature.

3.1.3 Characterization

Fourier transform infrared (FTIR), thermogravimetric analysis (TGA), X-ray diffraction (XRD), transmission electron microscopy (TEM), and dynamic light scattering (DLS), were used to analyze the stabilized synthesized SPIONs. To evaluate the heating capacity of the SPIONs, MH assays were performed. DLS technique was also used to perform a PC formation assay by measuring the hydrodynamic diameter (Dh) and ζ-potential of the samples at different time points. All sample preparations for the various techniques are specified in Appendix A.2 and in Appendix A.3.

3.1.4 Stability Study

To study the SPIONs stability, new syntheses were conducted, and the particles were characterized in various dispersion media, including MiliQ water, phosphate buffer saline (PBS), NaCl, and high glucose Dulbecco's Modified Eagle's Medium (DMEM-HG, Biowest). The characterization involved assessing their Dh and ζ-potential using DLS, as well as their heating capacity. To determine the surface charge of the SPIONs, a graphite electrode cell was utilized, and measurements were conducted using an SZ-100 nanoparticle array (Horiba, Lda) with a 532 nm laser. Additionally, the heating capacity of the synthesized NPs was assessed. At the concentrations of 1, 2.5, 5 and 10 mg/mL the temperature of the sample was measured using an Nb Nanoscale Biomagnetics D5 equipment with a magnetic field strength of 300 Gauss and a frequency of 388.4 kHz. In each sample, a temperature stabilization period

of about 30-40 seconds without an applied field was used followed by 10 minutes of applied field. The above characterization of the SPIONs in water was conducted at the time of synthesis and repeated after 1, 3, and 6 months to assess the stability and the ability of the SPIONs to retain their characteristics over time.

3.2 Cell Culture

Three cell lines were used for the different cell assays: advanced cutaneous melanoma cancer cells WM983b (Rockland), human Caucasian fetal foreskin fibroblast cells HFFF2 (ECACC 86031405) and a human leukemia monocytic cell line THP-1 (ATCC TIB-202™). The WM938b cell line was grown in DMEM-HG supplemented with 1% penicillin-streptomycin (P/S, Gibco) and 5% heat-inactivated fetal bovine serum (FBS, Biowest). The HFFF2 cell line was grown in low glucose DMEM medium (DMEM-LG, Biowest) supplemented with 1% P/S and 10% FBS (Biowest). Lastly, the THP-1 cell line was grown in Roswell Park Memorial Institute (RPMI, Biowest) medium supplemented with 1% P/S, 10% heat-inactivated FBS, 1% of sodium pyruvate and 1% of non-essential amino acids (both from Gibcon). The three cell lines were maintained in an MCO-19AIC(UV) CO_2 incubator (Sanyo) with a humidified atmosphere of 5% CO_2 at 37 °C.

3.2.1 Cytotoxicity Protocols

The resazurin and Live/Dead assays were the two cell viability tests used to evaluate cell viability of the three cell lines in the presence of the coated SPIONs. The procedures followed are described in Appendix B.1.

3.2.2 Internalization Study

The uptake of SPIONs by the three cell lines was determined based on the Prussian blue staining technique. For this assay, WM983b, THP-1 and HFFF2 cells were exposed to the SPIONs for 1 h, 6 h and 24 h at a concentration of 100 μg/mL (protocol in Appendix B.2).

3.3 Hyperthermia Studies

Before proceeding to *in vitro* MH, the heating capacity of the SPIONs was tested in a planar applicator at a 300 G AMF at a frequency of 388.4 kHz for 10 min. The three different types of SPIONs were diluted in water at a concentration of 5 mg/mL and the assay was conducted in a nB nanoScale Biomagnetics D5 series device.

3.3.1 *In Vitro* Magnetic Hyperthermia

For the *in vitro* MH assay 500k cells/mL and 450k cells/mL of WM983b and HFFF2 respectively were seeded in hyperthermia vials and left to incubate for 24 h. After this the different types of SPIONs were added at a concentration of 5 mg/mL diluted in the corresponding cell medium with

gentamicin antibiotic (Gilbco) at a ratio of 1:1000 from a stock solution of 10 mg/mL and the vials were incubated again for 24 h.

All MH assays were performed on a nB nanoScale Biomagnetics DM100 series apparatus, using samples with a volume of 1 mL. To achieve the desired temperature range, the configuration used consisted of applying a 300 G AMF at a frequency of 388.4 kHz until a temperature of 45 °C was reached or until 25 min of heating was achieved. For this study, 3 controls were performed per assay, one SPIONs control (unheated vial with SPIONs and cells), and two cell controls (without NPs), one accompanying the vials to be measured and the other kept in a CO_2 incubator MCO-19AIC(UV) (Sanyo) with a humidified atmosphere of 5% CO_2 at 37 °C.

Following the MH treatment, each flask was rinsed 2x with the respective cell culture medium and 500 µL of the previously prepared resazurin solution (50% resazurin plus 50% complete medium) was subsequently added to each flask in order to measure the metabolic activity of cells in response to treatment. The flasks were then left to incubate for a period of approximately 2 h in order to provide adequate fluorescence while avoiding signal saturation. Once the incubation time had elapsed, the solutions from the flasks were transferred to a non-sterile 96-well cell culture plate. Additionally, 1 mL of cell culture medium and gentamicin at a 1:1000 ratio from a 10 mg/mL stock solution were re-introduced into each flask for the resazurin assay to be repeated 24 h later. Absorbance values were measured at wavelengths of 570 and 600 nm using the BioTek ELx800 UV absorbance microplate and cell viability was expressed as a percentage of the control, given by [% cell viability = test cells/incubator control cells × 100].

3.3.2 Sand Bath Hyperthermia

For this assay the three cell lines were seeded separately in a 24-well plate maintaining the cell density used for the resazurin assay. After the cells were adhered, 500 µL of SPIONs coated with APTES at a concentration of 100 µg/mL were added and the plate was incubated again for a period of 24 h. After this period, the plate was placed in a sand bath for 1 h at a temperature range of 41- 44 °C. Immediately after hyperthermia, a solution of resazurin (Alfa Aesar) with concentration of 0.04 mg/mL was placed on the wells to get a final resazurin concentration of 0.02 mg/mL and the plate was incubated again for a period of approximately 2.5 hours in order to avoid signal saturation. After this time, 100 µL of the solutions from each well were transferred to a non-sterile 96-well cell culture plate before reading to minimize any potential influence of the SPIONs' color on the absorbance values. The absorbance was then measured at 570 and 600 nm wavelength using the BioTek ELx800 UV absorbance microplate reader and cell viability was expressed as a percentage of the control (plate that was not heated), given by [% cell viability = NP treated cells/control cells × 100]. After this, half of the replicates were fixed, and the other half were placed with 400 µL of the respective medium in each well and underwent an additional 24-hour incubation (the steps outlined below were reiterated with this samples after this time interval). For the fixation process the cells were washed 4x with PBS and 400 µL/well of 4% paraformaldehyde (PFA, Sigma Aldrich) was added. After a period of about 15 minutes, the cells were washed 3x with PBS and then permeabilized with 400 µL of 0.5% Triton-X 100 for 20 min. After being washed

with PBS the cells were then stained with Actin-staining™ 555 Phalloidin Red (Cytoskeleton) dissolved in 0.2% PBS solution at 100 nM. Each coverslip was covered with 50 µL of the staining solution for 1.5 hours. Then, each coverslip was washed with PBS and nuclear staining was performed by adding 50 µL of a 10 µM 4',6-diamino-2-phenylindone (DAPI, Molecular Probes) solution dissolved in the PBS solution and left to act for about 3-4min. After this staining the coverslips were washed with PBS and water and mounted on slides on 10 µL of Mowiol mounting medium (Sigma-Aldrich). The samples were visualized with an epi-fluorescence microscope Nikon Eclipse Ti-S.

4. RESULTS AND DISCUSSION

4.1 SPIONs Characterization

4.1.1 FTIR

OA, DMSA and APTES coated SPIONs were studied with FTIR to characterize the chemical transformations occurring during the various surface modifications and to identify characteristic bands related to the prevalent functional groups. Measurements obtained between wavelengths of 500 and 4000 cm^{-1} are shown in Figure 4.1.

In all three spectra presented, the presence of the three characteristic bands of SPIONs is evident. The strong absorption band at approximately 550 cm^{-1} corresponds to the Fe-O stretching vibration mode while the band at 1590 cm^{-1} is attributed to the O-H stretching vibration modes of the NPs. Finally, the broader band between 3000 cm^{-1} and 3500 cm^{-1} is associated with the O-H stretching vibration mode due to water [26].

Regarding the FTIR spectrum of OA coated SPIONs, the sharp peaks at approximately 2921 and 2851 cm^{-1} represent the symmetric and asymmetric -CH_2 stretching in the OA molecule, respectively. The band at 1709 cm^{-1} corresponds to the C=O stretching vibration and indicates the formation of an OA bilayer. This bilayer is significant as it imparts hydrophilicity to the SPIONs, enhancing their stability in aqueous solutions. Additionally, bands at approximately 1588 and 1435 cm^{-1} can be attributed to the symmetric and asymmetric -COO stretching vibration modes, respectively, indicating covalent bonding between the -COO- groups of the OA and the Fe atom of the NPs [26], [66], [104].

The FTIR spectrum of DMSA coated SPIONs reveals characteristic bands related to carboxylic acid functional groups. The DMSA presence on the SPIONs' surface is supported by the identification of bands associated with the asymmetric and symmetric stretching vibration modes of the C=O double bond at approximately 1587 cm^{-1} and 1373 cm^{-1}, respectively. The IR bands characteristic of thiol (S-H) or disulfide groups (S-S) at the ranges 2250–2600 cm^{-1} and 500–540 cm^{-1}, respectively are not evident in the DMSA spectrum. According to the literature, the absence of S-H stretching vibration modes can be attributed to the dialysis process which in turn contributes to the formation of intraparticle S-S bridges [105], [106]. However, the S-S band may be concealed by the Fe-O band due to overlapping ranges, leading to the apparent absence of the thiol and disulfide groups in the FTIR spectrum.

According to the literature, the primary mechanism behind the covalent anchoring of the aminopropyl silane groups is predominantly attributed to their self-polycondensation and this should be observed in a band at approximately 584 cm^{-1} [107]. However, the spectrum does not exhibit the

presence of Fe-O-Si bonds, as these bonds overlap with the Fe-O vibrations of the SPIONs, similar to what is observed in the curve of the DMSA-coated SPIONs. Nevertheless, two characteristic bands of this type of coating can be observed: one around 1555 cm^{-1}, corresponding to the bending mode of the amine, and another absorption band at 959 cm^{-1}, attributed to the stretching vibration of Si-O.

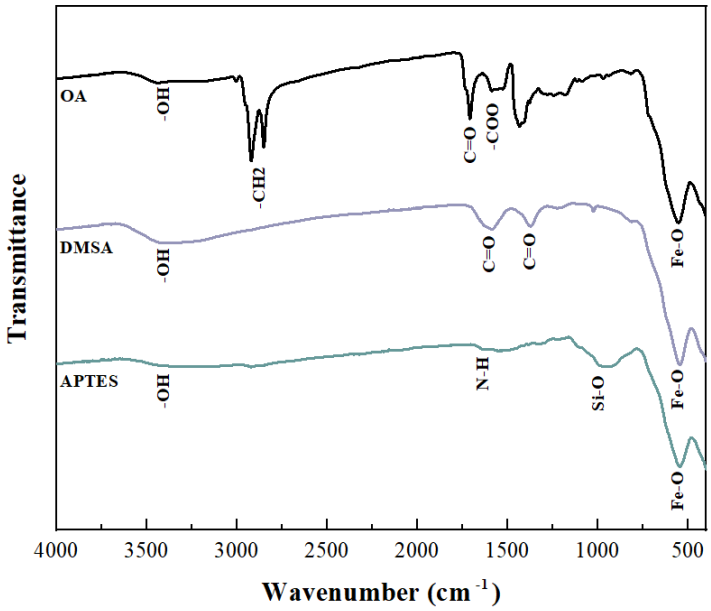

Figure 4.1 | **FTIR spectra of SPIONs synthesized by chemical co-precipitation.** SPIONs coated with OA (black line), DMSA (purple line) and APTES (green line).

4.1.2 TGA

The thermal stability of the three different coated SPIONs under study was assessed by TGA and the obtained curves are shown in Figure 4.2.

The TGA curve of OA-coated SPIONs exhibits four distinct mass losses. Up to 300 °C, there is a weight loss of 19.08%, likely attributed to both the desorption of water molecules and the removal of the free/weakly bound coating agent since this range includes the boiling temperature of OA (b.p. 94-195 °C/1.2 mmHg) [108]. The next two weight losses in the ranges of approximately 300-400 °C and 400-500 °C were 15.85% and 5.10%, respectively, which may be associated with the chemisorption decomposition of OA on the surface of the NPs. This confirms a higher binding energy between the OA molecules and the SPIONs and occurs when a bilayer is formed. Finally, in the range of 500-890 °C, a weight loss of 11.07% is observed, likely resulting from the weight loss of the SPIONs themselves. This is caused by the reducing gas produced from the coating agent at elevated temperatures, and beyond 600 °C, the carbon of the OA is oxidized, forming CO and CO_2 [109]. The considerable difference concerning the weight loss observed in OA-coated SPIONs compared to DMSA- and APTES-coated NPs can be attributed to the fact that the OA-coated SPIONs, being an oil-based sample, did not undergo proper lyophilization. This was evident through visual inspection, as the DMSA and APTES samples appeared in powder form, while the OA-coated samples did not.

Regarding the plot of DMSA functionalized SPIONs, this is characterized by two mass losses: one at ~200 °C of about 5.14% and another one at ~600 °C of 3.40% that can be justified due to loss of water and due to the decomposition of DMSA ligands over the SPION surface, respectively. According to the literature the loss of these ligands is usually more defined with 3 steps between 140 and 500 °C [110].

Lastly, the TGA curve of APTES-coated SPIONs shows a weight loss of approximately 1.32% until approximately 200 °C, which is likely attributable to the presence of water and impurity phases, probably from unwashed salts. Beyond this temperature, as indicated in the literature, the APTES coating decomposes, resulting in an additional weight loss of 4.98% [111].

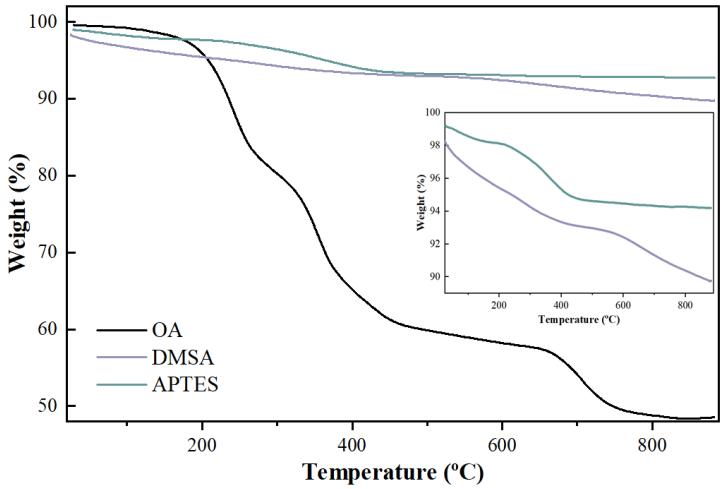

Figure 4.2 | **TGA curves of SPIONs produced by chemical co-precipitation.** SPIONs coated with OA (black line), DMSA (purple line) and APTES (green line).

4.1.3 XRD

XRD is a valuable method for exploring the crystal structure and phases of materials, enabling confirmation of their composition and identification of specific crystalline phases. In the case of SPIONs, magnetite (Fe_3O_4) and maghemite (γ-Fe_2O_3) are the principal phases, however, their similar crystal structures and physical properties pose challenges in precisely distinguishing them through this technique [112].

Magnetite is generally preferred for biomedical applications, especially MH, due to its higher magnetization and consequently greater heating efficiency. The SPIONs synthesis process was carried out under anaerobic conditions facilitated by the presence of N_2, so the resulting SPIONs should possess a cubic crystalline structure, mainly consisting of magnetite.

Figure 4.3 shows the XRD patterns obtained from the synthesized SPIONs coated with OA, DMSA and APTES. The three patterns exhibit the presence of six distinctive 2θ peaks associated with these NPs, positioned at 30.3, 35.6, 43.3, 53.6, 57.2, and 63.1, corresponding to the diffraction planes (220), (311), (400), (422), (511), and (440), respectively [66]. A comparison with standard XRD patterns for magnetite and maghemite powders (JCPDS 00-019-0629 for magnetite and JCPDS 00-039-1346 for maghemite) confirms that the produced SPIONs possess a cubic crystalline structure characteristic of

magnetite. This confirmation underscores the preservation of the crystalline structure of the SPIONs across all the utilized coating agents post-stabilization.

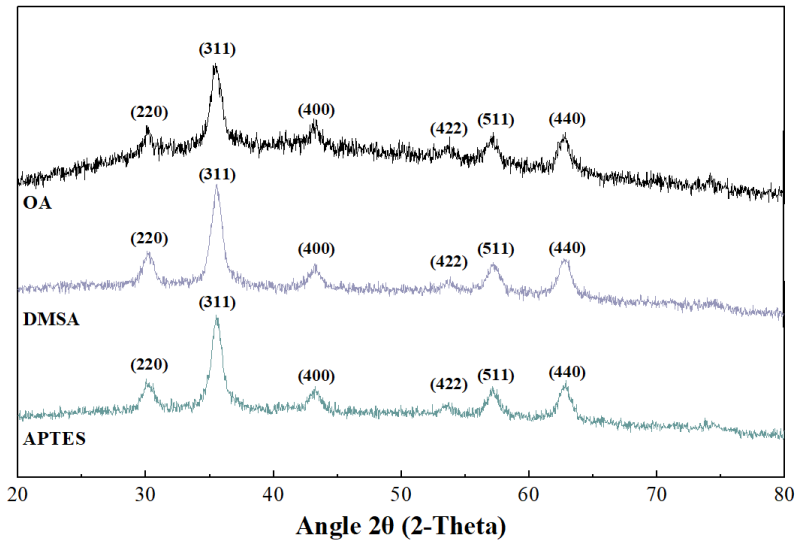

Figure 4.3 | **X-ray pattern of SPIONs synthesized by chemical co-precipitation.** SPIONs coated with OA (black line), DMSA (purple line) and APTES (green line).

To analyze the crystallinity of the different SPIONs quantitatively, their average crystallite size was calculated using Scherrer's equation (4.2):

$$\tau = \frac{K\lambda}{\beta \cos\theta} \tag{4.2}$$

Where τ represents the average core diameter of the particles; K is the Scherrer's constant or grain shape factor (K = 0.94); λ stands for the incident X-ray wavelength (λ= 1.54 Å); β denotes the full width at half-maximum (FWHM, in radians) of the highest intensity, and θ is the Bragg diffraction angle (angle of diffraction). Based on this equation, the OA-coated SPIONs exhibited an average crystallite size of approximately 7.9 nm (2 θ = 35.46), for DMSA-coated SPIONs approximately 6.8 nm (2 θ = 35.56), and for APTES-coated SPIONs, the τ value was approximately 7.5 nm (2 θ = 35.50). Upon comparing the obtained values with the existing literature, it can be inferred that the synthesized SPIONs retained the crystal structure of the uncoated SPIONs. This observation indicates that the stabilizers used in the synthesis process do not introduce any alterations to the crystal structure of the SPIONs as reported elsewhere [66].

4.1.4 TEM

In order to study the size and its distribution, as well as to observe the morphology of the synthesized SPIONs, TEM technique was used. Figure 4.4 displays the TEM analysis of OA (A and D), DMSA (B and E), and APTES (C and F) coated NPs. The average sizes, within a distribution range of 3-11 nm, were approximately 7.1 ± 1.4 nm, 6.6 ± 1.1 nm, and 6.6 ± 1.2 nm, respectively. This is interesting considering that, all three types of SPIONs fulfilled the criteria for biomedical applications, as they had sizes below 200 nm with a narrow size distribution, and their sizes remained within the range suitable

for superparamagnetism, which should not exceed a few tens of nanometers. A semi-spherical shape was observed in all TEM images, which, according to the literature, can be attributed to the type of salts used for NP production or the molar ratio of the iron ions [113]. Furthermore, it can also be concluded that the presence of the different coatings had no influence on the core size of the SPIONs, keeping the particles diameter between 6 - 8 nm, which is in agreement with the average crystallite size obtained from the XRD analysis.

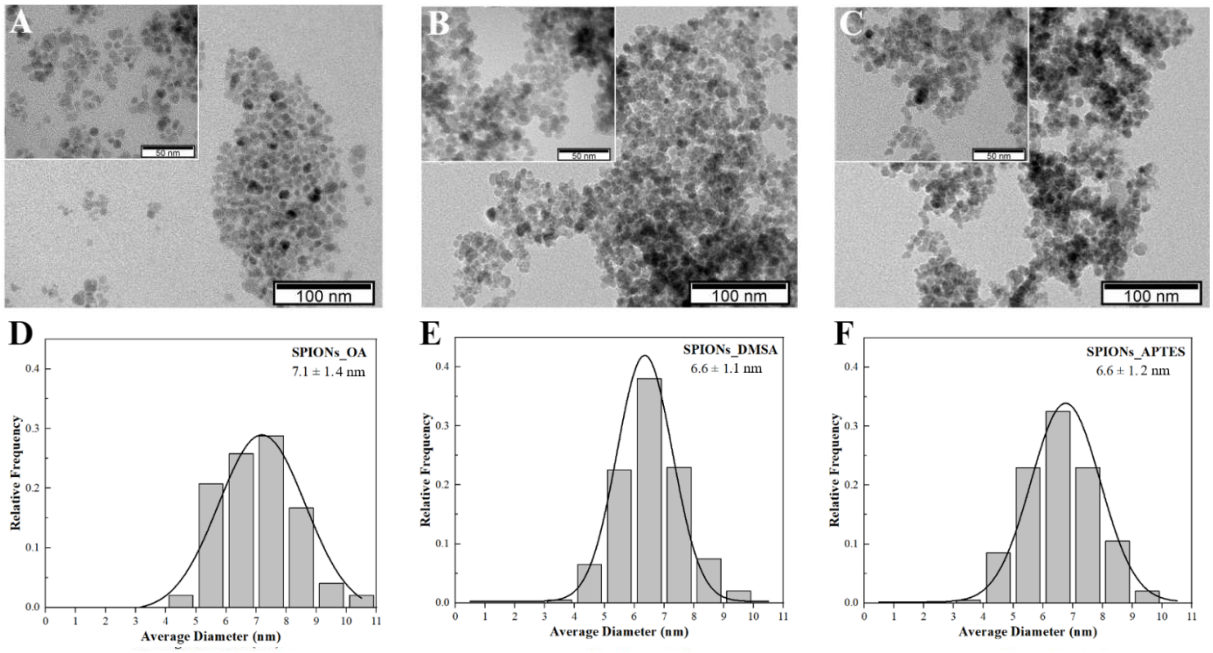

Figure 4.4 | **TEM images and the corresponding size distribution graphs of SPIONs synthesized by chemical co-precipitation.** OA-coated SPIONs (A, D), DMSA-coated SPIONs (B, E) and APTES-coated SPIONs (C, F). Scale bar of 50 nm and of 100 nm.

4.1.5 ζ-Potential and DLS Analysis

The Dh is a critical parameter in particle characterization as it reflects the particle size when in solution, considering any coatings or modifications on the particle surface [114]. In this regard, the evaluation of the hydrodynamic size in water for the various synthesized SPIONs was carried out in three different concentrations (0.025, 0.05, and 0.1 mg/mL) and the results are presented in Figure 4.5 (A). As shown, at the highest concentration (0.1 mg/mL), significant aggregate formation was observed in all three types of NPs, rendering this concentration unsuitable for further measurements. Regarding the concentration of 0.025 mg/mL the sizes of this first synthesis were approximately 93, 201 and 90 nm for the SPIONs coated by OA, DMSA and APTES respectively, while for the same order of coatings for the concentration of 0.05 mg/mL were approximately 90, 191 and 86 nm respectively. Although the differences were not substantial, the sizes obtained for the intermediate concentration (0.05 mg/mL) were slightly smaller, leading to its selection for the subsequent measurements throughout the study.

ζ-potential is a parameter that quantifies the electrostatic charge present on the surface of colloidal particles, such as NPs, dispersed in a liquid medium and serves to quantify the potential difference between the particle surface and the surrounding liquid. Due to its significant role in determining the

stability and behavior of colloidal systems, ζ-potential was also evaluated in this study and the results are shown in Figure 4.5 (B). In this first characterization, this parameter was also conducted in filtered MiliQ water, at a concentration of 0.05 mg/mL, and the results presented confirmed the expected contrast between coating agents [115], [116]. SPIONs coated with OA and DMSA exhibited negative charges of -63.7 ± 1.5 mV and -46.3 ± 7.8 mV, respectively, while the APTES-coated SPIONs displayed a positive charge of approximately +30.5 ± 5.8 mV.

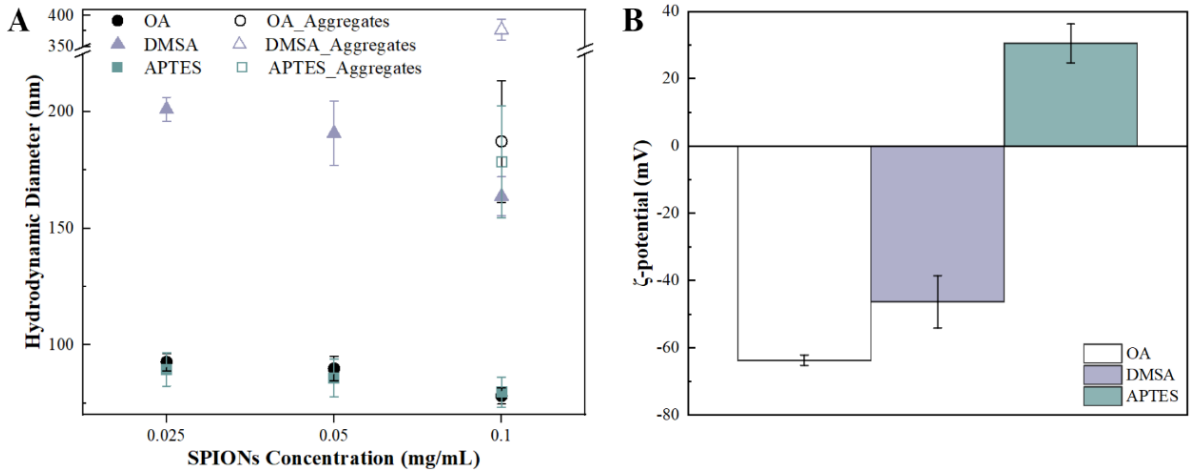

Figure 4.5 | **Hydrodynamic diameter (A) and ζ-potential analysis (B) of SPIONs produced by chemical co-precipitation diluted in water.** SPIONs coated with OA (black), DMSA (purple) and APTES (green). Data is expressed as average ± standard deviation for at least five measurements.

Different syntheses were carried out throughout this study and Table A.1 in Appendix A2 gives an overview of the various Dh and ζ -potentials obtained. From these data, it was possible to observe some variation between the syntheses, which can be attributed to many factors. Some of the factors that may have affected the disparity in results could be associated with the reaction conditions (reaction time, temperature, pH and stirring), the concentration of precursors and coating agents (which may have been subject to measurement errors) and variations in the dialysis process (for OA and DMSA coated SPIONs) [117], [118]. Therefore, a comprehensive understanding and control of these factors are crucial for achieving better homogeneity of results across syntheses.

4.1.6 Magnetic Hyperthermia Analysis

An important parameter in MH is the SAR of the material, which characterizes the material's capability to convert alternating magnetic energy into heat [119]. To evaluate the heat-producing capacity of the produced SPIONs, diverse samples were subjected to a magnetic field strength of 300 Gauss and a frequency of 388.4 kHz. A temperature stabilization interval of approximately 30-40 seconds with no applied field was followed by a 10-minute application of the field. Four distinct concentrations (1, 2.5, 5, and 10 mg/mL) were tested in water, with the outcomes depicted in Figure 4.6. The SAR values shown (Figure 4.6 (B)) were calculated according to equation A.6 presented in Appendix A2.

The results illustrated variations between different stabilizers, with OA-coated SPIONs registering the highest values for both ΔT and SAR, while APTES-coated NPs exhibited the lowest values. For

a concentration of 5 mg/mL, the recorded ΔT values (in °C) were 30.2 ± 1.7, 24.2 ± 0.8, and 19.5 ± 0.6 for OA-coated SPIONs, DMSA-coated NPs, and APTES-coated NPs, respectively. Correspondingly, for the same sequence of coatings and concentration, the SAR values attained (in W/g) were 190 ± 5, 149 ± 11, and 119 ± 11. The chosen concentration for these parameter measurements in subsequent tests was 5 mg/mL.

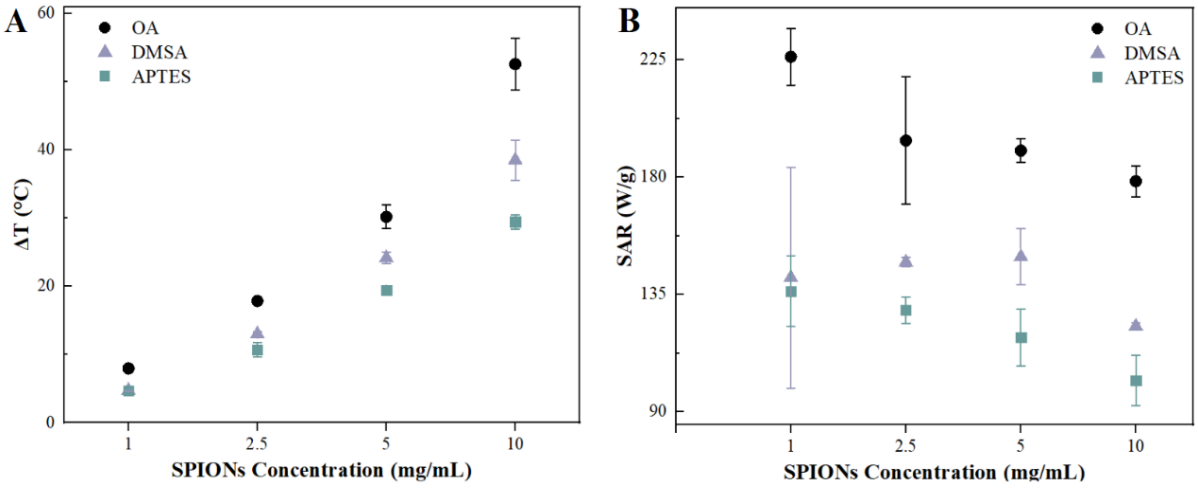

Figure 4.6 | **Temperature variation (A) and SAR values (B) of SPIONs produced by chemical co-precipitation in water for different concentrations.** SPIONs coated with OA (black), DMSA (purple) and APTES (green). Temperature variation induced by the application of an AMF with a 300 G intensity and a 388.4 kHz frequency, over a period of 10 minutes.

4.2 SPIONs Stability

4.2.1 ζ - Potential

Due to its significant role in determining the stability and behavior of colloidal systems, the ζ - potential of the different SPIONs was evaluated using different media [120]. As already mentioned, in a first characterization, this parameter was measured in filtered MiliQ water and the SPIONs coated with OA, DMSA and APTES exhibited (in mV) surface charges of -63.7 ± 1.5, -46.3 ± 7.8, and +30.5 ± 5.8. However, in physiological environment, large quantities of proteins adsorb to the NPs, leading to alterations in their surface charge. Thus, the ζ - potential was also analyzed both in PBS 1x and in the different cell media used (DMEM HG + 5% FBS, DMEM LG + 10% FBS and complete RPMI).

As depicted in the Figure 4.7, the ζ -potential values were closer to zero in PBS, and this effect became more pronounced when the NPs were exposed to the different cell media due to the surface charge neutralization effect by the surrounding proteins. This observation underlines the significant influence of the surrounding environment on the ζ-potential of NPs and highlights the need for a comprehensive understanding of colloidal behavior under biological conditions as it directly influences the fate and biological responses of NPs *in vivo.*

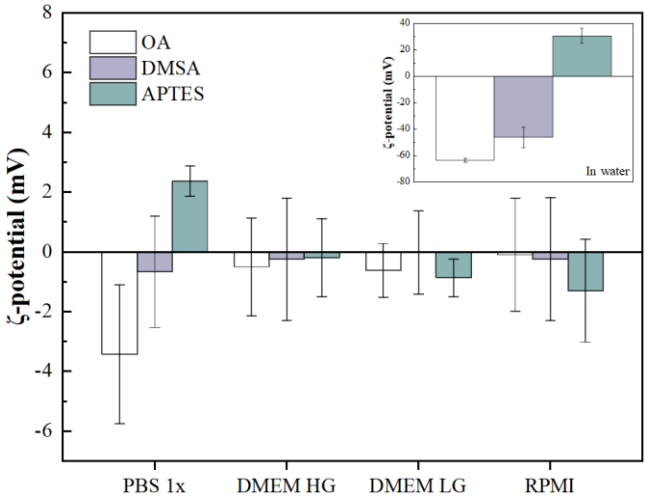

Figure 4.7 | **ζ-potential analysis of SPIONs at 5 mg/mL in water, PBS 1x and cell culture media.** SPIONs coated with OA (black), DMSA (purple) and APTES (green). Data is expressed as average ± standard deviation for at least three measurements.

4.2.2 Protein Corona Formation

When in contact with biological fluids, a dynamic layer of proteins tend to adsorb onto the surface of the NPs. This resultant structure, known as the PC, comprises proteins constituting the "hard corona", those demonstrating affinity for either the iron oxide core or the polymer coating, and proteins that exhibit weaker binding forming the "soft corona" through protein-protein interactions [62], [121]. The formation of the PC ends up giving the functionalized NPs a new identity, altering their physicochemical properties and affecting their stability and interaction with cells [64].

In order to gain a deeper insight into PC formation in the synthesized SPIONs, the Dh of the various SPIONs was measured using the DLS technique. PC formation was tested with MiliQ water as a control and also with the 3 types of cell culture media related to the cell lines under study, with and without FBS, in order to also assess the influence of serum on the Dh of the SPIONs. Four-time intervals (1 h, 6 h, 12 h, and 24 h) were also investigated to discern the impact of time. The results for SPIONs coated with OA, DMSA and APTES are shown in Figure 4.8, Figure 4.9 and Figure 4.10, respectively.

The results show that protein adsorption occurs rapidly, resulting in minimal variation over the time periods studied. According to the literature, the formation of PC in DMEM is contingent on time and does not occur instantly [63], [122]. However, it's important to mention that these observations were not corroborated in this particular work. Moreover, OA-coated (Figure 4.8) and DMSA-coated (Figure 4.9) SPIONs exhibited similar behavior, probably due to their negative charges attracting similar positively charged components of the surrounding medium. In addition, serum-free media led to the formation of larger hydrodynamic sizes in the case of SPIONs coated with negatively charged coating agents. Figure 4.8 (B, C) and Figure 4.9 (B, C) show curves below the water curve (shown in Figure 4.8 (A) and Figure 4.9 (A)). This could possibly be due to measurements of negatively charged components in these media (DMEMLG_FBS and RPMI_FBS). These values are lower than those for SPIONs suspended in water, indicating that they correspond to smaller components than the SPIONs themselves. Regarding APTES-coated SPIONs (Figure 4.10), the curves indicate the largest hydrodynamic sizes,

suggesting FBS contains abundant negatively charged proteins. This aligns with previous literature which suggest that NPs with an initially positive surface charge tend to form larger PCs after medium incubation compared to NPs with an negative surface charge [64], [123].

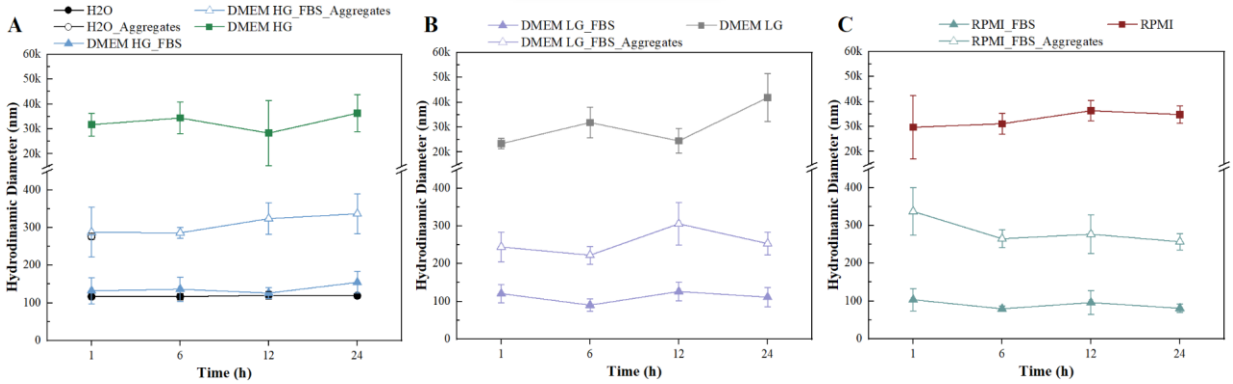

Figure 4.8 | **Analysis of the dynamics of PC formation in OA-coated SPIONs incubated for periods of 1 h, 6 h, 12 h and 24 h at 0.05 mg/mL in different media.** Water and DMEM_HG with and without FBS (A), DMEM_LG with and without FBS (B) RPMI with and without FBS (C). Hydrodynamic diameter variation vs time. Data is expressed as average ± standard deviation for at least three measurements.

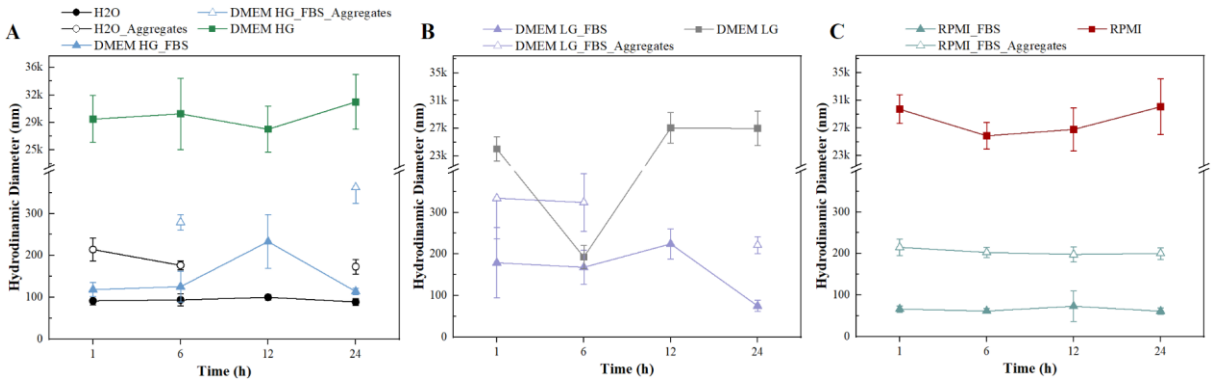

Figure 4.9 | **Analysis of the dynamics of PC formation in DMSA-coated SPIONs incubated for periods of 1 h, 6 h, 12 h and 24 h at 0.05 mg/mL in different media.** Water and DMEM_HG with and without FBS (A), DMEM_LG with and without FBS (B) RPMI with and without FBS (C). Hydrodynamic diameter variation vs time. Data is expressed as average ± standard deviation for at least three measurements.

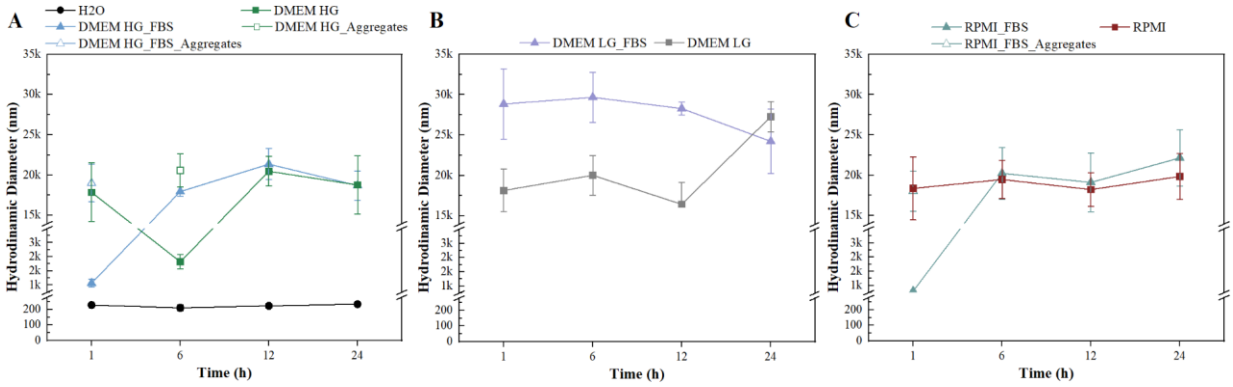

Figure 4.10 | **Analysis of the dynamics of PC formation in APTES-coated SPIONs incubated for periods of 1 h, 6 h, 12 h and 24 h at 0.05 mg/mL in different media.** Water and DMEM_HG with and without FBS (A), DMEM_LG with and without FBS (B) RPMI with and without FBS (C). Hydrodynamic diameter variation vs time. Data is expressed as average ± standard deviation for at least three measurements.

Calatayud *et al.* conducted a study that also revealed significant differences in the hydrodynamic size of NPs with distinct surface charges after a 24-hour incubation in a protein-rich cell medium [64]. After this time, the group observed that NPs with a positive surface charge exhibited a hydrodynamic size of approximately 3000 nm, while NPs with a negative surface charge measured approximately 1500 nm. In a study by Portilla, Y. *et al.*, the group evaluated PC formation using SPIONs coated with APTES and DMSA, using DMEM for incubation with different time points [63]. They observed that the maximum hydrodynamic size occurred after an incubation of 5 to 10 h (2455 nm for APTES-MNPs and 209 nm for DMSA-MNPs) and then decreased until stabilizing after 24 h. While the sizes differed significantly from our study, the research group also noted a similar increase in the Dh of APTES-coated SPIONs, consistent with our findings.

In conclusion, the variations in hydrodynamic size observed in MNPs coated with different coatings following media incubation are directly attributed to the surface charges introduced by each respective coating. To isolate SPIONs with adsorbed proteins, future investigations could involve resuspending SPIONs in water before measurements to exclude medium constituents' influence and facilitate subsequent comparisons.

4.2.3 Magnetic Hyperthermia

To evaluate the stability and capacity of the produced SPIONs to maintain their characteristics over time, ΔT and SAR values were gauged at 1, 3, and 6 months post-synthesis. Prepared at a concentration of 5 mg/mL in water, the samples underwent identical field conditions as employed during their initial characterization. The outcomes are depicted in Figure 4.11. The SAR values shown were calculated according to equation A.2 in Appendix A2.

From the results obtained, it can be seen that, in general, there are significant differences at the end of the 3-month period, with a decrease in these parameters in the three types of SPIONs synthesized. Notably, SPIONs coated with APTES displayed the least significant decrease. The elevated values (in some cases) observed after 6 months could potentially be attributed to challenges in maintaining an exact SPIONs concentration due to increased aggregation and heightened resistance to dispersion via

sonication. In the future, it would be interesting to evaluate the hydrodynamic size over these periods of time to confirm the suggested formation of aggregates. Kulikov *et al.* observed a (smaller) decrease in SAR values after 18 months in OA-coated SPIONs, attributing it to alterations in magnetic properties resulting from potential oxidation of Fe^{2+} ions in the Fe_3O_4 structure, consequently impacting the NPs' surface anisotropy [124].

Ultimately, underscoring the significance of periodically monitoring physicochemical attributes of standard NPs, including size/agglomeration, surface charge, and, as illustrated in this context, heat capacity, throughout the study duration is crucial. Such monitoring allows that any changes are duly considered when interpreting and analyzing the collected data.

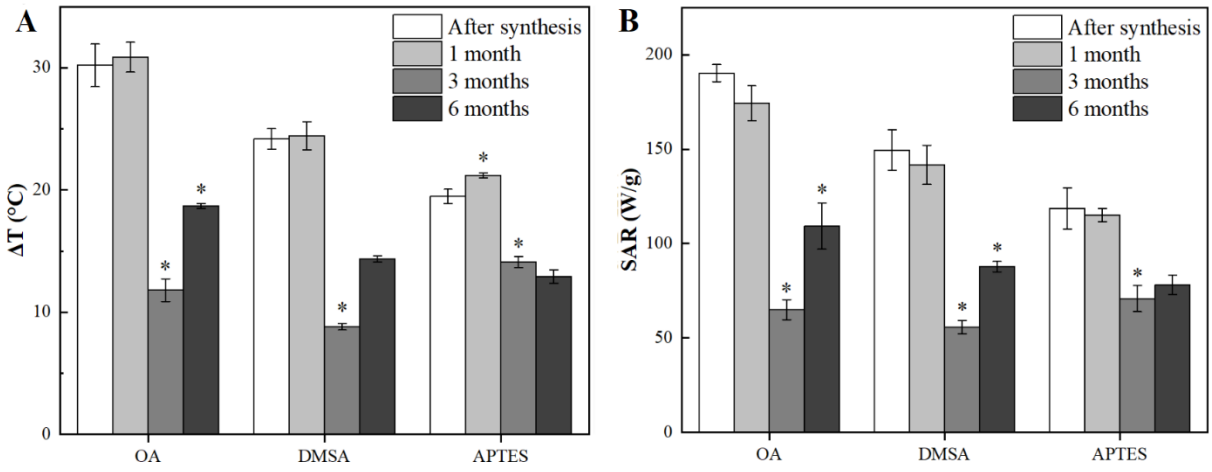

Figure 4.11 | **Evaluation of SPIONs stability at 5 mg/mL in water through analysis of temperature variation (A) and SAR values (B) over 6 months.** Temperature variation induced by the application of an AMF with a 300 G intensity and a 388.4 kHz frequency, over a period of 10 minutes. Data is expressed as average ± standard deviation for at least three measurements. *p value < 0.05 compared with the previous measurement.

The heating capacity of the produced SPIONs at the end of 1 month period, using various solvents, was also evaluated. Once again, the samples were prepared at a concentration of 5 mg/mL, but this time in water, in a PBS solution, and in DMEM HG. The results are depicted in Figure 4.12.

Regarding using water, a reduction in ΔT and SAR values could be observed, however, this reduction was only significant when PBS and DMEM HG were utilized as dispersion media. This phenomenon can be attributed to the formation of a PC, which enhances the propensity for aggregate formation. The principal difference when comparing water and the other two dispersion media was observed for the OA-coated SPIONs, probably due to their high negative surface charge which led to greater bonding with the cations present in the surrounding media, culminating in greater aggregation and loss of stability.

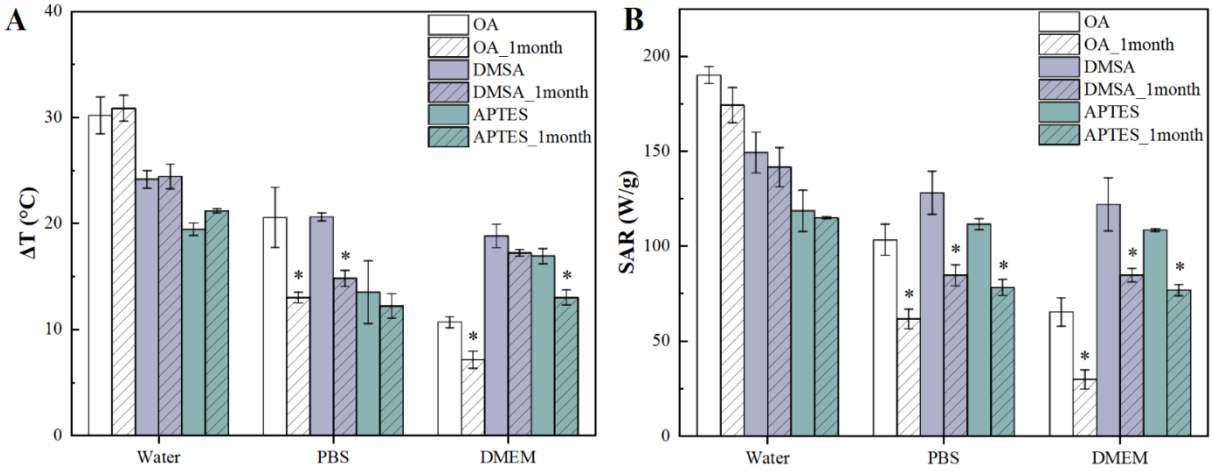

Figure 4.12 | **Evaluation of SPIONs stability at 5 mg/mL in water, PBS 1x and DMEM HG + 10% FBS through analysis of temperature variation (A) and SAR values (B) at the end of the 1-month period.** SPIONs coated with OA (white), DMSA (purple) and APTES (green). Temperature variation induced by the application of an AMF with a 300 G intensity and a 388.4 kHz frequency, over a period of 10 minutes. Data is expressed as average ± standard deviation for at least three measurements. *p value < 0.05 compared with the previous measurement.

4.3 SPIONs Cytotoxicity

Since SPIONs hold great promise as candidates for MH applications, which involve direct contact with the human body, their biocompatibility is of utmost importance. Thus, in order to evaluate the possible cytotoxicity of the synthesized SPIONs, the resazurin colorimetric method was performed, and the results are depicted in Figure 4.13.

The assay was conducted on three different cell lines: HFFF2 presented in Figure 4.13 (A), WM983b in Figure 4.13 (B), and THP-1 shown in Figure 4.13 (C). Cells were exposed to different concentrations of NPs for 24 h and 48 h, and the results are expressed as the percentage of cell viability relative to the control (cells not exposed to NPs but maintained under the same conditions). SPIONs concentrations that resulted in cell viability of more than 80% were considered to be non-cytotoxic. The detailed protocol can be found in Appendix B1.

Regarding OA-coated SPIONs, it is possible to observe that they are not toxic at the lowest concentrations tested; however, cytotoxicity can be observed from 0.5 mg/mL onwards, primarily for HFFF2 cells. In contrast, DMSA-coated SPIONs demonstrated the lowest cytotoxicity to the cell lines used, presenting a viability above 80% except WM983b in the presence of the highest NPs concentration. On the other hand, SPIONs coated with APTES exhibited moderate cytotoxicity in fibroblast and macrophage cell lines, and in the HFFF2 cell line, the behavior did not appear to be dose-dependent, remaining relatively constant as the concentration of NPs increased.

A Live/Dead assay was performed (results presented in Figure 4.14), also revealing that there appears to be no direct correlation between cell viability and the NPs concentration used. Having said that, it can be inferred that these specific SPIONs exhibit a certain level of cytotoxicity, that appears to be non-concentration dependent. This observation is further supported by the fact that in all assays, the percentage of cell viability remains above 50%. It is important to note that the results of cytotoxicity assays are highly influenced by several factors, these factors encompass the cell lines chosen, the

specific nature of the assay performed and critical aspects such as the size, composition, morphology, and concentration of the NPs under study. Moreover, the pH of the culture medium and the duration of exposure are additional key factors that significantly influence the cytotoxicity responses.

According to available literature, positively charged NPs tend to be more cytotoxic to non-phagocytic cells, while anionic ones are more cytotoxic to phagocytic cells [64], [125]. However, such conclusions couldn't be drawn from the results obtained in this study. Furthermore, the assay was also performed after 48 h of cell exposure to the synthesized SPIONs, but as can be seen in Figure B.2 in Appendix B, no significant differences were observed after this period. As a result, all remaining assays were conducted only with a 24 h exposure period.

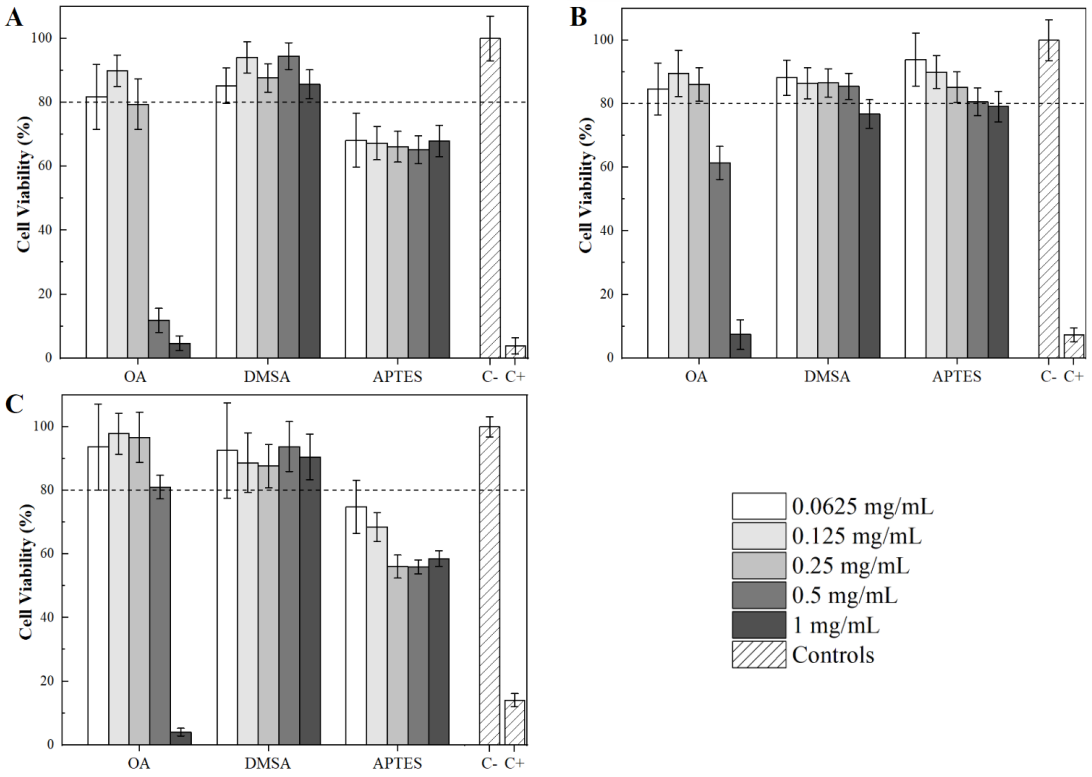

Figure 4.13 | **Resazurin cell viability assay of the HFFF2 (A), WM983b (B) and THP-1 (C) cell lines after 24 h of incubation with the three types of SPIONs produced.** Data is expressed as mean ± uncertainty for three independent experiments with five replicates for each condition.

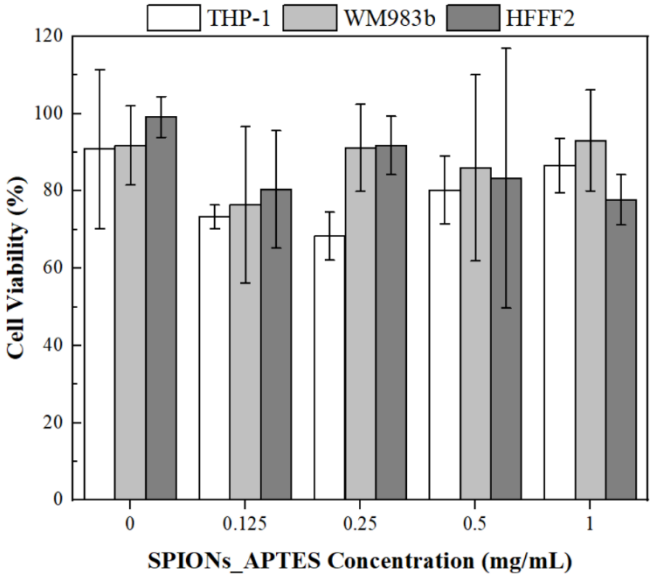

Figure 4.14 | **Live/Dead cell viability assay of the HFFF2, WM983b and THP-1 cell lines after 24 h incubation with APTES-coated SPIONs.** Three replicates were made for each concentration and data is expressed as average ± uncertainty for approximately 15 images for each condition.

4.4 SPIONs Internalization

To study the interaction between the SPIONs under study and the three cell lines, images of the location of the NPs inside the cells were taken with Prussian blue staining after 1 h, 6 h and 24 h of exposure time. Figure 4.15, Figure 4.16 and Figure 4.17 depict the contact of the different types of SPIONs at a concentration of 100 µg/mL with HFFF2, WM983b, and THP-1 cell lines, respectively.

The increasing predominance of the blue color with longer exposure times indicates a higher number of SPIONs bound to the cell membranes or already internalized within the cells. When comparing the three types of coatings, APTES-coated SPIONs show a higher intracellular uptake compared to the other two NP types. This finding aligns with existing literature, which suggests that NPs with a positive surface charge are more efficiently internalized due to the physical adhesion (electrostatic attraction) between the NPs and the negatively charged cytoplasmic membrane [126]. This electrostatic attraction is generally considered as a primary driving force in regulating the cellular uptake of NPs [127]. In the study conducted by Calatayud *et al.*, aforementioned in section 4.2.2, besides investigating the impact of surface charge on hydrodynamic size when exposed to physiological media, they also explored the influence of this charge on NP internalization in neuroblastoma cells [64]. In this study, the research group observed that the cells were able to incorporate 100% of the initially positively charged NPs (added up to ≈100 pg/cell), while for the initially negatively charged NPs, absorption was less than 50%.

Moreover, a relatively higher internalization of DMSA-coated SPIONs compared to OA-coated ones is also observed. This observation can be attributed not only to the charge, as it is less negative compared to OA, but also its smaller hydrodynamic size making it more easily absorbed by cells.
Finally, an enhanced internalization of the different types of SPIONs by macrophages can be observed, especially within the first hour of exposure. The mechanism of cellular uptake remains unclear, but there

are already some types of SPIONs under study evaluated as NMR markers for the diagnosis of inflammatory and degenerative diseases associated with high phagocytic activity of macrophages [47], [128]. Furthermore, a noticeable difference in internalization can be observed between the HFFF2 and WM983b cell lines, with fibroblasts exhibiting a higher internalization rate compared to the melanoma cell line. This finding is particularly noteworthy, as recent studies indicate that extracellular MH results in elevated levels of cell apoptosis due to the higher heating efficiency of SPIONs. For example, Hannon G. *et al*. observed significant differences in cell viability within a pancreatic cancer cell line when comparing intracellular and extracellular MH. Following a 30-minute exposure, they observed that extracellular MH led to significant levels of cell necrosis, while intracellular MH had no impact on cell viability [48]. Another study, coordinated by Simões B. *et al.*, explored the internalization dynamics of SPIONs in WM983b using molecular inhibitors of endocytosis [132]. This work revealed that the SAR values were higher when SPIONs were in the extracellular environment, and consequently inhibiting the cellular uptake of SPIONs enhances the efficacy of MH.

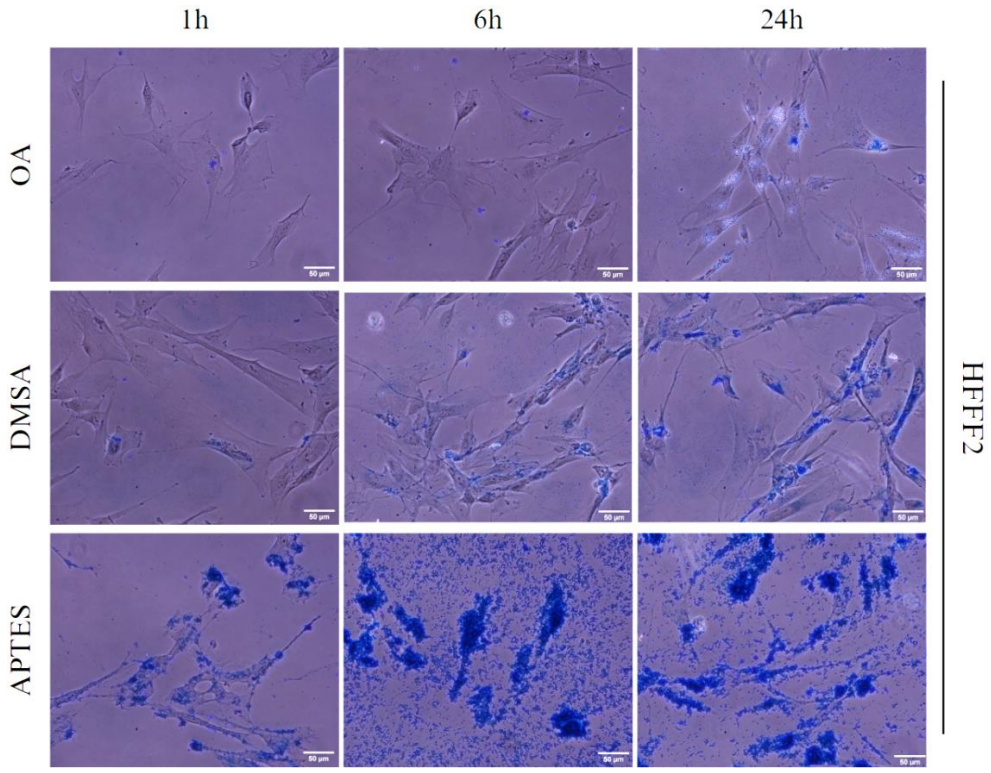

Figure 4.15 | **SPIONs intracellular location in HFFF2 fibroblast cells after Prussian blue staining.** Cells incubated with 100 µg/mL of SPIONs coated with OA, DMSA and APTES for 1 h, 6 h and 24 h. Bright field images at 40x objective magnification with scale bar: 50 µm.

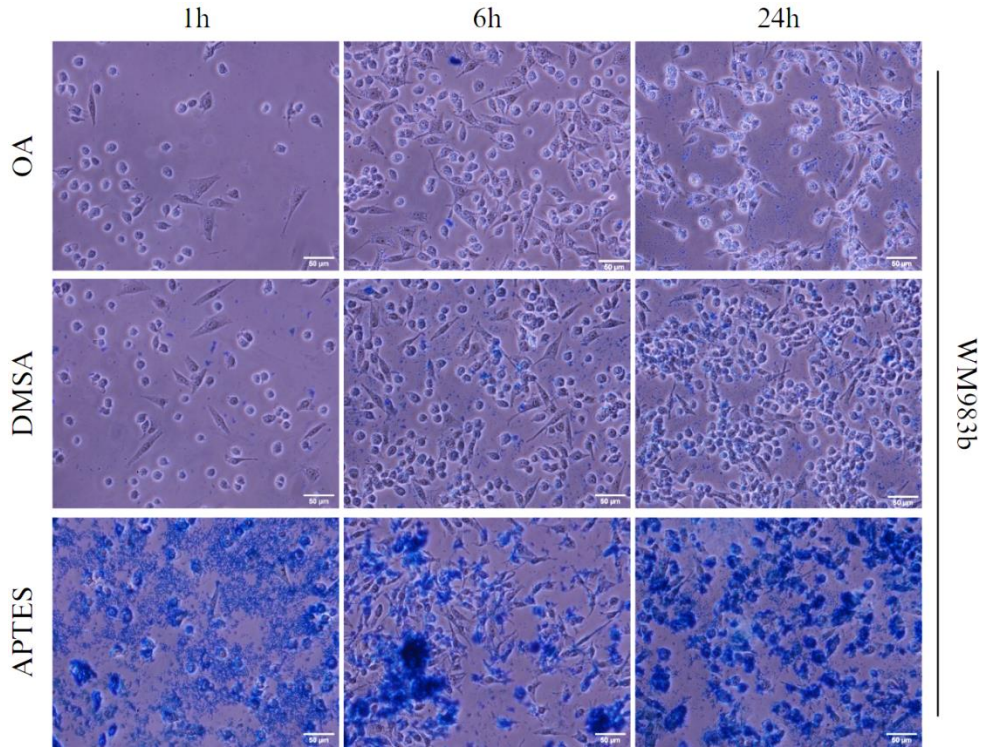

Figure 4.16 | **SPIONs intracellular location in WM983b melanoma cells after Prussian blue staining.** Cells incubated with 100 µg/mL of SPIONs coated with OA, DMSA and APTES for 1 h, 6 h and 24 h. Bright field images at 40x objective magnification with scale bar: 50 µm.

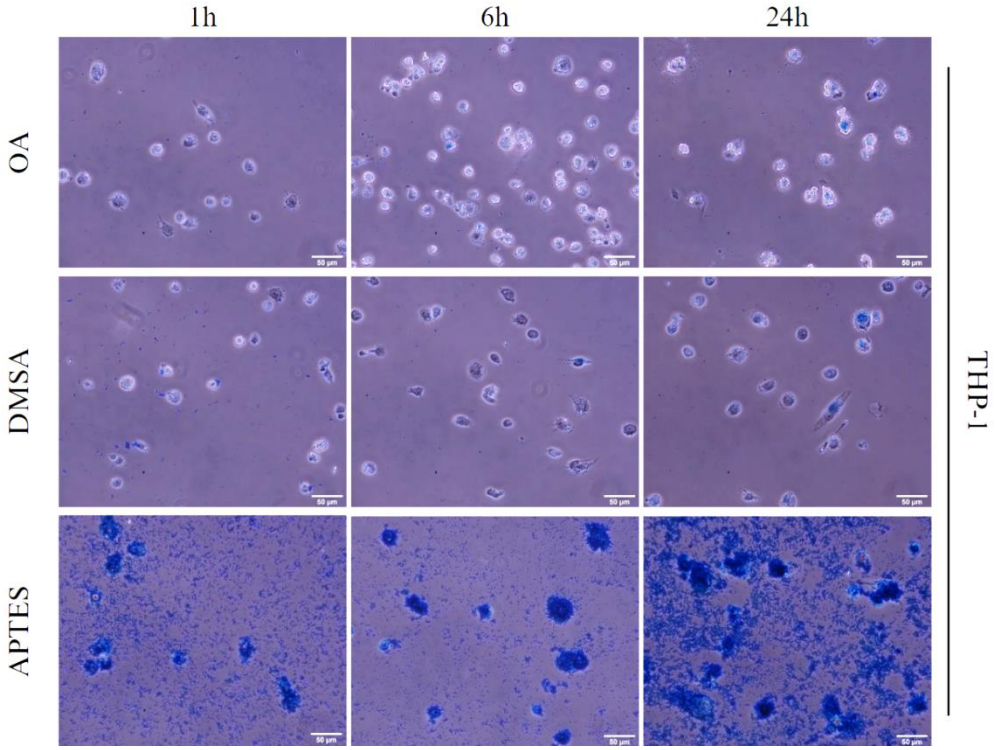

Figure 4.17 | **SPIONs intracellular location in THP-1 macrophage-like cells after Prussian blue staining.** Cells incubated with 100 µg/mL of SPIONs coated with OA, DMSA and APTES for 1 h, 6 h and 24 h. Bright field images at 40x objective magnification with scale bar: 50 µm.

4.5 Magnetic Hyperthermia

All the MH assays mentioned before were conducted in hyperthermia flasks. However, before proceeding to *in vitro* hyperthermia, heating of SPIONs in Petri dishes was tested in order to provide a better environment for cell adhesion and facilitate subsequent assays. The heating results for the different types of SPIONs at a concentration of 5 mg/mL in Petri dishes are presented in Figure 4.18. According to the obtained results, the temperatures reached were below the desired levels, with the highest temperature recorded being 30.7 °C. Upon applying the field in 2D, the heating proved to be insufficient, not even reaching the physiological temperature. Since the planar applicator did not allow the use of the same optimized parameters used for the hyperthermia flasks, the following tests were conducted in flasks to attempt to reach the desired therapeutic temperature range for the *in vitro* MH study.

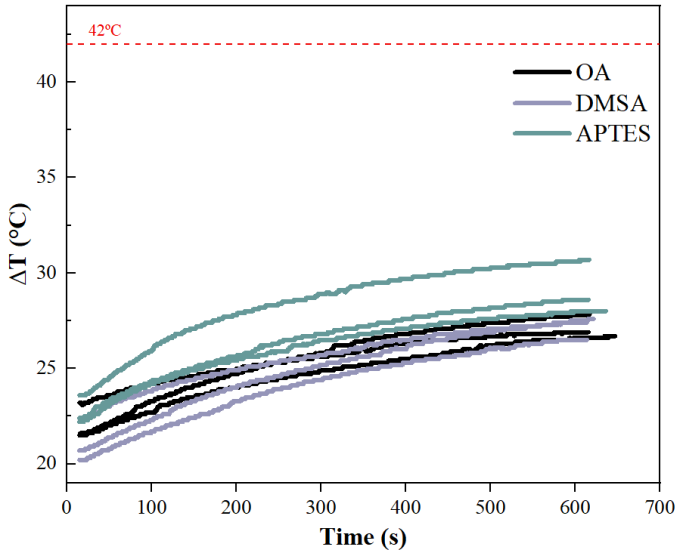

Figure 4.18 | **Temperature curves of the three types of SPIONs in water at 5 mg/mL on a planar applicator.** SPIONs coated with OA (black), DMSA (purple) and APTES (green). Temperature variation induced by the application of an AMF with a 300 G intensity and a 388.4 kHz frequency, over a period of 10 minutes. Three replicates are presented for each condition.

4.5.1 *In Vitro* Magnetic Hyperthermia

The results of the MH tests using different types of SPIONs with the HFFF2 and WM983b cell lines are shown in Figure 4.19 (A and C, respectively). For this assay, a configuration involving a 300 G AMF at a frequency of 388.4 kHz was used to achieve temperatures up to 45 °C or a maximum of 25 minutes of heating. Abrupt temperature changes in the temperature curves can be attributed to SPION sedimentation during measurement. The findings indicate that only the APTES-coated SPIONs were able to attain the desired temperatures and, in general, in the melanoma cell line, the temperature of 42 °C was reached faster compared to the assay performed in fibroblasts. For DMSA-coated SPIONs, the maximum temperatures recorded were 39.2 °C and 35.6 °C for HFFF2 and WM983b, respectively. For OA-coated SPIONs, the corresponding temperatures were 39.8 °C and 37.7 °C. The temperature contrast between the two cell lines could be possibly attributed to the elevated level of aggregation and a propensity for precipitation observed in the hyperthermia flasks containing the melanoma cell line, as

depicted in Figure B.6 in Appendix B.3. In contrast, the flasks containing the HFFF2 cell line with OA- and DMSA-coated SPIONs exhibited enhanced stability, likely contributing to their heightened heating capability.

It is well known that hyperthermia therapy induces cancer cell apoptosis by exploiting the increased sensitivity of cancer cells to temperatures between 40 °C and 44 °C. To assess the therapy's efficacy in reducing cell viability, resazurin assays were conducted immediately after MH and 24 hours later, as shown in Figure 4.17 (B and D). Overall, a substantial decline in viability compared to the control cells that remained in the incubator is evident, particularly pronounced in the WM983b cell line (D) compared to HFFF2 (B). Reduced viability in both cell and SPION controls can be attributed not only to NPs cytotoxicity at this concentration in the NPs control group but also to the suboptimal assay conditions (e.g., challenging to maintain sterility). In the case of fibroblast cells subjected to hyperthermia using OA and DMSA-coated SPIONs, a recovery in viability can be observed 24 hours post-assay.

To sum up, APTES-coated SPIONs led to a more significant reduction in viability, aligned with the higher temperatures achieved and, once again, the melanoma cell line displayed greater susceptibility, consistent with existing literature [81]. It would be interesting to re-evaluate viability 48 hours later to assess the evolving behavior of both the melanoma cell line and fibroblasts.

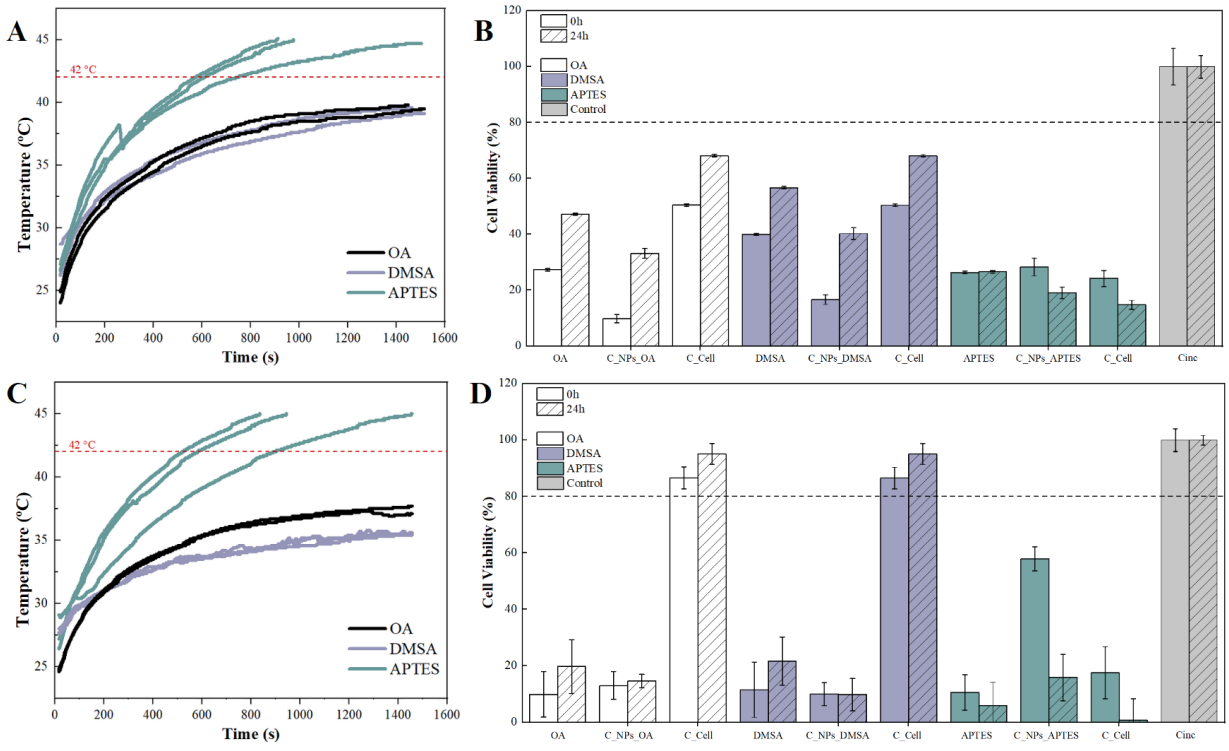

Figure 4.19 | ***In vitro* MH (A, C) and subsequent cell viability assays (B, D) of HFFF2 fibroblasts (A, B) and WM983b melanoma cells (C, D) incubated for 24 h with the different types of SPIONs.** SPIONs coated with OA (black), DMSA (purple) and APTES (green). Temperature variation induced by the application of an AMF with a 300 G intensity and a 388.4 kHz frequency, until a temperature of 45 °C or until 25 minutes of heating were reached. Two replicates are presented for OA- and DMSA-coated SPIONs and three replicates for the APTES-coated SPIONs. The cell viability test was carried out immediately after the MH test and 24 hours after. "C_NPs" denotes the NPs control (unheated vial with SPIONs and cells), "C_Cell" denotes the unheated Cell controls (without NPs) that accompanied the vials to be measured, and finally "Control" (gray bars) denotes a cell control

(without NPs) kept in the incubator. The percentage of cell viability was calculated as a percentage of the cell control (incubated) and data is expressed as mean ± uncertainty for at least five replicas for each condition.

4.6 Sand Bath Hyperthermia

Due to the challenges encountered while attempting to detach cells from the hyperthermia flasks for subsequent assays, a sand bath was employed to simulate temperature rising within the therapeutic range. In this procedure, cells from the three cell lines were individually seeded in a 24-well plate, allowed to adhere, and then exposed to 100 μg/mL of APTES-coated SPIONs. Following a 24-hour incubation period, the plate was subjected to a sand bath for 1 hour, maintaining a temperature range of 41- 44 °C.

The results of the subsequent resazurin assays, normalized to a control group not subjected to either SPIONs or temperature, are depicted in Figure 4.20. These outcomes demonstrate that the fibroblast cell line was the least affected by heating, while the melanoma cell line exhibited the most pronounced impact. It was also possible to observe that the presence of SPIONs led to a greater decrease in viability, even though it was not a MH assay. This can be justified not only by some possible cytotoxicity but also by the fact that SPIONs are good heat conductors since they are NPs composed of iron oxide.

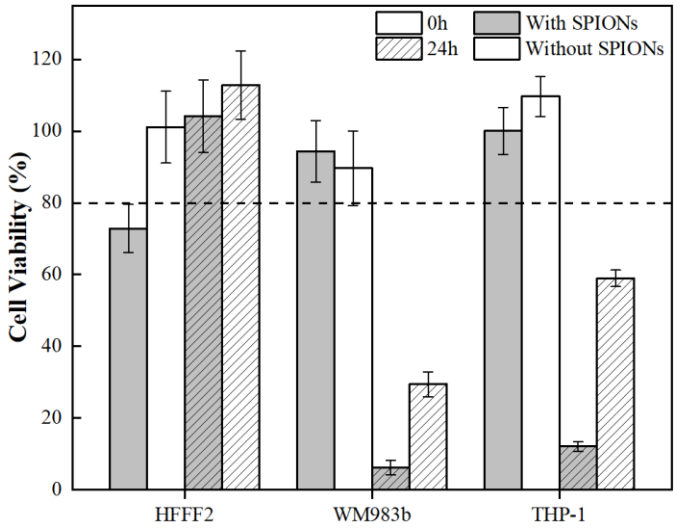

Figure 4.20 | **Cell viability of the three cell lines (HFFF2, WM983b and THP-1) after 1 hour of sand bath hyperthermia (41-44 °C).** Viability was tested right after heating and after a 24-hour incubation period. The influence of exposure to 100 μg/mL of APTES-coated SPIONs during 24 h of pre-warming incubation was also tested. The percentage of cell viability was calculated as a percentage to incubated cell controls (not exposed to either heat or SPIONs) and the data are expressed as mean ± uncertainty for at least five replicates for each condition.

As previously mentioned, the precise mechanism driving cell death resulting from hyperthermia remains a subject of ongoing research. This lack of consensus arises due to the multitude of parameters that, when altered, activate diverse cell death pathways. Existing literature indicates that numerous cell lines exhibit limited tolerance towards temperatures around 44/45 °C. This results in a range of detrimental effects, including increased apoptosis or necrosis-associated cell death. This phenomenon is observed in various cell types, such as human erythroleukemia cells, murine melanoma cells, and prostate stromal cells [133]–[136]. However, there are also some lines that have been shown to be resistant to

this treatment, such as the RIF-1 line and in osteosarcoma [137], [138]. The reason for this may be that cancer cells normally have a poor apoptosis regulation system, and for example Yonezawa *et al.*, found a direct transition to necrosis at 44 °C [138]. Additionally, some cell lines initially display short-term heat shock tolerance but subsequently experience reduced viability, as seen in melanoma (Bowes) cells and lung adenocarcinoma cells [136], [139]

The response of cytoskeletal structure to heat shock also varies widely depending on factors such as cell type, attained temperature, and duration of heating. N. K. Prasad *et al.* observed that following hyperthermia treatment, Hela cells demonstrated varying degrees of membrane blebbing, accompanied by notable disruption of actin and tubulin cytoskeletons [140]. This disruption was posited as a potential cause of cell death following hyperthermia treatment. In a study by Garcia M. *et al.*, acute and long-term impacts of hyperthermia (45 °C, 30 min, in a water bath) on the B16-F10 murine melanoma cell line were investigated [141]. Immediate harmful effects were observed post-heating, with diminished peripheral F-actin (filamentous actin) rings after 3 hours and altered F-actin cytoskeleton, loss of cell boundaries, cell shrinkage, and nuclear material condensation after 24 hours. Additional effects encompassed disruption of cell layer organization, intercellular contact, and a substantial reduction in attached cell count.

Following the resazurin assay, cells were fixed at 3- and 24-hours post-hyperthermia treatment, permeabilized, and stained using Actin-staining™ 555 Phalloidin Red and DAPI. Samples were visualized via an epi-fluorescence microscope (Nikon Eclipse Ti-S), with results presented for fibroblast, melanoma, and macrophage cell lines in Figure 4.21, Figure 4.22 and Figure 4.23, respectively. The outcomes aligned with the resazurin assays, highlighting a reduction in viability, particularly within the WM983b cell line. Additionally, a reduction in the definition and intensity of the actin filament-marking fluorophore was observed. After 24 h, a comprehensive disruption of actin filaments was apparent, with only a few nuclei stained by DAPI. This correlates with the substantial decrease in cell viability previously noted. Actin cytoskeleton cleavage and disruption are frequently observed during apoptosis [86]–[88]. The decrease in cell viability over time also supports the hypothesis that the cytoskeletons of the treated cells were disrupted, thereby triggering the initiation of a signal leading to cell death. While some features described in the literature, such as loss of cell boundaries, cellular shrinkage, cytoplasmic contraction, and nuclear material condensation, were not evident in the images presented, these observations should be further explored [138], [141]. Furthermore, marking microtubules could provide insight, as they are reported to be more sensitive to hyperthermia [140]. Given the anticipated generation of deleterious substances like free radicals and ROS due to elevated temperatures, assessing their formation could offer valuable insights into cellular stress [142]. In addition to oxidative stress an analysis of caspases activity or lysosomal behavior would also be important.

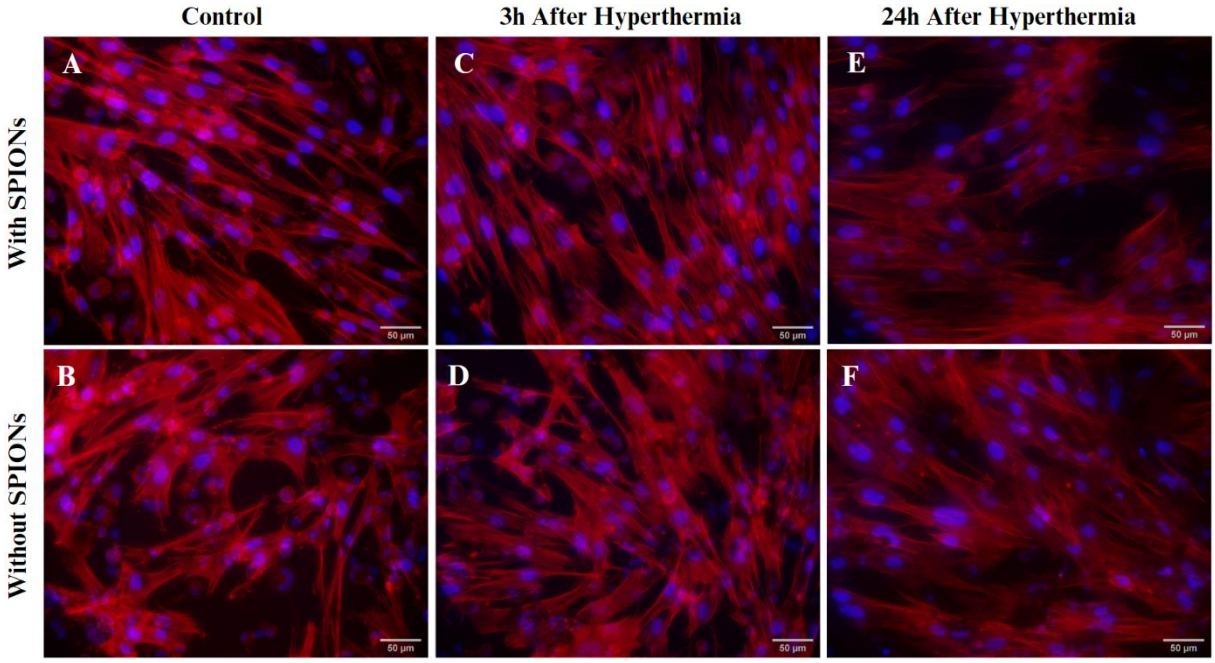

Figure 4.21 | **Fluorescence images of fibroblast HFFF2 cells stained with phalloidin (F-actin filaments in red) and DAPI (nucleus in blue) 3 h and 24 h after sand bath hyperthermia.** The influence of exposure to 100 µg/mL of APTES-coated SPIONs during 24 h of pre-heating incubation was also tested. Unheated control cells shown in the first column (A, B). Scale bar: 50 µm.

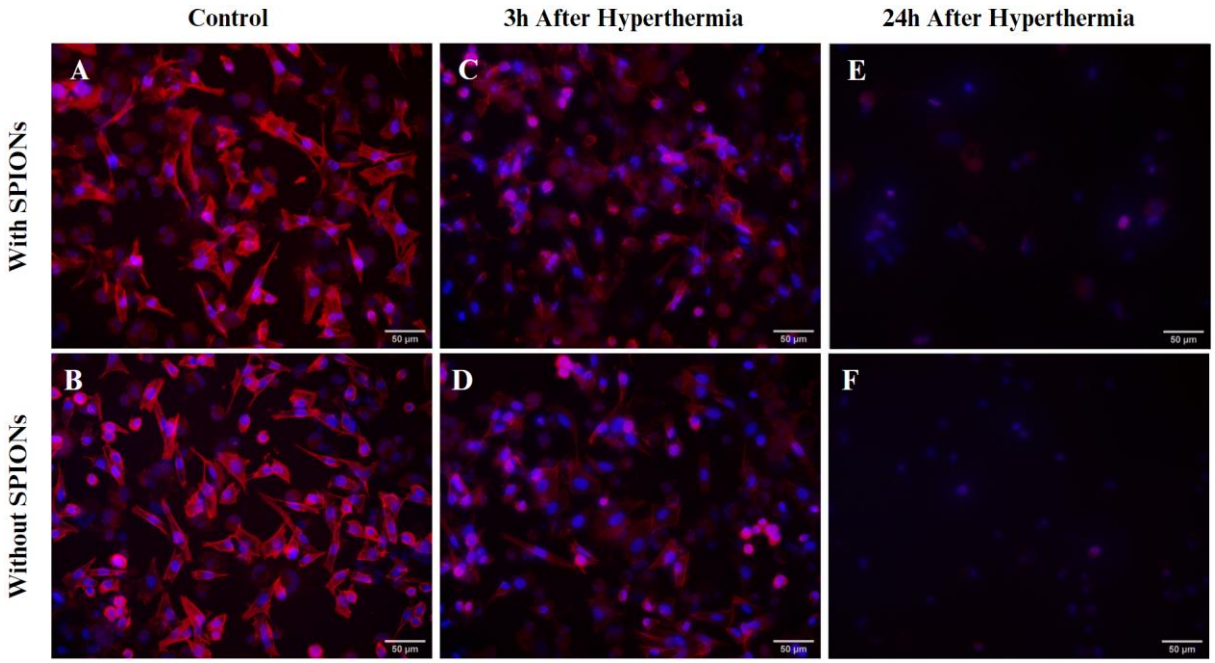

Figure 4.22 | **Fluorescence images of melanoma WM983b cells stained with phalloidin (F-actin filaments in red) and DAPI (nucleus in blue) 3 h and 24 h after sand bath hyperthermia.** The influence of exposure to 100 µg/mL of APTES-coated SPIONs during 24 h of pre-heating incubation was also tested. Unheated control cells shown in the first column (A, B). Scale bar: 50 µm.

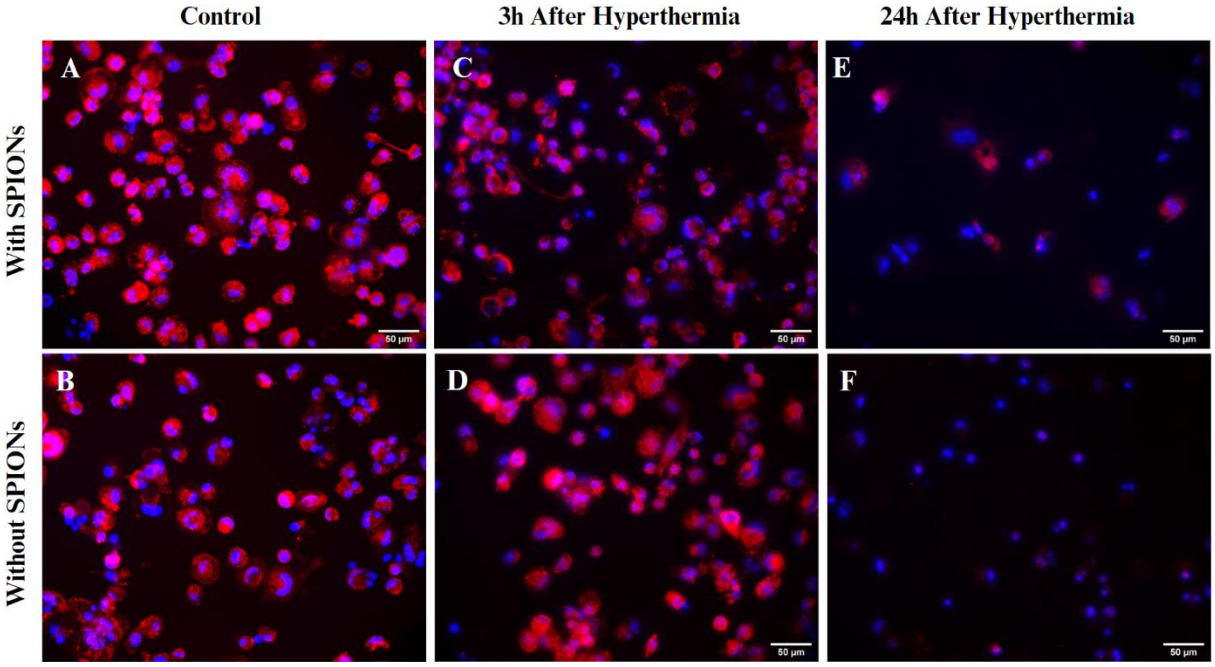

Figure 4.23 | **Fluorescence images of THP-1 macrophage-like cells stained with phalloidin (F-actin filaments in red) and DAPI (nucleus in blue) 3 h and 24 h after sand bath hyperthermia.** The influence of exposure to 100 µg/mL of APTES-coated SPIONs during 24 h of pre-heating incubation was also tested. Unheated control cells shown in the first column (A, B). Scale bar: 50 µm.

5. CONCLUSION AND FUTURE PERSPECTIVES

Emerging nanotechnological discoveries and the unique properties of bionanomaterials have given rise to new approaches to improving cancer therapies. Specifically, SPIONs take advantage of their ability to dissipate heat locally under an AMF. This method, called MH, exploits the increased sensitivity of cancer cells to changes in temperature, leading to their death. Nonetheless, the intricacies of the cell death mechanism triggered by this therapy are highly complex and contingent on a multitude of factors. This complexity underscores its significance as a focal point for investigation within the current scientific community. Having said that, the primary goal of the presented work was to explore different SPIONs coatings and assess their potential for use in MH. The central emphasis was on examining the stability of these materials, comprehending how the type of coating influences the interaction with the different cells and understanding the mechanism of cell death induced by the therapy.

Following the synthesis through the chemical co-precipitation method, SPIONs underwent functionalization with three distinct coatings: OA, DMSA, and APTES. Characterization involved various techniques, including FTIR, TGA, XRD, TEM, DLS, and MH. Examination of FTIR and TGA spectra confirmed the stabilization process in the synthesized SPIONs. XRD and TEM results indicated that SPIONs maintained their average core size and morphological structure, preserving crystalline properties.

To assess the influence of stabilizing agents, DLS and ζ -potential studies determined Dh and charge of the modified SPIONs. Different concentrations of NPs in water were tested revealing significant variations in the hydrodynamic size among the different types of coated SPIONs. At a concentration of 0.05 mg/mL the results obtained were approximately 93, 201 and 90 nm for the SPIONs coated with OA, DMSA and APTES, respectively. For the same order of NPs, the superficial charges obtained were approximately -63.7 ± 1.5 mV and -46.3 ± 7.8 mV and +30.5 ± 5.8 mV. However, it was possible to observe that both the Dh and ζ -potential values varied from synthesis to synthesis. Therefore, an understanding and control of the various factors influencing the hydrodynamic size and charge of the NPs are crucial details to achieve better homogeneity of results. Finally, a MH analysis was carried out in order to observe the SAR and ΔT values of the produced SPIONs when exposed to a magnetic field strength of 300 Gauss and a frequency of 388.4 kHz. At a concentration of 5 mg/mL, ΔT values obtained were 30.2 ± 1.7 °C, 24.2 ± 0.8 °C and 19.5 ± 0.6 °C for the OA-coated SPIONs, the DMSA-coated NPs and the APTES-coated NPs, respectively. Similarly, the SAR values at the same coating order were 190 ± 5 W/g, 149 ± 11 W/g and 119 ± 11 W/g.

After fully characterizing the coated SPIONs, studies were carried out to assess their stability under different conditions. Firstly, the ζ -potential of the different SPIONs was evaluated using 1x PBS as well as the various culture media. As expected, the values were closer to zero in PBS, and this effect became more pronounced when the NPs were exposed to the different cell media due to the neutralization carried out by the PC formed. Dh measurements at different incubation times demonstrated rapid protein adsorption without linear variation. APTES-coated SPIONs exhibited the largest hydrodynamic sizes, aligning with the tendency of initially positively charged NPs to form larger PCs. It is worth acknowledging that because the measurements were not done in filtered MiliQ water, there could have been potential influences from components within the medium. Finally, the ΔT and SAR values were measured 1, 3 and 6 months after synthesis. Over time, ΔT and SAR values decreased, with APTES-coated SPIONs showing the least significant decline at the end of the 3-month period.

Cytotoxicity tests across three cell lines (HFFF2, WM983b, and THP-1) revealed different responses: OA-coated SPIONs displayed cytotoxicity at 0.5 mg/mL, DMSA-coated SPIONs showed the least cytotoxicity, and APTES-coated SPIONs demonstrated moderate cytotoxicity in fibroblast and macrophage cell lines. Subsequently, an internalization assay was carried out to study the interaction between the synthesized SPIONs and the three cell lines mentioned. The results indicated increased NPs internalization over time in all cell lines, with APTES-coated SPIONs showing greater uptake due to its positive surface charge. The melanoma cell line exhibited the least NPs internalization, what is potentially advantageous for MH since studies indicate that extracellular MH results in greater heating efficiency of the SPIONs.

Regarding the *in vitro* MH assay carried out in hyperthermia flasks, APTES-coated SPIONs caused a more significant reduction in viability in line with the higher temperatures reached and, once again, the melanoma cell line showed greater sensitivity to temperature increase. On the other hand, OA and DMSA-coated SPIONs failed to reach the therapeutic temperature range under the conditions tested, but it was also possible to notice a greater sensitivity on the part of WM983b to these SPIONs.

Lastly, a resazurin test was conducted on all three cell lines, subjecting them to a temperature range of 41 – 44 °C for one hour in a sand bath, while exposed to a concentration of 100 μg/mL of APTES-coated SPIONs. Once more, there was notable sensitivity in the melanoma cell line and comparatively less sensitivity observed in fibroblasts. It should also be noted that the presence of SPIONs led to a greater decrease in viability, although this was not an MH assay. The images obtained from the fluorescence assay with labeling of the nuclei and actin filaments aligned with the resazurin assay, highlighting a reduction in viability, particularly in the WM983b cell line. In addition, a reduction in the definition and intensity of the fluorophore marking the actin filaments of these cells was observed and, after 24 hours, complete rupture of the actin filaments was evident, with only a few nuclei stained by DAPI. Fibroblast cell line remained unaffected by both SPION presence and temperature.

In summary, this work delves into the behavior, stability, cytotoxicity, internalization, and hyperthermia potential of SPIONs coated with OA, DMSA, and APTES across various cell lines, with a specific focus on melanoma. Notably, SPIONs coated with APTES seemed to exhibit the most promising characteristics for the intended application. We are confident that the initially outlined objectives

have been successfully accomplished and that this work underscores the critical role of the coating employed and highlights the multitude of factors that demand consideration.

It will be of great interest to optimize the method of synthesis as well as functionalization to achieve a better homogeneity of the sizes and charges obtained. Additionally, a detailed examination of protein adsorption on SPIONs surfaces would be interesting to compare internalization processes between cationic and anionic SPIONs and their subsequent impact on hyperthermia and cell death mechanisms. Exploring the feasibility of achieving therapeutic temperatures with lower NP concentrations in hyperthermia tests would also be important. Moreover, regarding the *in vitro* assays, it would be valuable to carry them out on the planar applicator to facilitate subsequent studies. These expanded studies might include evaluating caspase activity, ROS production, or susceptibility to LMP. To mimic the tumor environment more accurately, the interaction of these SPIONs could be assessed in spheroids composed of the three cell lines. This approach would not only enhance our understanding of SPIONs internalization by the different cell lines but also provide insights into the evolution of cell death under repeated hyperthermia cycles in a more realistic setting.

While this technique displays significant promise for the future, its underlying mechanism remains intricate, leaving several unanswered questions. Therefore, additional research is imperative to fully comprehend the nanoscale heating mechanisms and the complete spectrum of biological effects stemming from this exposure. That said, research efforts like the one presented hold significant value in advancing the exploration of this therapy for clinical application.

6. BIBLIOGRAPHY

[1] J. M. Lourenço, 'NOVAthesis Word template for FCT-NOVA'. NOVA University Lisbon, 2021. Accessed: Sep. 28, 2023. [Online]. Available: https://docentes.fct.unl.pt/joao-lourenco/announcements/novathesis-word-template-fct-nova

[2] F. Bray, M. Laversanne, E. Weiderpass, and I. Soerjomataram, 'The ever-increasing importance of cancer as a leading cause of premature death worldwide', *Cancer*, vol. 127, no. 16, pp. 3029–3030, Aug. 2021, doi: 10.1002/cncr.33587.

[3] World Health Organization, 'Cancer', Cancer. Accessed: Aug. 23, 2023. [Online]. Available: https://www.who.int/en/news-room/fact-sheets/detail/cancer

[4] International Agency for Research on Cancer, 'Cancer Tomorrow'. Accessed: Aug. 23, 2023. [Online]. Available: https://gco.iarc.fr/tomorrow/en/dataviz/isotype?types=1&single_unit=500000

[5] C. S. Nascimento, É. A. R. Alves, C. P. De Melo, R. Corrêa-Oliveira, and C. E. Calzavara-Silva, 'Immunotherapy for cancer: Effects of iron oxide nanoparticles on polarization of tumor-associated macrophages', *Nanomedicine*, vol. 16, no. 29. Future Medicine Ltd., pp. 2633–2650, Dec. 01, 2021. doi: 10.2217/nnm-2021-0255.

[6] K. Saginala, A. Barsouk, J. S. Aluru, P. Rawla, and A. Barsouk, 'Epidemiology of Melanoma', *Medical sciences (Basel, Switzerland)*, vol. 9, no. 4. NLM (Medline), Oct. 20, 2021. doi: 10.3390/medsci9040063.

[7] M. G. Davey, N. Miller, and N. M. McInerney, 'A Review of Epidemiology and Cancer Biology of Malignant Melanoma', *Cureus*, May 2021, doi: 10.7759/cureus.15087..

[8] M. Song, C. Liu, S. Chen, and W. Zhang, 'Nanocarrier-based drug delivery for melanoma therapeutics', *International Journal of Molecular Sciences*, vol. 22, no. 4. MDPI AG, pp. 1–19, Feb. 02, 2021. doi: 10.3390/ijms22041873.

[9] M. Shevtsov, S. Kaesler, C. Posch, G. Multhoff, and T. Biedermann, 'Magnetic nanoparticles in theranostics of malignant melanoma', vol. 11, p. 127, 2021, doi: 10.1186/s13550-021-00868-6.

[10] D. Burns *et al.*, 'The Pathogenesis and Clinical Management of Cutaneous Melanoma: An Evidence-Based Review', *J Med Imaging Radiat Sci*, vol. 50, no. 3, pp. 460-469.e1, Sep. 2019, doi: 10.1016/j.jmir.2019.05.001.

[11] J. Chen, R. Shao, X. D. Zhang, and C. Chen, 'Applications of nanotechnology for melanoma treatment, diagnosis, and theranostics', *International Journal of Nanomedicine*, vol. 8. pp. 2677–2688, Jul. 23, 2013. doi: 10.2147/IJN.S45429.

[12] A. Nishikawa, Y. Suzuki, M. Kaneko, and A. Ito, 'Combination of magnetic hyperthermia and immunomodulators to drive complete tumor regression of poorly immunogenic melanoma', *Cancer Immunology, Immunotherapy*, vol. 72, no. 6, pp. 1493–1504, Jun. 2023, doi: 10.1007/S00262-022-03345-8/METRICS.

[13] J. D. Rybka, 'Radiosensitizing properties of magnetic hyperthermia mediated by superparamagnetic iron oxide nanoparticles (SPIONs) on human cutaneous melanoma cell lines', *Reports of Practical Oncology and Radiotherapy*, vol. 24, no. 2, pp. 152–157, Mar. 2019, doi: 10.1016/J.RPOR.2019.01.002

[14] R. R. Oliveira *et al.*, 'Paclitaxel-Loaded Lipid-Coated Magnetic Nanoparticles for Dual Chemo-Magnetic Hyperthermia Therapy of Melanoma', *Pharmaceutics*, vol. 15, no. 3, p. 818, Mar. 2023, doi: 10.3390/PHARMACEUTICS15030818/S1.

[15] J. D. Wolchok *et al.*, 'Long-Term Outcomes With Nivolumab Plus Ipilimumab or Nivolumab Alone Versus Ipilimumab in Patients With Advanced Melanoma', *Journal of Clinical Oncology*, vol. 40, no. 2, pp. 127–137, Jan. 2022, doi: 10.1200/JCO.21.02229.

[16] M. A. Postow *et al.*, 'A prospective, phase 1 trial of nivolumab, ipilimumab, and radiotherapy in patients with advanced melanoma', *Clinical Cancer Research*, vol. 26, no. 13, pp. 3193–3201, Jul. 2020, doi: 10.1158/1078-0432.CCR-19-3936..

[17] J. L. Roti, 'Cellular responses to hyperthermia (40-46°C): Cell killing and molecular events', in International Journal of Hyperthermia, pp. 3–15. Feb. 2008, doi: 10.1080/02656730701769841.

[18] W. B. Coley, 'The Treatment of Inoperable Sarcoma by Bacterial Toxins (the Mixed Toxins of the Streptococcus erysipelas and the Bacillus prodigiosus)', *Proc R Soc Med*, vol. 3, no. Surg Sect, p. 1, Jun. 1910, doi: 10.1177/003591571000301601.

[19] N. M. Bleehen and G. C. W. Howard, 'Clinical Hyperthermia: Methods and Results', *Radiobiology in Radiotherapy*, pp. 209–231, 1988, doi: 10.1007/978-1-4471-1603-5_18.

[20] G. Franco. Baronzio and E. Dieter. Hager, *Hyperthermia in cancer treatment : a primer*. Landes Bioscience, 2006, doi: 10.4172/2329-67771.1000115.

[21] A. Mizuno *et al*. 'Plasma Biological Science in Various Species', *Plasma Medical Science*, pp. 109–171, Jan. 2019, doi: 10.1016/B978-0-12-815004-7.00003-2.

[22] J. van der Zee, 'Heating the patient: A promising approach?', *Annals of Oncology*, vol. 13, no. 8. pp. 1173–1184, Aug. 2002. doi: 10.1093/annonc/mdf280.

[23] A. Farzin, S. A. Etesami, J. Quint, A. Memic, and A. Tamayol, 'Magnetic Nanoparticles in Cancer Therapy and Diagnosis', *Adv Healthc Mater*, vol. 9, no. 9, p. 1901058, May 2020, doi: 10.1002/ADHM.201901058.

[24] I. Rubia-Rodríguez *et al.*, 'Whither magnetic hyperthermia? A tentative roadmap', *Materials*, vol. 14, no. 4, pp. 1–37, Feb. 2021, doi: 10.3390/ma14040706.

[25] X. Liu *et al.*, 'Comprehensive understanding of magnetic hyperthermia for improving antitumor therapeutic efficacy', *Theranostics*, vol. 10, no. 8, p. 3793, 2020, doi: 10.7150/THNO.40805.

[26] C. Isabel, 'Application of Hyperthermia for Cancer Treatment: Synthesis and Characterization of Magnetic Nanoparticles and their internalization on Tumor Cell Lines', NOVA SST, Master Thesis, 2017.

[27] S. Laurent, S. Dutz, U. O. Häfeli, and M. Mahmoudi, 'Magnetic fluid hyperthermia: focus on superparamagnetic iron oxide nanoparticles', *Adv Colloid Interface Sci*, vol. 166, no. 1–2, pp. 8–23, Aug. 2011, doi: 10.1016/J.CIS.2011.04.003.

[28] M. Mahmoudi, A. Simchi, and M. Imani, 'Iranian Chemical Society Recent Advances in Surface Engineering of Superparamagnetic Iron Oxide Nanoparticles for Biomedical Applications', 2010, doi: 10.1007/BF03246181.

[29] V. I. Shubayev, T. R. Pisanic, and S. Jin, 'Magnetic nanoparticles for theragnostics', *Advanced Drug Delivery Reviews*, vol. 61, no. 6. pp. 467–477, Jun. 21, 2009. doi: 10.1016/j.addr.2009.03.007.

[30] A. V. Samrot, C. S. Sahithya, J. Selvarani A, S. K. Purayil, and P. Ponnaiah, 'A review on synthesis, characterization and potential biological applications of superparamagnetic iron oxide nanoparticles', *Current Research in Green and Sustainable Chemistry*, vol. 4. Elsevier B.V., Jan. 01, 2021. doi: 10.1016/j.crgsc.2020.100042.

[31] R. K. Gilchrist. *et al.*, 'Selective Inductive Heating of Lymph Nodes', *Ann Surg*, vol. 146, no. 4, p. 596, Oct. 1957, doi: 10.1097/00000658-195710000-00007.

[32] A. Jordan *et al.*, 'Cellular uptake of magnetic fluid particles and their effects on human adenocarcinoma cells exposed to AC magnetic fields in vitro', *Int J Hyperthermia*, vol. 12, no. 6, pp. 705–722, 1996, doi: 10.3109/02656739609027678.

[33] K. Maier-Hauff *et al.*, 'Efficacy and safety of intratumoral thermotherapy using magnetic iron-oxide nanoparticles combined with external beam radiotherapy on patients with recurrent glioblastoma multiforme', *J Neurooncol*, vol. 103, no. 2, pp. 317–324, Jun. 2011, doi: 10.1007/s11060-010-0389-0.

[34] A. Jordan *et al.*, 'Presentation of a new magnetic field therapy system for the treatment of human solid tumors with magnetic fluid hyperthermia', *J Magn Magn Mater*, vol. 225, no. 1–2, pp. 118–126, Jan. 2001, doi: 10.1016/S0304-8853(00)01239-7.

[35] S. V. Spirou, M. Basini, A. Lascialfari, C. Sangregorio, and C. Innocenti, 'Magnetic hyperthermia and radiation therapy: Radiobiological principles and current practice', *Nanomaterials*, vol. 8, no. 6. MDPI AG, Jun. 03, 2018. doi: 10.3390/nano8060401.

[36] M. Johannsen *et al.*, 'Morbidity and quality of life during thermotherapy using magnetic nanoparticles in locally recurrent prostate cancer: Results of a prospective phase I trial', *International Journal of Hyperthermia*, vol. 23, no. 3, pp. 315–323, 2007, doi: 10.1080/02656730601175479.

[37] K. Maier-Hauff *et al.*, 'Intracranial thermotherapy using magnetic nanoparticles combined with external beam radiotherapy: Results of a feasibility study on patients with glioblastoma multiforme', *J Neurooncol*, vol. 81, no. 1, pp. 53–60, Jan. 2007, doi: 10.1007/s11060-006-9195-0.

[38] M. Johannsen, B. Thiesen, P. Wust, and A. Jordan, 'Magnetic nanoparticle hyperthermia for prostate cancer', *International Journal of Hyperthermia*, vol. 26, no. 8, pp. 790–795, Dec. 2010, doi: 10.3109/02656731003745740.

[39] M. Johannsen *et al.*, 'Clinical hyperthermia of prostate cancer using magnetic nanoparticles: Presentation of a new interstitial technique', *International Journal of Hyperthermia*, vol. 21, no. 7, pp. 637–647, Nov. 2005, doi: 10.1080/02656730500158360.

[40] F. K. H. van Landeghem *et al.*, 'Post-mortem studies in glioblastoma patients treated with thermotherapy using magnetic nanoparticles', *Biomaterials*, vol. 30, no. 1, pp. 52–57, Jan. 2009, doi: 10.1016/J.BIOMATERIALS.2008.09.044.

[41] F. Rodríguez *et al.*, 'Nano-Based Approved Pharmaceuticals for Cancer Treatment: Present and Future Challenges', *Biomolecules*, vol. 12, no. 6. MDPI, Jun. 01, 2022. doi: 10.3390/biom12060784.

[42] K. Wu, D. Su, J. Liu, R. Saha, and J. P. Wang, 'Magnetic nanoparticles in nanomedicine: a review of recent advances', *Nanotechnology*, vol. 30, no. 50, p. 502003, Sep. 2019, doi: 10.1088/1361-6528/AB4241.

[43] A. Gonçalves *et al.*, 'Engineering dual-stimuli responsive poly(vinyl alcohol) nanofibrous membranes for cancer treatment by magnetic hyperthermia', *Biomaterials Advances*, vol. 145, p. 213275, Feb. 2023, doi: 10.1016/J.BIOADV.2022.213275.

[44] D. Nieciecka *et al.*, 'Hybrid system for local drug delivery and magnetic hyperthermia based on spions loaded with doxorubicin and epirubicin', *Pharmaceutics*, vol. 13, no. 4, 2021, doi: 10.3390/pharmaceutics13040480.

[45] K. R. Wierzbinski *et al.*, 'Potential use of superparamagnetic iron oxide nanoparticles for in vitro and in vivo bioimaging of human myoblasts', *Sci Rep*, vol. 8, no. 1, Dec. 2018, doi: 10.1038/s41598-018-22018-0.

[46] Y. Du, X. Liu, Q. Liang, X. J. Liang, and J. Tian, 'Optimization and Design of Magnetic Ferrite Nanoparticles with Uniform Tumor Distribution for Highly Sensitive MRI/MPI Performance and Improved Magnetic Hyperthermia Therapy', *Nano Lett*, vol. 19, no. 6, pp. 3618–3626, Jun. 2019, doi: 10.1021/ACS.NANOLETT.9B00630.

[47] A. M. M. Dias *et al.*, 'Superparamagnetic Iron Oxide Nanoparticles for Immunotherapy of Cancers through Macrophages and Magnetic Hyperthermia', *Pharmaceutics*, vol. 14, no. 11. MDPI, Nov. 01, 2022. doi: 10.3390/pharmaceutics14112388.

[48] G. Hannon, A. Bogdanska, Y. Volkov, and A. Prina-Mello, 'Comparing the effects of intracellular and extracellular magnetic hyperthermia on the viability of BxPC-3 cells', *Nanomaterials*, vol. 10, no. 3, Mar. 2020, doi: 10.3390/nano10030593.

[49] P. I. P. Soares *et al.*, 'Iron oxide nanoparticles stabilized with a bilayer of oleic acid for magnetic hyperthermia and MRI applications', *Appl Surf Sci*, vol. 383, pp. 240–247, Oct. 2016, doi: 10.1016/J.APSUSC.2016.04.181.

[50] M. Rahman, A. A. Saei, H. Amiri, and M. Mahmoudi, 'Biomedical Applications of Superparamagnetic Nanoparticles in Molecular Scale', *Curr Org Chem*, vol. 19, no. 11, pp. 982–990, Jun. 2015, doi: 10.2174/1385272819111506101005 48.

[51] A. Akbarzadeh, M. Samiei, and S. Davaran, 'Magnetic nanoparticles: Preparation, physical properties, and applications in biomedicine', *Nanoscale Res Lett*, vol. 7, 2012, doi: 10.1186/1556-276X-7-144.

[52] J. Wallyn, N. Anton, and T. F. Vandamme, 'Synthesis, principles, and properties of magnetite nanoparticles for in vivo imaging applications—A review', *Pharmaceutics*, vol. 11, no. 11. MDPI AG, Nov. 01, 2019. doi: 10.3390/pharmaceutics11110601.

[53] I. M. Obaidat, V. Narayanaswamy, S. Alaabed, S. Sambasivam, and C. V. V. Muralee Gopi, 'Principles of magnetic hyperthermia: A focus on using multifunctional hybrid magnetic nanoparticles', *Magnetochemistry*, vol. 5, no. 4. MDPI, Dec. 01, 2019. doi: 10.3390/magnetochemistry5040067.

[54] A. E. Deatsch and B. A. Evans, 'Heating efficiency in magnetic nanoparticle hyperthermia', *Journal of Magnetism and Magnetic Materials*, vol. 354. pp. 163–172, 2014. doi: 10.1016/j.jmmm.2013.11.006.

[55] R. T. Holladay, L. Winfrey, M. A. Pierson, and A. S. Goldstein, 'Incorporating Magnetic Nanoparticle Aggregation Effects into Heat Generation and Temperature Profiles for Magnetic Hyperthermia Treatments', Virginia Teck, Master Thesis, 2015.

[56] M. Arruebo, R. Fernández-Pacheco, M. R. Ibarra, and J. Santamaría, 'Magnetic nanoparticles for drug delivery', *Nano Today*, vol. 2, no. 3, pp. 22–32, Jun. 2007, doi: 10.1016/S1748-0132(07)70084-1

[57] S. Shrestha, B. Wang, and P. Dutta, 'Nanoparticle processing: Understanding and controlling aggregation', *Advances in Colloid and Interface Science*, vol. 279. Elsevier B.V., May 01, 2020. doi: 10.1016/j.cis.2020.102162.

[58] H. Sun, C. Jiang, L. Wu, X. Bai, and S. Zhai, 'Cytotoxicity-Related Bioeffects Induced by Nanoparticles: The Role of Surface Chemistry', *Frontiers in Bioengineering and Biotechnology*, vol. 7. Frontiers Media S.A., Dec. 12, 2019. doi: 10.3389/fbioe.2019.00414.

[59] A. Petri-Fink, B. Steitz, A. Finka, J. Salaklang, and H. Hofmann, 'Effect of cell media on polymer coated superparamagnetic iron oxide nanoparticles (SPIONs): Colloidal stability, cytotoxicity, and cellular uptake studies', *European Journal of Pharmaceutics and Biopharmaceutics*, vol. 68, no. 1, pp. 129–137, Jan. 2008, doi: 10.1016/J.EJPB.2007.02.024.

[60] W. Mekseriwattana, S. Srisuk, R. Kriangsaksri, N. Niamsiri, and K. Prapainop, 'The Impact of Serum Proteins and Surface Chemistry on Magnetic Nanoparticle Colloidal Stability and Cellular

Uptake in Breast Cancer Cells', *AAPS PharmSciTech*, vol. 20, no. 2, pp. 1–9, Feb. 2019, doi: 10.1208/S12249-018-1275-X/METRICS.

[61] K. Nienhaus and G. U. Nienhaus, 'Mechanistic Understanding of Protein Corona Formation around Nanoparticles: Old Puzzles and New Insights', *Small*. John Wiley and Sons Inc, Jul. 12, 2023. doi: 10.1002/smll.202301663.

[62] G. Bashiri, M. S. Padilla, K. L. Swingle, S. J. Shepherd, M. J. Mitchell, and K. Wang, 'Nanoparticle protein corona: from structure and function to therapeutic targeting', *Lab on a Chip*, vol. 23, no. 6. Royal Society of Chemistry, pp. 1432–1466, Jan. 19, 2023. doi: 10.1039/d2lc00799a.

[63] Y. Portilla *et al.*, 'Iron oxide nanoparticle coatings dictate cell outcomes despite the influence of protein coronas', *ACS Appl Mater Interfaces*, vol. 13, no. 7, pp. 7924–7944, Feb. 2021, doi: 10.1021/acsami.0c20066.

[64] M. P. Calatayud, B. Sanz, V. Raffa, C. Riggio, M. R. Ibarra, and G. F. Goya, 'The effect of surface charge of functionalized Fe3O4 nanoparticles on protein adsorption and cell uptake', *Biomaterials*, vol. 35, no. 24, pp. 6389–6399, 2014, doi: 10.1016/j.biomaterials.2014.04.009.

[65] C. Guibert, V. Dupuis, V. Peyre, and J. Fresnais, 'Hyperthermia of Magnetic Nanoparticles: Experimental Study of the Role of Aggregation', *Journal of Physical Chemistry C*, vol. 119, no. 50, pp. 28148–28154, Dec. 2015, doi: 10.1021/acs.jpcc.5b07796.

[66] P. I. P. Soares *et al.*, 'Effects of surfactants on the magnetic properties of iron oxide colloids', *J Colloid Interface Sci*, vol. 419, pp. 46–51, Apr. 2014, doi: 10.1016/J.JCIS.2013.12.045.

[67] N. Repar *et al.*, 'Oleic Acid Protects Endothelial Cells from Silica-Coated Superparamagnetic Iron Oxide Nanoparticles (SPIONs)-Induced Oxidative Stress and Cell Death', *Int J Mol Sci*, vol. 23, no. 13, Jul. 2022, doi: 10.3390/ijms23136972.

[68] L. Magtanong *et al.*, 'Exogenous Monounsaturated Fatty Acids Promote a Ferroptosis-Resistant Cell State', *Cell Chem Biol*, vol. 26, no. 3, pp. 420-432.e9, Mar. 2019, doi: 10.1016/j.chembiol.2018.11.016.

[69] X. Zeng *et al.*, 'Oleic acid ameliorates palmitic acid induced hepatocellular lipotoxicity by inhibition of ER stress and pyroptosis', *Nutr Metab (Lond)*, vol. 17, no. 1, Jan. 2020, doi: 10.1186/s12986-020-0434-8.

[70] N. Massironi *et al.*, 'Heparin–Superparamagnetic Iron Oxide Nanoparticles for Theranostic Applications', *Molecules*, vol. 27, no. 20, Oct. 2022, doi: 10.3390/molecules27207116.

[71] A. V. Samrot *et al.*, 'Production and utilization of spions for in-vitro drug release and x-ray imaging', *J Pure Appl Microbiol*, vol. 14, no. 2, pp. 1317–1322, Jun. 2020, doi: 10.22207/JPAM.14.2.27.

[72] F. Paulini *et al.*, 'In Vivo Evaluation of DMSA-Coated Magnetic Nanoparticle Toxicity and Biodistribution in Rats: A Long-Term Follow-Up', *Nanomaterials*, vol. 12, no. 19, Oct. 2022, doi: 10.3390/nano12193513.

[73] A. Ruiz, P. C. Morais, R. Bentes de Azevedo, Z. G. M. Lacava, A. Villanueva, and M. del Puerto Morales, 'Magnetic nanoparticles coated with dimercaptosuccinic acid: development, characterization, and application in biomedicine', *Journal of Nanoparticle Research*, vol. 16, no. 11. Kluwer Academic Publishers, Nov. 01, 2014. doi: 10.1007/s11051-014-2589-6.

[74] M. S. Osman, N. A. Noorossaidy, N. Azis, N. S. Salim, N. A. Zaini, and N. A. A. Bashah, 'Synthesis of dimercaptosuccinic acid (DMSA) coated magnetic nanoparticles: Feasibility on dye decolorization and heavy metal adsorption', in *IOP Conference Series: Materials Science and Engineering*, Institute of Physics Publishing, Aug. 2019. doi: 10.1088/1757-899X/551/1/012125.

[75] Y. Liu, Y. Li, X. M. Li, and T. He, 'Kinetics of (3-aminopropyl)triethoxylsilane (aptes) silanization of superparamagnetic iron oxide nanoparticles', *Langmuir*, vol. 29, no. 49, pp. 15275–15282, Dec. 2013, doi: 10.1021/la403269u.

[76] X. M. Zhu *et al.*, 'Enhanced cellular uptake of aminosilane-coated superparamagnetic iron oxide nanoparticles in mammalian cell lines', *Int J Nanomedicine*, vol. 7, pp. 953–964, 2012, doi: 10.2147/IJN.S28316.

[77] L. Galluzzi *et al.*, 'Molecular mechanisms of cell death: recommendations of the Nomenclature Committee on Cell Death 2018', *Cell Death & Differentiation 2018 25:3*, vol. 25, no. 3, pp. 486–541, Jan. 2018, doi: 10.1038/s41418-017-0012-4.

[78] G. Yan, M. Elbadawi, and T. Efferth, 'Multiple cell death modalities and their key features (Review)', *World Acad Sci J*, vol. 2, no. 2, pp. 39–48, Mar. 2020, doi: 10.3892/WASJ.2020.40/HTML.

[79] P. Syntichaki and N. Tavernarakis, 'Death by necrosis', *EMBO Rep*, vol. 3, no. 7, pp. 604–609, Jul. 2002, doi: 10.1093/EMBO-REPORTS/KVF138.

[80] S. Nagata, 'Apoptosis and Clearance of Apoptotic Cells', *https://doi.org/10.1146/annurev-immunol-042617-053010*, vol. 36, pp. 489–517, Apr. 2018, doi: 10.1146/ANNUREV-IMMUNOL-042617-053010.

[81] A. Hervault and N. T. K. Thanh, 'Magnetic nanoparticle-based therapeutic agents for thermo-chemotherapy treatment of cancer', *Nanoscale*, vol. 6, no. 20, pp. 11553–11573, Sep. 2014, doi: 10.1039/C4NR03482A.

[82] P. Vineis, 'Cancer as an evolutionary process at the cell level: an epidemiological perspective', 2003. Accessed: Aug. 13, 2023. [Online]. Available: http://carcin.oxfordjournals.org/

[83] J. R. Lepock, 'Cellular effects of hyperthermia: Relevance to the minimum dose for thermal damage', in *International Journal of Hyperthermia*, pp. 252–266, May 2003. doi: 10.1080/0265673031000065042.

[84] R. Bazak, M. Houri, S. E. Achy, W. Hussein, and T. Refaat, 'Passive targeting of nanoparticles to cancer: A comprehensive review of the literature', *Mol Clin Oncol*, vol. 2, no. 6, pp. 904–908, Nov. 2014, doi: 10.3892/mco.2014.356.

[85] Y. Oh, N. Lee, H. W. Kang, and J. Oh, ‘In vitro study on apoptotic cell death by effective magnetic hyperthermia with chitosan-coated MnFe2O4’, *Nanotechnology*, vol. 27, no. 11, p. 115101, Feb. 2016, doi: 10.1088/0957-4484/27/11/115101.

[86] M. Desouza, P. W. Gunning, and J. R. Stehn, ‘The actin cytoskeleton as a sensor and mediator of apoptosis’, *Bioarchitecture*, vol. 2, no. 3, pp. 75–87, May 2012, doi: 10.4161/bioa.20975.

[87] Y. Li *et al.*, ‘Mechanical stretching induces fibroblasts apoptosis through activating Piezo1 and then destroying actin cytoskeleton’, *Int J Med Sci*, vol. 20, no. 6, pp. 771–780, 2023, doi: 10.7150/IJMS.81666.

[88] S. M. Laster and J. M. Mackenzie, ‘Bleb formation and F-actin distribution during mitosis and tumor necrosis factor-induced apoptosis’, *Microsc Res Tech*, vol. 34, no. 3, pp. 272–280, 1996, doi: 10.1002/(SICI)1097-0029(19960615)34:3<272::AID-JEMT10>3.0.CO;2-J.

[89] M. Salimi, S. Sarkar, M. Hashemi, and R. Saber, ‘Treatment of Breast Cancer-Bearing BALB/c Mice with Magnetic Hyperthermia using Dendrimer Functionalized Iron-Oxide Nanoparticles’, *Nanomaterials 2020, Vol. 10, Page 2310*, vol. 10, no. 11, p. 2310, Nov. 2020, doi: 10.3390/NANO10112310.

[90] D. Salvador, V. Bastos, and H. Oliveira, ‘Hyperthermia enhances doxorubicin therapeutic efficacy against A375 and MNT-1 melanoma cells’, *Int J Mol Sci*, vol. 23, no. 1, Jan. 2022, doi: 10.3390/ijms23010035.

[91] K. E. A. Duval *et al.*, ‘Immunogenetic effects of low dose (CEM43 30) magnetic nanoparticle hyperthermia and radiation in melanoma cells’, *https://doi.org/10.1080/02656736.2019.1627433*, vol. 36, no. sup1, pp. 37–46, Nov. 2019, doi: 10.1080/02656736.2019.1627433.

[92] Y. Chao *et al.*, ‘Iron Nanoparticles for Low-Power Local Magnetic Hyperthermia in Combination with Immune Checkpoint Blockade for Systemic Antitumor Therapy’, *Nano Lett*, vol. 19, no. 7, pp. 4287–4296, Jul. 2019, doi: 10.1021/ACS.NANOLETT.9B00579.

[93] C. Pucci, A. Degl’Innocenti, M. Belenli Gümüş, and G. Ciofani, ‘Superparamagnetic iron oxide nanoparticles for magnetic hyperthermia: recent advancements, molecular effects, and future directions in the omics era’, *Biomaterials Science*, vol. 10, no. 9. Royal Society of Chemistry, pp. 2103–2121, Mar. 04, 2022. doi: 10.1039/d1bm01963e.

[94] F. Wang, R. Gómez-Sintes, and P. Boya, ‘Lysosomal membrane permeabilization and cell death’, *Traffic*, vol. 19, no. 12. Blackwell Munksgaard, pp. 918–931, Dec. 01, 2018. doi: 10.1111/tra.12613.

[95] A. C. Johansson, H. Appelqvist, C. Nilsson, K. Kågedal, K. Roberg, and K. Öllinger, ‘Regulation of apoptosis-associated lysosomal membrane permeabilization’, *Apoptosis*, vol. 15, no. 5, pp. 527–540, May 2010, doi: 10.1007/S10495-009-0452-5.

[96] M. Domenech, I. Marrero-Berrios, M. Torres-Lugo, and C. Rinaldi, ‘Lysosomal membrane permeabilization by targeted magnetic nanoparticles in alternating magnetic fields’, *ACS Nano*, vol. 7, no. 6, pp. 5091–5101, Jun. 2013, doi: 10.1021/nn4007048.

[97] C. Oberle *et al.*, 'Lysosomal membrane permeabilization and cathepsin release is a Bax/Bak-dependent, amplifying event of apoptosis in fibroblasts and monocytes', *Cell Death & Differentiation 2010 17:7*, vol. 17, no. 7, pp. 1167–1178, Jan. 2010, doi: 10.1038/cdd.2009.214.

[98] P. Clerc *et al.*, 'Targeted Magnetic Intra-Lysosomal Hyperthermia produces lysosomal reactive oxygen species and causes Caspase-1 dependent cell death', *Journal of Controlled Release*, vol. 270, pp. 120–134, Jan. 2018, doi: 10.1016/J.JCONREL.2017.11.050.

[99] L. Beola *et al*., 'The intracellular number of magnetic nanoparticles modulates the apoptotic death pathway after magnetic hyperthermia treatment', ACS Appl Mater Interfaces, vol. 12, no. 39, pp. 43474–43487, Sep. 2020, doi: 10.1021/acsami.0c12900.

[100] B. P. Shah, N. Pasquale, G. De, T. Tan, J. Ma, and K. B. Lee, 'Core-shell nanoparticle-based peptide therapeutics and combined hyperthermia for enhanced cancer cell apoptosis', ACS Nano, vol. 8, no. 9, pp. 9379–9387, Sep. 2014, doi: 10.1021/NN503431X.

[101] M. Talelli *et al.*, 'Superparamagnetic iron oxide nanoparticles encapsulated in biodegradable thermosensitive polymeric micelles: Toward a targeted nanomedicine suitable for image-guided drug delivery', Langmuir, vol. 25, no. 4, pp. 2060–2067, Feb. 2009, doi: 10.1021/la8036499.

[102] N. Fauconnier, J. N. Pons, J. Roger, and A. Bee, 'Thiolation of Maghemite Nanoparticles by Dimercaptosuccinic Acid', J Colloid Interface Sci, vol. 194, no. 2, pp. 427–433, Oct. 1997, doi: 10.1006/JCIS.1997.5125.

[103] M. H. Mashhadizadeh and M. Amoli-Diva, 'Drug-Carrying Amino Silane Coated Magnetic Nanoparticles as Potential Vehicles for Delivery of Antibiotics', 2012, doi: 10.4172/2157-7439.1000139.

[104] A. Aliakbari, M. Seifi, S. Mirzaee, and H. Hekmatara, 'Influence of different synthesis conditions on properties of oleic acid-coated-Fe3O4 nanoparticles', Materials Science- Poland, vol. 33, no. 1, pp. 100–106, Mar. 2015, doi: 10.1515/MSP-2015-0027.

[105] E. S. Martins *et al*., 'Potential Use of DMSA-Containing Iron Oxide Nanoparticles as Magnetic Vehicles against the COVID-19 Disease', ChemistrySelect, vol. 6, no. 31, pp. 7931–7935, Aug. 2021, doi: 10.1002/slct.202101900.

[106] S. I. C. J. Palma, M. Marciello, A. Carvalho, S. Veintemillas-Verdaguer, M. del P. Morales, and A. C. A. Roque, 'Effects of phase transfer ligands on monodisperse iron oxide magnetic nanoparticles', J Colloid Interface Sci, vol. 437, pp. 147–155, Jan. 2015, doi: 10.1016/J.JCIS.2014.09.019.

[107] X. Y. Wang *et al*., 'Optimizing the silanization of thermally-decomposed iron oxide nanoparticles for efficient aqueous phase transfer and MRI applications', RSC Adv, vol. 6, no. 96, pp. 93784–93793, Sep. 2016, doi: 10.1039/C6RA18360C.

[108] F. Senturk, S. Cakmak, and G. G. Ozturk, 'Synthesis and Characterization of Oleic Acid Coated Magnetic Nanoparticles for Hyperthermia Applications', Natural and Applied Sciences Journal, vol. 2, no. 2, pp. 16–29, Dec. 2019, doi: 10.38061/IDUNAS.657975.

[109] K. Petcharoen and A. Sirivat, ‘Synthesis and characterization of magnetite nanoparticles via the chemical co-precipitation method’, Materials Science and Engineering: B, vol. 177, no. 5, pp. 421–427, Mar. 2012, doi: 10.1016/J.MSEB.2012.01.003.

[110] S. Çitoğlu, Ö. D. Coşkun, L. D. Tung, M. A. Onur, and N. T. Kim Thanh, ‘DMSA-coated cubic iron oxide nanoparticles as potential therapeutic agents’, Nanomedicine, vol. 16, no. 11, pp. 925–941, May 2021, doi: 10.2217/nnm-2020-0467.

[111] L. M. AL-Harbi and M. S. A. Darwish, ‘Functionalized iron oxide nanoparticles: synthesis through ultrasonic-assisted co-precipitation and performance as hyperthermic agents for biomedical applications’, Heliyon, vol. 8, no. 6, p. e09654, Jun. 2022, doi: 10.1016/J.HELIYON.2022.E09654.

[112] R. L. Rebodos and P. J. Vikesland, ‘Effects of oxidation on the magnetization of nanoparticulate magnetite’, Langmuir, vol. 26, no. 22, pp. 16745–16753, Nov. 2010, doi: 10.1021/LA102461Z.

[113] A. K. Gupta and M. Gupta, ‘Synthesis and surface engineering of iron oxide nanoparticles for biomedical applications’, Biomaterials, vol. 26, no. 18, pp. 3995–4021, Jun. 2005, doi: 10.1016/J.BIOMATERIALS.2004.10.012.

[114] C. M. Maguire, M. Rösslein, P. Wick, and A. Prina-Mello, ‘Characterisation of particles in solution – a perspective on light scattering and comparative technologies’, Sci Technol Adv Mater, vol. 19, no. 1, p. 732, Dec. 2018, doi: 10.1080/14686996.2018.1517587.

[115] C. Costa *et al*., ‘In vitro cytotoxicity of superparamagnetic iron oxide nanoparticles on neuronal and glial cells. Evaluation of nanoparticle interference with viability tests’, Journal of Applied Toxicology, vol. 36, no. 3, pp. 361–372, Mar. 2016, doi: 10.1002/JAT.3213.

[116] M. Calero *et al*., ‘Efficient and safe internalization of magnetic iron oxide nanoparticles: Two fundamental requirements for biomedical applications’, Nanomedicine, vol. 10, no. 4, pp. 733–743, May 2014, doi: 10.1016/J.NANO.2013.11.010.

[117] S. Arsalani *et al*., ‘Uniform size PEGylated iron oxide nanoparticles as a potential theranostic agent synthesized by a simple optimized coprecipitation route’, J Magn Magn Mater, vol. 564, Dec. 2022, doi: 10.1016/j.jmmm.2022.170091.

[118] L. P. Mona, S. P. Songca, and P. A. Ajibade, ‘Synthesis and encapsulation of iron oxide nanorods for application in magnetic hyperthermia and photothermal therapy’, Nanotechnology Reviews, vol. 11, no. 1. De Gruyter Open Ltd, pp. 176–190, Jan. 01, 2021. doi: 10.1515/ntrev-2022-0011.

[119] I. M. Obaidat, B. Issa, and Y. Haik, ‘Magnetic properties of magnetic nanoparticles for efficient hyperthermia’, Nanomaterials, vol. 5, no. 1. MDPI AG, pp. 63–89, Jan. 09, 2014. doi: 10.3390/nano5010063.

[120] D. J. Pochapski, C. Carvalho Dos Santos, G. W. Leite, S. H. Pulcinelli, and C. V. Santilli, ‘Zeta Potential and Colloidal Stability Predictions for Inorganic Nanoparticle Dispersions: Effects of Experimental Conditions and Electrokinetic Models on the Interpretation of Results’, Langmuir, vol. 37, no. 45, pp. 13379–13389, Nov. 2021, doi: 10.1021/acs.langmuir.1c02056.

[121] S. Tenzer *et al*., 'Rapid formation of plasma protein corona critically affects nanoparticle pathophysiology', Nature Nanotechnology 2013 8:10, vol. 8, no. 10, pp. 772–781, Sep. 2013, doi: 10.1038/nnano.2013.181.

[122] G. Maiorano *et al*., 'Effects of cell culture media on the dynamic formation of protein-nanoparticle complexes and influence on the cellular response', ACS Nano, vol. 4, no. 12, pp. 7481–7491, Dec. 2010, doi: 10.1021/NN101557E.

[123] U. Sakulkhu *et al*., 'Significance of surface charge and shell material of superparamagnetic iron oxide nanoparticle (SPION) based core/shell nanoparticles on the composition of the protein corona', Biomater Sci, vol. 3, no. 2, pp. 265–278, Feb. 2015, doi: 10.1039/C4BM00264D.

[124] O. A. Kulikov *et al*., 'Magnetic Hyperthermia Nanoarchitectonics via Iron Oxide Nanoparticles Stabilised by Oleic Acid: Anti-Tumour Efficiency and Safety Evaluation in Animals with Transplanted Carcinoma', Int J Mol Sci, vol. 23, no. 8, p. 4234, Apr. 2022, doi: 10.3390/IJMS23084234/S1.

[125] E. Fröhlich, 'The role of surface charge in cellular uptake and cytotoxicity of medical nanoparticles', Int J Nanomedicine, vol. 7, pp. 5577–5591, 2012, doi: 10.2147/IJN.S36111.

[126] W. Zhang *et al*., 'Differently Charged Super-Paramagnetic Iron Oxide Nanoparticles Preferentially Induced M1-Like Phenotype of Macrophages', Front Bioeng Biotechnol, vol. 8, p. 544260, May 2020, doi: 10.3389/FBIOE.2020.00537/BIBTEX.

[127] D. Zhang, L. Wei, M. Zhong, L. Xiao, H. W. Li, and J. Wang, 'The morphology and surface charge-dependent cellular uptake efficiency of upconversion nanostructures revealed by single-particle optical microscopy', Chem Sci, vol. 9, no. 23, pp. 5260–5269, Jun. 2018, doi: 10.1039/C8SC01828F.

[128] C. Polasky *et al*., 'Impact of Superparamagnetic Iron Oxide Nanoparticles on THP-1 Monocytes and Monocyte-Derived Macrophages', Front Mol Biosci, vol. 9, p. 811116, Feb. 2022, doi: 10.3389/FMOLB.2022.811116.

[129] D. Cabrera et al., 'Dynamical Magnetic Response of Iron Oxide Nanoparticles Inside Live Cells', ACS Nano, vol. 12, no. 3, pp. 2741–2752, Mar. 2018, doi: 10.1021/acsnano.7b08995

[130] D. Soukup, S. Moise, E. Céspedes, J. Dobson, and N. D. Telling, 'In situ measurement of magnetization relaxation of internalized nanoparticles in live cells', ACS Nano, vol. 9, no. 1, pp. 231–240, Jan. 2015, doi: 10.1021/nn503888j.

[131] S. Dutz, M. Kettering, I. Hilger, R. Müller, and M. Zeisberger, 'Magnetic multicore nanoparticles for hyperthermia—influence of particle immobilization in tumour tissue on magnetic properties', Nanotechnology, vol. 22, no. 26, p. 265102, May 2011, doi: 10.1088/0957-4484/22/26/265102.

[132] B. T. Simões, F. V. Almeida, J. P. Borges, and P. I. P. Soares, 'Extracellular Hyperthermia for the Treatment of Advanced Cutaneous Melanoma', MDPI AG, Jun. 2022, p. 56. doi: 10.3390/materproc2022008056.

[133] L. Sharif-Khatibi, A. Kariminia, S. Khoei, and B. Goliaei, 'Hyperthermia induces differentiation without apoptosis in permissive temperatures in human erythroleukaemia cells', Int J Hyperthermia, vol. 23, no. 8, pp. 645–655, Dec. 2007, doi: 10.1080/02656730701769833.

[134] R. S. Oliveira-Filho, R. G. Bevilacqua, and R. Chammas, "Hyperthermia increases the metastatic potential of murine melanoma," Braz J Med Biol Res, vol. 30, no. 8, pp. 941–945, 1997, doi: 10.1590/S0100-879X1997000800005.

[135] M. Brehmer and I. Svensson, 'Heat-induced apoptosis in human prostatic stromal cells', BJU Int, vol. 85, no. 4, pp. 535–541, 2000, doi: 10.1046/J.1464-410X.2000.00473.X.

[136] M. P. Garcia, J. R. T. Cavalheiro, and M. H. Fernandes, 'Acute and Long-Term Effects of Hyperthermia in B16-F10 Melanoma Cells', PLoS One, vol. 7, no. 4, p. e35489, Apr. 2012, doi: 10.1371/JOURNAL.PONE.0035489.

[137] R. Jayasundar, D. Honess, L. D. Hall, and N. M. Bleehen, 'Simultaneous evaluation of the effects of RF hyperthermia on the intra- and extracellular tumor pH', Magn Reson Med, vol. 43, no. 1, pp. 1–8, 2000, doi: 10.1002/(SICI)1522-2594(200001)43:1<1::AID-MRM1>3.0.CO;2-2.

[138] M. Yonezawa et al., 'hyperthermia induces apoptosis in malignant fibrous histiocytoma cells in vitro', Int J Cancer, vol. 66, no. 3, pp. 347–351, May 1996, doi: 10.1002/(SICI)1097-0215(19960503)66:3<347::AID-IJC14>3.0.CO;2-8.

[139] H. Fukao et al., 'Effect of hyperthermia on the viability and the fibrinolytic potential of human cancer cell lines', Clinica Chimica Acta, vol. 296, no. 1–2, pp. 17–33, Jun. 2000, doi: 10.1016/S0009-8981(00)00198-4.

[140] N. K. Prasad, K. Rathinasamy, D. Panda, and D. Bahadur, 'Mechanism of cell death induced by magnetic hyperthermia with nanoparticles of γ-MnxFe2–xO3 synthesized by a single step process', J Mater Chem, vol. 17, no. 48, pp. 5042–5051, Dec. 2007, doi: 10.1039/B708156A.

[141] M. P. Garcia, J. R. T. Cavalheiro, and M. H. Fernandes, 'Acute and long-term effects of hyperthermia in B16-F10 melanoma cells', PLoS One, vol. 7, no. 4, Apr. 2012, doi: 10.1371/journal.pone.0035489.

[142] K. Ahmed, S. F. Zaidi, Mati-ur-Rehman, R. Rehman, and T. Kondo, 'Hyperthermia and protein homeostasis: Cytoprotection and cell death', J Therm Biol, vol. 91, p. 102615, Jul. 2020, doi: 10.1016/J.JTHERBIO.2020.102615.

[143] F. Babick, 'Dynamic light scattering (DLS)', Characterization of Nanoparticles: Measurement Processes for Nanoparticles, pp. 137–172, Jan. 2020, doi: 10.1016/B978-0-12-814182-3.00010-9.

[144] 'Resazurin Cell Viability Assay | Creative Bioarray'. Accessed: Sep. 06, 2023. [Online]. Available: https://www.creative-bioarray.com/support/resazurin-cell-viability-assay.htm

A. SPIONs

A.1 Spectrophotometric Iron Determination by UV-Vis

After SPIONs synthesis, the 1,10-phenantroline colorimetric was used to determine the quantity of iron from each synthesis [66], [101]. Firstly, each sample was sonicated for about 30 seconds and then were added to 5 Eppendorf tubes. Afterwards, 40 μL of the SPIONs diluted solution were added in each tube followed by the addition of 20 μL of HCl 37% (v/v) (Panreac). The samples were then incubated at room temperature for an hour to dissolve all the SPIONs and generate ferrous and ferric chlorides. Subsequently, to reduce Fe^{3+} to Fe^{2+} and form the orange-red iron tris (1,10-phenanthroline) (II) complex, 100 μL of a hydroxylamine-hydrate solution (Sigma-Aldrich) at a concentration of 100 mg. mL^{-1} and 500 μL of a 1,10-phenanthroline monohydrate solution (Sigma-Aldrich) at a concentration of 3 mg. mL^{-1} were added to the samples. Subsequently, the samples were diluted to 1800 μL using 500 mM ammonium acetate (Panreac) pH 4 buffer, and absorbance readings at 510 nm were obtained using a UV-Vis spectrophotometer (T90+ UV/VIS Spectrometer, PG Instruments Ltd.). All three mentioned solutions were prepared beforehand using 0.01 N HCl as the solvent. Using a calibration curve that was obtained using (Mohr's salt solution in HCl 0.01 N in a concentration range of 10 to 1000 μg/mL), the concentration of iron (II) was quantified.

Iron (II) concentration was determined using equation A.1:

$$\mathrm{Abs}_{510} = 4.5079 \times [\mathrm{Fe}] + 0.0753 \quad \text{(A.1)}$$

SPIONs concentration was obtained using equation A.2 (where D.F denotes Dilution factor):

$$[\mathrm{SPIONs}] = ([\mathrm{Fe}] \times \mathrm{D.F})/0.7 \quad \text{(A.2)}$$

A.2 Characterization

FTIR

FTIR spectroscopy is a type of absorption spectroscopy used to identify and characterize the chemical constituents of substances based on their interaction with infrared radiation (IR). Briefly, when IR passes through a sample some is absorbed and some is transmitted and, by using the Fourier Transform, the detector's output can be transformed into a readable spectrum. Each type of chemical bond absorbs IR at specific frequencies, creating distinctive absorption patterns that can be used to identify the functional groups and molecular structures of the sample.

For analysis, the three types of coated SPIONs were freeze-dried for 24 hours (VaCO 2 ZIRBUS technology) and the spectra were obtain using FTIR Nicolet 6700 (Thermo Electron Corporation) with attenuated total reflectance (ATR) with an incident angle of 45° in the range of 4000 – 480 cm^{-1}.

TEM

TEM is an advanced microscopy technique that relies on the interaction between a high-energy electron beam (80 keV or more) and a solid sample. High resolution images are produced with this method allowing the acquisition of detailed information about the sample under analysis.

For this work the images were obtained from solutions of the different types of SPIONs diluted in ultrapure water at a concentration of 0.5 µg/mL. The diluted samples were placed on a 25 mesh Kevlar grid for analysis and images were obtained in a Hitachi H-8100 II with LaB6 thermionic emission.

XRD

XRD is a widely used technique for analyzing the structure of crystalline materials. It is based on the principle that, when the sample is subjected to X-rays, they interfere with the crystal lattice and interact with it, producing a diffraction pattern that is then compared to reference standards. The SPIONs were freeze-dried for 24 hours using VaCO 2 ZIRBUS technology, and the analysis was performed with a Panalytical X'Pert PRO MDP X-ray diffractometer where the 2θ values were obtained using Cu-K radiation (k = 1.54060) generated in a range of 15° to 80° with a step size of 0.033.

TGA

TGA is a technique used to study the thermal stability and decomposition behavior of materials. Briefly, it consists of monitoring the mass of the sample as temperature changes occur in a specific atmosphere. For this work, the SPIONs were also freeze-dried for 24 hours using VaCO 2 ZIRBUS technology, and the TGA measurements were made using TGA-DSC – STA 449 F3 Jupiter at a heating rate of 10 °C. min^{-1} from room temperature (25 °C) to 900 °C in oxygen free atmosphere.

DLS

An optical measurement method used for the characterization of disperse systems is DLS. This method is most typically used to measure the Brownian motion of particles in liquids with the aim of particle size analysis. Briefly, a photon-counting detector is positioned at a specified angle and continually measures the amount of monochromatic laser beam scattering caused by the present particles. Due to Brownian motion, the quantity of photons hitting the detector varies with time, producing characteristic size-dependent fluctuation intervals in the field scattered intensity (Figure A.1). Typically, the intensity of the dispersed light oscillates more quickly, and the correlation declines more drastically with smaller particle sizes. Quantitative information concerning the time scale of these fluctuations can be obtained by a signal processing technique known as autocorrelation. Here, the autocorrelation decay of

the measured intensity can be correlated to the translational diffusion coefficient (D) by the expression in Equation A.3.

$$C\ (\tau) = 1 + \beta \exp(-2\Gamma\tau) \tag{A.3}$$

Where τ is the delay time (μsec), C is the autocorrelation function, β is a pre-exponential factor, and Γ is the decay constant. Whereas q is the scattering vector that can be determined by the Equation A.4.

$$q = \frac{4\pi n}{\lambda} \sin\left(\frac{\theta}{2}\right) \tag{A.4}$$

Here, n is the refractive index (n_{water} = 1.33), λ is the laser wavelength (λ = 532 nm) and θ is the scattering angle (θ = 90°). In turn, for spherical particles, D_h can be obtained from the translational diffusion coefficient (D) using the Stokes-Einstein relationship (Equation A.5).

$$D_h = \frac{k_B T}{3\pi\eta(T)D} \tag{A.5}$$

Where k_B and T denote Boltzmann's constant (k_B = 1.38x10^{-23} J/K) and temperature (T = 298.15 K) respectively, while η is the dynamic viscosity of the fluid (η_{water} = 0.00089 Pa.s at 25 °C) and D is the translational diffusion coefficient determined by Γ/q^2.

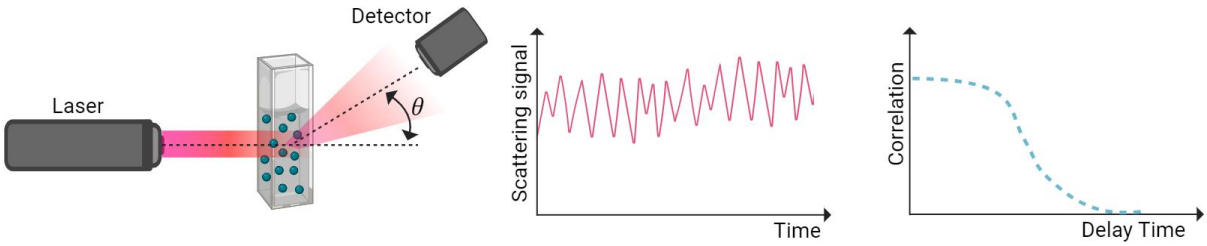

Figure A.1 | **DLS Principle**. A monochromatic laser beam illuminates the sample, and particle dimensions are obtained from variations in the scattered light. These variations, at a specific angle θ, are interpreted using an autocorrelation function, quantifying the resemblance between the intensity of scattered light at a given moment and a short time afterward, with this difference being defined as the delay time. Adapted from [143].

For this work, for a first characterization, the samples were prepared at 3 different concentrations (0.025, 0.05 and 0.1 mg/mL) of SPIONs with the three types of coatings using MiliQ water filtered with a 0.22 μm pore membrane syringe. The diluted suspensions were then measured in triplicate, with 3 individual passes, using a disposable cell with a dispersion angle of θ = 90°. All measurements were performed using a SZ-100 nanopartica series (Horiba, Lda) with a laser of 532 nm and controlling temperatures with a Peltier system (25 °C).

Table A.1 | **Hydrodynamic size and ζ - potential of different syntheses of the three types of SPIONs in water at 5 mg/mL.** Dh, hydrodynamic diameter; PDI, polydispersity index. Aggregate formation is also given in nanometers (nm). Data is expressed as mean ± standard deviation for at least three measurements.

Sample	Dh (nm)	Aggregates (nm)	PDI	ζ - Potential
SPIONs_OA	89.8 ± 5.2	--	0.22	-85.5 ± 2.8
	107.5 ± 4.8	--	0.17	-58.7 ± 2.6
	135.3 ± 9.2	--	0.23	-71.9 ± 4.6
	141.7 ± 4.9	--	0.23	-68.4 ± 3.9
SPIONs_DMSA	190.9 ± 13.8	--	0.21	-46.1 ± 1.5
	120.8 ± 7.8	275.6 ± 23.3	0.24	-39.3 ± 4.3
	111.4 ± 13.9	218.5 ± 21.6	0.19	- 47.8 ± 2.0
	96.9 ± 12.0	213.0 ± 31.2	0.26	-45.5 ± 4.5
SPIONs_APTES	85.8 ± 8.1	--	0.19	6.9 ± 1.5
	322.3 ± 12.4	16023.9 ± 40007.2	0.39	-9.9 ± 4.7
	212.4 ± 3.9	--	0.19	14.2 ± 1.0
	230.5 ± 13.1	--	0.25	16.0 ± 1.6

Magnetic Hyperthermia

When exposed to an AMF, the capacity of SPIONs to absorb energy is quantified using a parameter known as SAR. SAR is defined as the radiofrequency power absorbed per unit mass of an object over a specified time period (W/g), and this value is determined by the equation A.6.

$$SAR\ (W/g) = \frac{C_{NP} m_{Fe} + C_1 m_1}{m_{Fe}} \left(\frac{dT}{dt}\right)_{max} \quad (A.6)$$

Where C_{NP} is the specific heat of the SPIONs, C_1 is the specific heat of the liquid, m_1 is the mass of the fluid, m_{Fe} is the mass of iron in the colloid, and (dT/dt) max is the maximum gradient of the suspension temperature curve.

In this work, to evaluate the heating capacity of the produced NPs, the samples were exposed to a magnetic field strength of 300 Gauss and a frequency of 388.4 kHz using an Nb Nanoscale Biomagnetics D5 equipment. Four distinct concentrations (1, 2.5, 5, and 10 mg/mL) were tested in water and a temperature stabilization interval of approximately 30-40 seconds with no applied field was followed by a 10-minute application of the field.

A.3 Protein Corona

For the PC formation study the DLS method was also used under the same conditions as above to be able to observe the various hydrodynamic sizes. For this test SPIONs with the three types of coatings were prepared at a concentration of 0.05 mg/mL and different filtered (0.22 µm pore membrane syringe) dispersion media were tested. The formation of PC was tested using MiliQ water and using the

three types of cell culture media respective to the cell lines under study with and without FBS (in order to also test the influence of serum on the hydrodynamic size of the NPs). Four different time points were tested, for this, after dilutions, the samples were incubated for periods of 3 h, 6 h, 12 h and 24 h and were then measured in triplicates, with 3 individual runs, using a disposable cell with a scattering angle of $\theta = 90°$. The ζ-potential of the produced SPIONs was also evaluated to determine the surface charge of each coated SPIONs in the different dispersion media. The media had pH values of about 7, 6.9, 7.4, 7.8 and 7.4 for MiliQ water, PBS, RPMI, DMEM LG and DMEM HG respectively. A graphite electrode cell was utilized to conduct the analysis and all the measures were performed using a SZ-100 nanopartica series (Horiba, Lda) with a laser of 532 nm and controlling temperatures with a Peltier system (25 °C).

B. CELL VIABILITY AND SPIONS INTERNALIZATION

B.1 Cytotoxicity protocols

Resazurin Assay

Resazurin, with its IUPAC name being 7-hydroxy-10-oxidophenoxazin-10-ium-3-one, was first identified by Weselsky. It serves as an indicator for assessing cellular metabolic activity. This particular dye possesses the qualities of being membrane-permeable, water-soluble, stable in culture media, and non-toxic. Resazurin plays a pivotal role as an intermediary electron acceptor within the electron transport chain. It undergoes a transformation from its initial oxidized, non-fluorescent, blue state to its reduced state known as resorufin, which is fluorescent and exhibits a pink coloration as represented in Figure B.1. By monitoring a change in absorbance, it is possible to determine the amount of resorufin produced, which is proportional to the number of viable cells. The main advantages of the resazurin reduction assay over tetrazolium assays include its lower cost, higher sensitivity, and reduced interference from NPs.

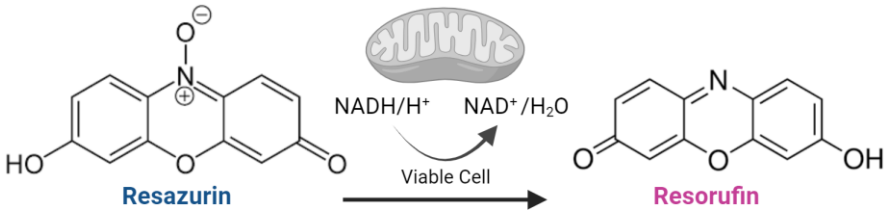

Figure B.1 | **Resazurin assay Principle.** Living cells maintain a reducing environment in their cytoplasm and mitochondria, where dehydrogenase enzymes transform resazurin, a blue, non-fluorescent compound, into a red fluorescent dye called resorufin. Adapted from [144].

For this assay, WM983b, THP-1 and HFFF2 cells were seeded in 96-well plates at a density of 100k cell/mL, 600k cell/mL, and 90k cell/mL respectively and left to adhere for 24 h. In order to assess possible cytotoxicity, the cells were exposed for 24 h and 48 h to 100 µL of concentrations of SPIONs between 1 mg/mL and 0.0625 mg/mL in culture medium. Positive control cells were treated with 10 % DMSO to ensure cell death. A negative control with viable cells treated with complete culture medium (control cells) was also established. After a 24 h and 48 h incubation period, each well was washed 2x with the respective cell culture medium. The resazurin solution was prepared from a more concentrated

solution in PBS at 0.04 mg/mL diluted 2x in cell culture medium. Subsequently, 150 µL of a previously prepared resazurin solution (50% resazurin plus 50% complete medium) was added to each well and the plates were left to incubate for a period of approximately 3 h in order to provide adequate fluorescence avoiding signal saturation. Following this interval, 100 µL of solutions from each well were transferred to a non-sterile 96-well cell culture plate prior to reading, ensuring minimal impact of the SPIONs' color on absorbance measurements. Subsequently, absorbance was recorded at 570 and 600 nm wavelengths utilizing a BioTek ELx800 UV absorbance microplate reader. Cell viability was then calculated as a percentage of the control using the formula [% cell viability = (NP treated cells/control cells) × 100].

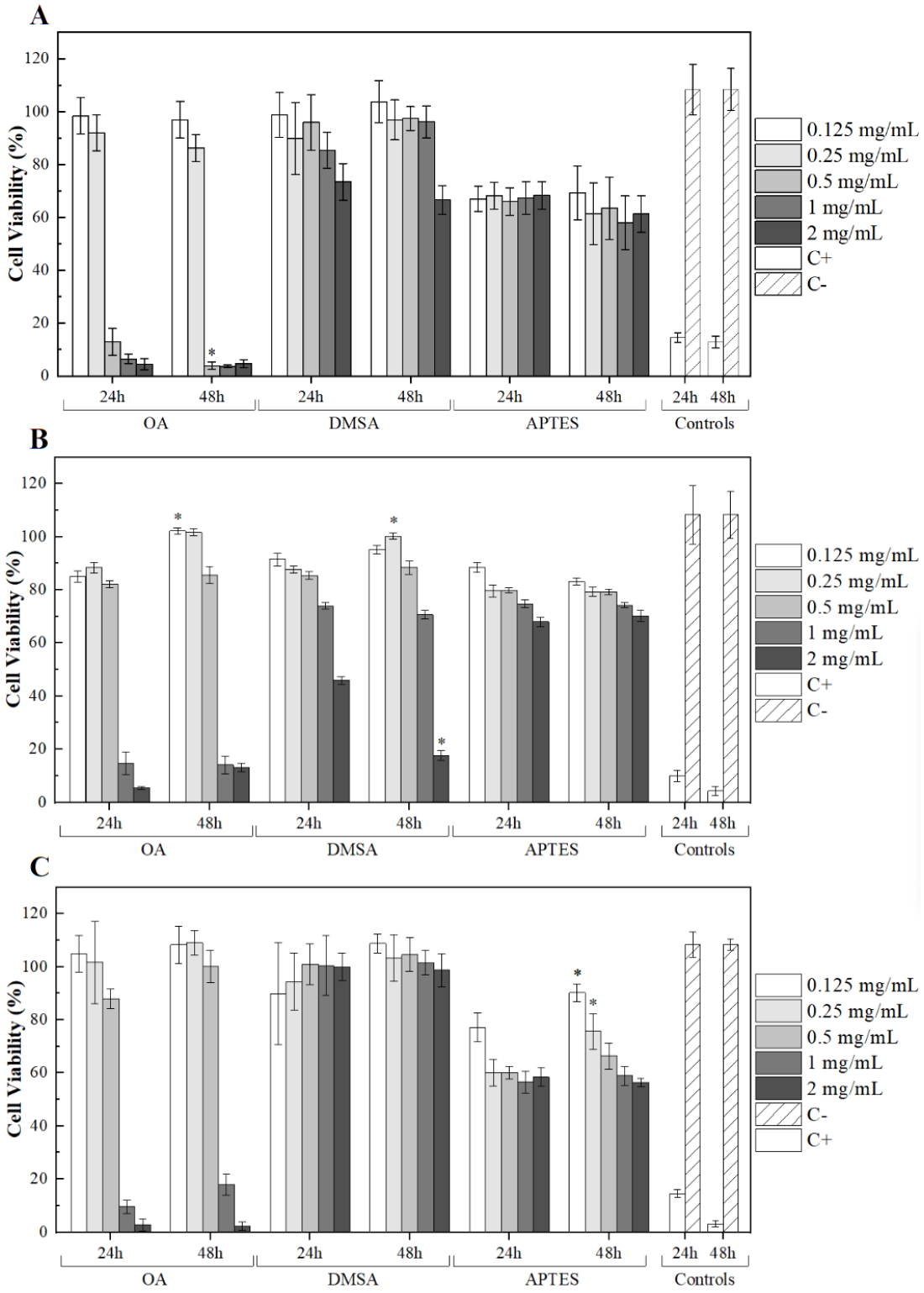

Figure B.2 | **Resazurin cell viability assay of the HFFF2 (A), WM983b (B) and THP-1 (C) cell lines after incubation periods of 24 h and 48 h with the three types of SPIONs.** The percentage of cell viability was calculated as a percentage of the cell control (without NPs) and the data are expressed as mean ± uncertainty for at least five replicates for each condition. *p value < 0.05 compared with the same condition at 24 h.

Live/Dead Assay

The live/dead cell assay is a viability test based on real-time quantitative imaging of cells labeled with two probes, calcein green-fluorescent^{AM} and ethidium red fluorescent. The distinction between live and dead cells is then made by simultaneous staining with these two fluorophores since calcein^{AM} stains live cells green indicating intracellular esterase activity and ethidium homodimer-1 indicates loss of plasma membrane integrity by staining dead cells red.

For this assay, the three cell lines were seeded in 24-well plates maintaining the cell densities used in the resazurin assay except for the fibroblasts, where it was used a concentration of 15k cell/mL (to facilitate counting) and were left to adhere for 24 h. Subsequently 500 µL of APTES-coated SPIONs at concentrations of 1 mg/mL, 0.5 mg/mL, 0.25 mg/mL, and 0.125 mg/mL diluted in the respective cell culture medium were added to each well and the plates were incubated for 24 h. Cells that were not exposed to SPIONs were used as a negative control. To avoid potential contamination due to the presence of SPIONs, gentamicin antibiotic (Gilbco) was also added to each well at a ratio of 1:1000 from a stock solution of 10 mg/mL. The cells were then washed twice with the appropriate cell culture medium, and 150 mL of DMEM without FBS supplemented with 25 mM of the acid 4-(2-hidroxietil)-1-piperazinaetanosulfonic (HEPES) (Sigma), 0.2 µg/mL of calcein (Biotium) and 0.8 µg/mL of ethidium homodimer-1 (Biotium) were added to each well. After being incubated for 30 minutes, the cells were then washed with the respective culture medium in order to stop the action of the fluorophores. Live and dead cell images were acquired using an epi-fluorescence microscope Nikon Eclipse Ti-S with 10x magnification, and the images were analyzed using Cell Profiler software. The percentage of live and dead cells were obtained using [% cells = treated cell count/total cells x 100] where outliers were removed considering a significance level of 0.05. For this assay, three replicates were made for each concentration and approximately 30 images were taken of each well.

B.2 Internalization Study

Prussian Blue Staining

The uptake of SPIONs by the three types of cell lines was determined based on Prussian blue staining. Prussian blue staining is a classic histochemical reaction in which hemosiderin in the cells is separated from Fe^{3+} by diluted hydrochloric acid. The Fe^{3+} then combines with potassium ferrocyanide to produce an insoluble ferrous cyanide known as Prussian blue. In this way it provides representative images of the iron content inside the cells by light microscopy, giving a qualitative notion of the amount of SPIONs in the different cell lines.

For this assay, WM983b, THP-1 and HFFF2 cells were seeded in 24-well plates with 12 mm coverslips, tripling the cell densities of the resazurin assay, to obtain a monolayer cell model, and allowed to adhere for 24 hours. After this time the cells were exposed to the three types of SPIONs for 1 h, 6 h and 24 h at a concentration of 100 µg/mL and a control without NPs was also made. Gentamicin antibiotic was added to each well at a ratio of 1:1000 from a stock solution of 10 mg/mL. After the

incubation periods, the cells were washed 4x with PBS and 400 µL/well of 4% PFA solution was added for fixation. After a time of about 15 minutes the cells were washed 3x with PBS and were then treated with 400 µL Perl reagent (4% potassium hexacyanoferrate (II) trihydrate), $K_4[Fe(CN)_6] - 3H_2O$ (w/v) (Merck) and 4% HCl (v/v)) for a period of 40 minutes at room temperature. The wells were then washed 4x with PBS and the coverslips were removed. Following a PBS and water wash, each coverslip was mounted on slides using 10 µL of Mowiol mounting media (Sigma-Aldrich). For this assay, three replicates were made for each condition and approximately 12 images were obtained of each well using a Nikon inverted microscope with transmitted light bright field and objectives with magnifications of 10x, 20x (not shown), and 40x.

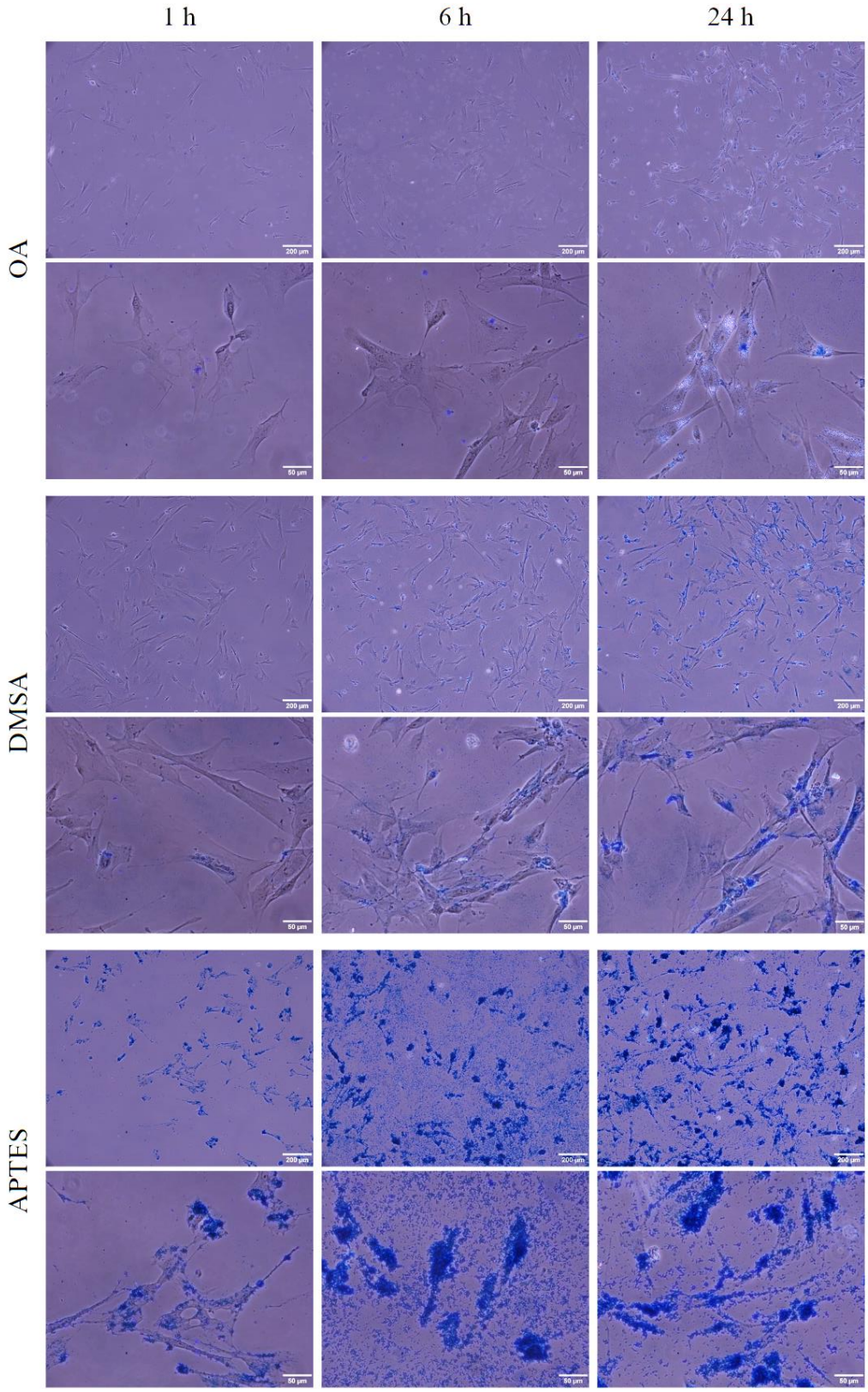

Figure B.3 | **SPIONs intracellular location in HFFF2 fibroblast cells after Prussian blue staining.** Cells incubated with 100 µg/mL of SPIONs coated with OA, DMSA and APTES for 1 h, 6 h and 24 h. Bright field images at 10x and 40x objective magnification with scale bar: 50 µm.

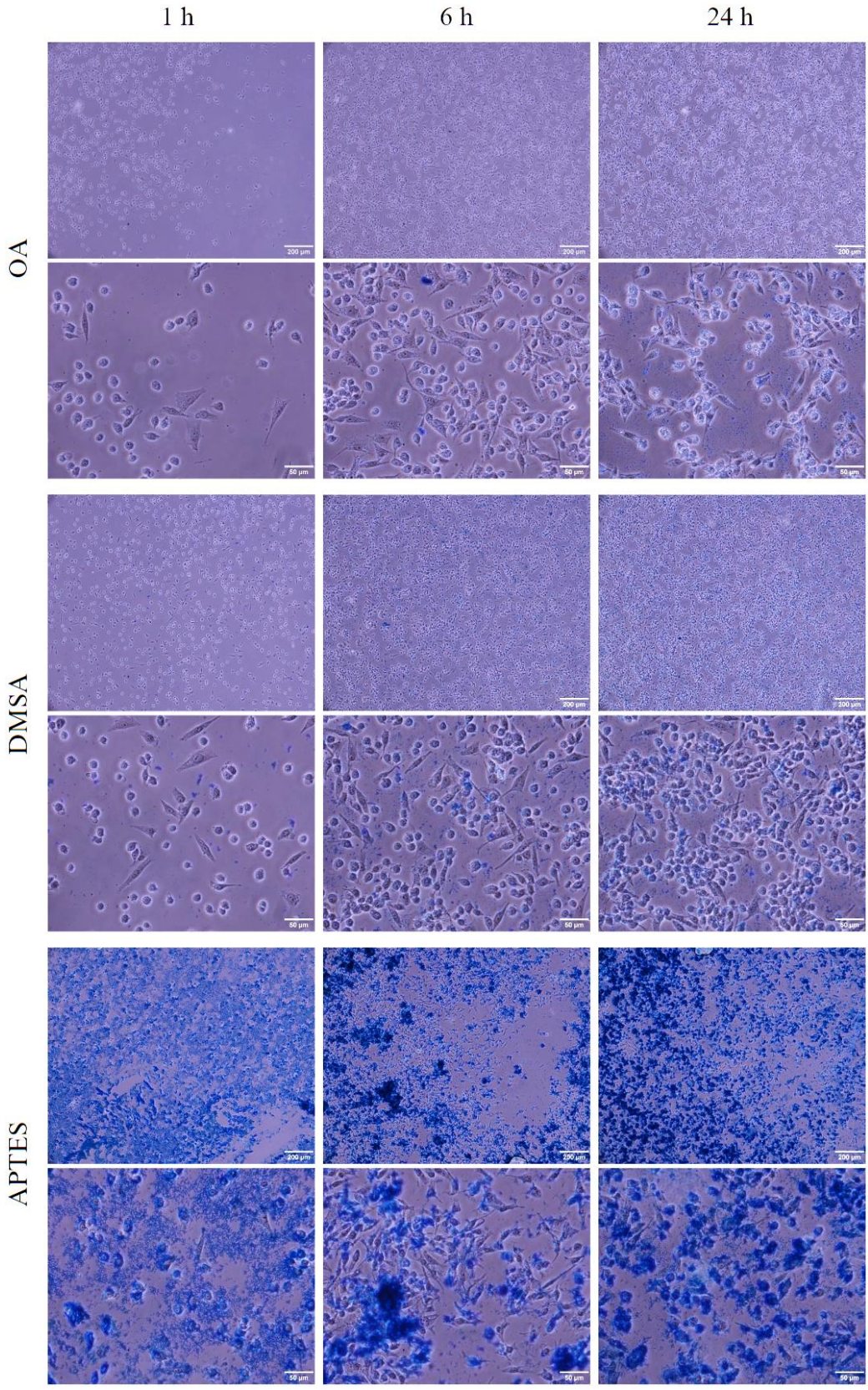

Figure B.4 | **SPIONs intracellular location in WM983b melanoma cells after Prussian blue staining.** Cells incubated with 100 µg/mL of SPIONs coated with OA, DMSA and APTES for 1 h, 6 h and 24 h. Bright field images at 10x and 40x objective magnification with scale bar: 50 µm.

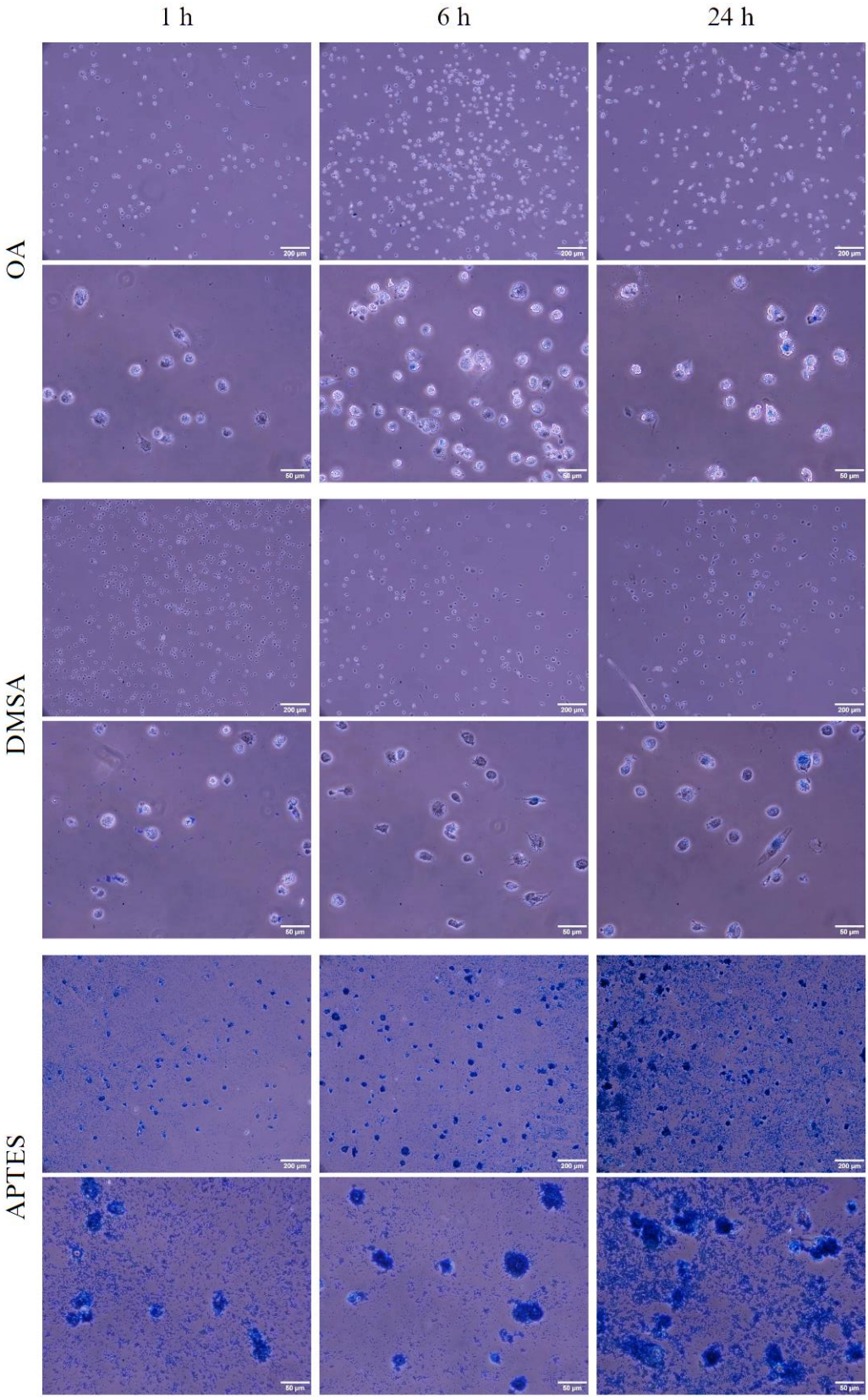

Figure B.5 | **SPIONs intracellular location in in THP-1 macrophage-like cells after Prussian blue staining.** Cells incubated with 100 µg/mL of SPIONs coated with OA, DMSA and APTES for 1 h, 6 h and 24 h. Bright field images at 10x and 40x objective magnification with scale bar: 50 µm.

B.3 *In vitro* Magnetic Hyperthermia

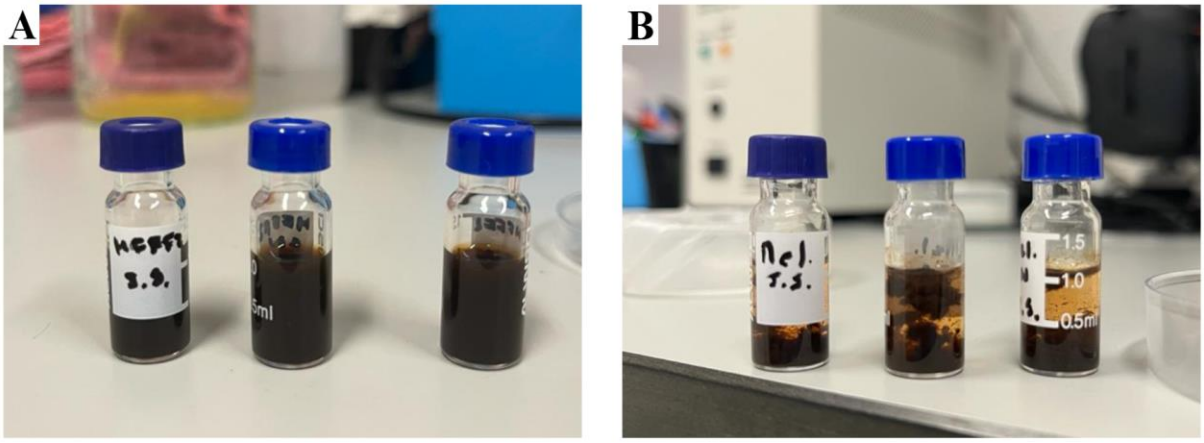

Figure B.6 | **Hyperthermia flasks before the *in vitro* MH assay**. Flasks containing the HFFF2 cell line (A) and the WM983b cell line (B) following a 24-hour incubation period with SPIONs.